Particle Correlations in Hadronic Decays of the Z Boson

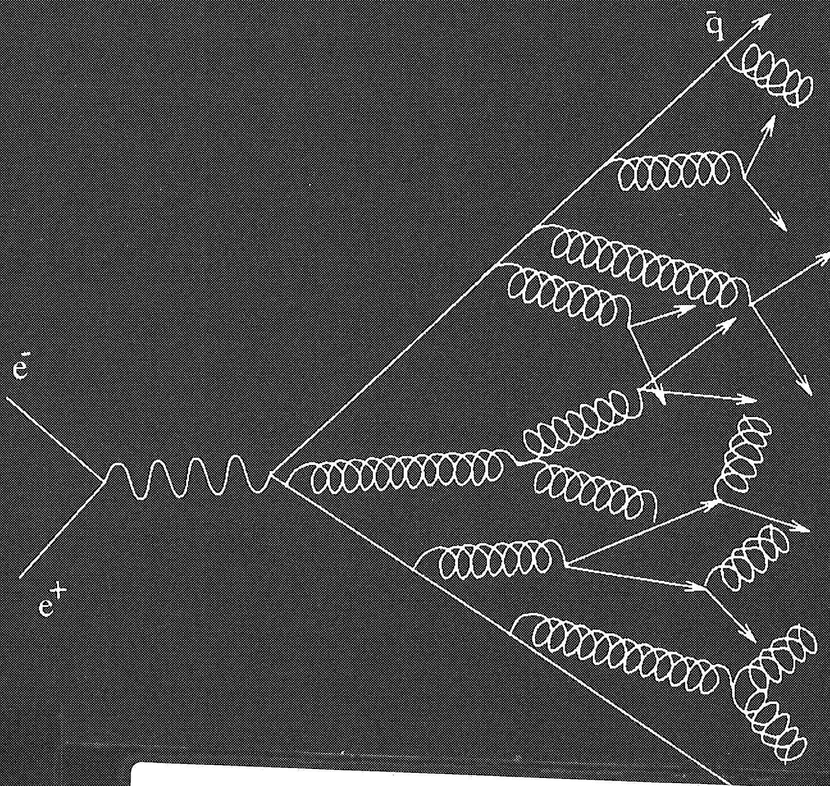

CERN LIBRARIES, GENEVA

Aly Aamer Syed

Particle Correlations in Hadronic Decays of the Z Boson

Een wetenschappelijke proeve op het gebied
van de Natuurwetenschappen.

Proefschrift

ter verkrijging van de graad van doctor
aan de Katholieke Universiteit Nijmegen,
volgens besluit van het College van Decanen
in het openbaar te verdedigen
op dinsdag 26 april 1994,
des namiddags te 3.30 uur precies, door

Aly Aamer Syed

geboren op 29 juni 1961 te Lahore, Pakistan.

Promotor: **Prof. Dr. E. W. Kittel**

Co-promotor: **Dr. W. J. Metzger**

CIP-DATA KONINKLIJKE BIBLIOTHEEK, DEN HAAG
Syed, Aly Aamer
Particle correlations in hadronic decays of the Z boson /
Aly Aamer Syed. - [S.1. : s.n.]. - I11.
Thesis Nijmegen. - With ref.
ISBN 90-9007038-9
Subject headings: high energy physics / elementary particles.

Maan Jee ki yaad main
aur
Baba Jee
Tofie
aur Bindya kay liaay

Acknowledgments

I have learnt a lot of things from many people during the time leading to this thesis. It would be a difficult task to thank them all individually for their help. However, I would like to thank at least some of them, realising that I would be forgetting some.

I would like to thank my promoter Prof. E. W. Kittel for introducing me to the challenging research topic of particle correlations and many discussions on the subject, my co-promoter Dr. W. J. Metzger for the help with my analysis and encouragement.

I would like to thank Prof. A. Zichichi for giving me the opportunity to work as an FBLJA fellow on the L3 experiment and Prof. M. Gourdin for introducing me to LEP physics. I would like to thank Dr. S. Banerjee for all the help and supervision that I got from him and Prof. T. Hebbeker for the discussions and help in QCD related matters. I benefitted from discussions with Dr. M. A. Chmeissani, Dr. M. Ilyas, Dr. J. Swain for which I thank them.

I would like to thank the Monte Carlo group for their cooperation, in particular Dr. N. Colino and Dr. T. Azemoon who helped me in writing the production control system.

While at CERN I enjoyed the company of my friends: Dr. P.V.K.S Baba, Dr. M. T. Dova, H. Hoorani, R. A. Khan, Dr. R. Malik, A. Niaz, Dr. K. N. Qureshi, H. A. Rizvi, C. Scheel, P. Vikas, and Dr. M. Wadhwa. I would like to thank them all for the nice time.

I thank all members of the high energy physics group in Nijmegen who provided me with a good atmosphere to work in, and the secretaries of the group E. Dikmans, A. Oosterhof and M. van Wees for their help in administrative matters. I thank my colleagues and friends Dr. D. Bourilkov, A. Buytenhuijs, M. Charlet, Dr. F. Filthaut, H. Kuijten, R. Rosmalen and P. Klok for the working environment in the Nijmegen apollo-room and help on numerous occasions and various matters.

My stay in Nijmegen would not have been as nice as it was if it were not for all the friends that I made here. I would like to thank all of them and hope they too enjoyed my company. In particular I would like to thank B. Bouwers, S. Bergh, J. Graat and R. van Dijk for their warm friendship.

A. S. Bhatti jo kay Villayat main hai uss kay saath foon aur email per rabita raha. Main uss ka shukar-guzar hoon kay uss nay mujhey sukhat waaqt main dillassa diya.

Aur aakhir main Mum jee aur Daddy jan, aap nay jis tarrah merry turbiat ki main uss ka jittna bhi sukkar-guzzar hoon kum hai. Main Yea kitab aap ki turbiat kay beghair nehin likh sukta tha. Main Tofie aur Bindya ka bayhud shukkar-guzar hoon kay inhoon nay merra bharpur saath diya.

Contents

Introduction

Our understanding of the basic structure of matter today is that all matter is made up of two types of particles, the quarks and the leptons, both of which are spin 1/2 fermions. Interactions between these particles are mediated by four types of forces: the gravitational force responsible e.g. for the weight of material things as we experience it in every day life, the weak force responsible e.g. for radioactive decay of certain nuclei, the electromagnetic force responsible for the interaction between charged particles, and the strong force which is responsible e.g. for holding the nuclei together. The quarks are acted upon by all four forces. The leptons, on the other hand, do not interact strongly.

In addition to these fundamental fermions, we know of the existence of the carriers of electromagnetic, weak, and strong forces as bosons. The carrier of the gravitational force has not yet been discovered. The photon is the carrier of the electromagnetic force, the $W^{\pm}$ and the Z bosons are the carriers of the weak force and the gluons are considered to be the carriers of the strong force.

One can ask oneself 'where does matter come from and why do we see so many types of quarks and leptons, when the world and the matter as we know it can be explained with a smaller number?'. One possible answer to these exemplary questions is provided by the *Big Bang* theory, according to which at the time of the Big Bang, all matter and energy of the universe was condensed to a point. The laws of physics for that epoch are not known. In any case, there was no distinction between the different forces and that is why this period is called the *Grand Unification*. It was only after 10^{-34} seconds that the weak and electromagnetic forces had become distinguishable due to decreased energy density as the universe expanded. The quarks and gluons came into being in a plasma state. At 10^{-10} seconds, the energy density was lower still and quarks and gluons could start to condense to form nucleons. However, still the nucleons could not stay together to form nuclei, so that there was a sort of hadron gas. Only after 300,000 years did matter and radiation become decoupled and the first atomic nuclei were formed. The stars and galaxies were formed 1000 million years after the big bang and life forms emerged which led to us and what we see around us. As time progressed from the instant of the big bang, the universe expanded and the energy density kept decreasing. More and more of the particles that existed at an earlier time in a higher energy density could no longer be created, and thus today we see fewer types of particles than there were at high energy densities.

In today's particle accelerators we can recreate, for a very short interval of time in a very small space, the high energy densities needed to create the primordial particles by colliding particles at very high energies. Having produced such particles in reproducible experimental conditions, we can study their dynamics by building and testing theories. At LEP, electrons and positrons are collided head-on at velocities close to that of light. The result is the production of Z bosons which must have abundantly existed in the time period between 10^{-34} and 10^{-10} seconds after the big bang and later decayed into quarks and leptons. The quarks later condensed due to a mechanism called hadronization to become hadrons.

The object of this thesis is to try to understand some of the processes that took place between the time when the quarks were "free" particles and when they became bound states (hadrons). According to the present understanding this transition occurred because partons (quarks and gluons) branched repeatedly leading to showers of these partons which lead to hadronisation. The study is performed on correlations between the hadrons produced in the decays of Z bosons. In particular we study the phenomena of self-similarity (intermittency) and angular ordering in parton showers.

In chapter 1, we give a theoretical introduction to the phenomenon of hadron production in e^+e^- interactions. Chapter 2 describes the apparatus used in the study, i.e. the LEP collider and the L3 detector. Chapter 3 describes a system developed for automatic book keeping for the preprocessing of the large amount of data and Monte Carlo events in the L3 experiment. Chapter 4 gives a description of the event selection procedure and of the resolution obtained in the L3 detector. In chapter 5, the analysis performed on the data to study self-similarity in parton showers is presented and chapter 6 gives the analysis performed to study the coherence effects in parton showers. The last section of this thesis, the summary, is followed by the bibliography.

Chapter 1

Theoretical Introduction

1.1 Introduction

Deep inelastic lepton nucleon scattering provided the evidence for the composite nature of nucleons. The constituents of nucleons behave as point-like particles when probed with leptons and are spin $\frac{1}{2}$ particles. A study of electromagnetic and weak cross sections revealed that these constituents must have fractional charges. So, the constituents were identified as the quarks introduced earlier to explain the large number of hadrons.

Only half of the total nucleon momentum could be seen by deep inelastic lepton-nucleon scattering experiments. This led to the introduction of gluons, responsible for interactions between quarks but not interacting with the leptons. The existence of the Δ^{++}, a baryon with three quarks of the same flavour, all in the same angular momentum and isospin state, called for the introduction of the concept of colour to avoid violation of the Pauli exclusion principle, by allowing the quarks to have three degrees of "colour" freedom. Later measurements of the ratio

$$\mathrm{R} = \frac{\sigma(\mathrm{e^+e^-} \to \mathrm{Hadrons})}{\sigma(\mathrm{e^+e^-} \to \mu^+\mu^-)},$$

which in the lowest order is equal to the sum of the squared charges of the contributing quarks flavours times 3 the colour degrees of freedom, confirmed that the number of colours is indeed three.

Today, Quantum Chromo Dynamics (QCD) is considered to be the theory of strong interactions. The gauge group of the theory is SU(3), the gauge bosons are eight gluons, and the quarks are the fermions of the theory.

Up to now, 5 different "flavours" of quarks and anti-quarks (each in 3 colours) have been identified in experiments. A 6th flavour (truth or top) is predicted but still to be discovered. Table 1.1 lists the additive quantum numbers (other than baryon number) for the 6 quark flavours. The corresponding numbers for the anti-quarks are the same in magnitude but opposite in sign.

Property/Quark	d	u	s	c	b	t
Q - electric charge	$-1/3$	$+2/3$	$-1/3$	$+2/3$	$-1/3$	$+2/3$
I_z - isospin z-component	$-1/2$	$+1/2$	0	0	0	0
S - strangeness	0	0	-1	0	0	0
C - charm	0	0	0	$+1$	0	0
B - bottomness (beauty)	0	0	0	0	-1	0
T - topness (truth)	0	0	0	0	0	$+1$

Table 1.1: *Quark quantum numbers*

1.2 Running coupling constant α_s

Contrary to Quantum Electro Dynamics (QED), the QCD is non-abelian and allows for couplings between its gauge bosons, which carry colour charge.

As in the case of QED, the effective coupling at some value of a reference scale Q^2 is different from the true coupling, due to screening effects originating from vacuum polarization. This leads to the running of the coupling constant with varying momentum transfer $|Q^2| = \mu^2$. In leading order, the running coupling constant of QCD is given by the relation

$$\alpha_s(\mu) = \frac{1}{b_o \ln(\mu^2/\Lambda^2)}$$

where

$$b_o = \frac{33 - 2n_f}{12\pi},$$

and n_f is the number of flavours active at a given energy and Λ is a QCD parameter which indicates the boundary between perturbative and non-perturbative regions of QCD and is given by

$$\Lambda = \mu_o \exp \frac{1}{-2b_o\alpha_s(\mu_o)}$$

where μ_o is the reference scale taken to be the Z mass at LEP energies.

The self coupling of the gluons leads to interesting properties of QCD such as colour confinement and asymptotic freedom.

1.3 Hadron production in e^+e^- annihilation

Figure 1.1 shows a schematic illustration of the process of $e^+e^- \to q\bar{q}$, where the production mechanism of hadrons is believed to follow 4 distinct phases [1]:

Phase (i): Production of a $q\bar{q}$ pair. This phase is described by the electroweak theory. Electroweak corrections, the most important of which is initial state bremsstrahlung, are not included in the figure.

Phase (ii): The initial quarks may radiate gluons, which in turn may radiate quark-antiquark pairs or gluons thus leading to a parton shower. This phase is described by perturbative QCD.

Phase (iii): The coloured partons produced in phase (ii) fragment into colourless hadrons. This phase is explained by some phenomenological model, since, due to the large value of α_s, perturbative QCD can no longer be used here.

Phase (iv): The unstable hadrons produced in phase (iii) decay into the experimentally observed hadrons. Again, QCD cannot be used here and the experimentally determined branching ratios are used to predict the outcome. For weak decays, one could attempt to use electroweak theory, but in practice one resorts to a phenomenological description here, as well.

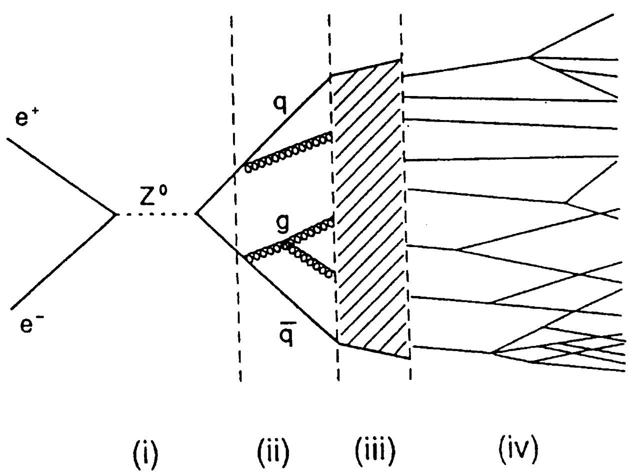

Figure 1.1: *The phases in the process of hadron production in* e^+e^- *annihilation*

1.3.1 Fermion pair production $e^+e^- \rightarrow f\bar{f}$

The lowest order total cross section for fermion pair production in e^+e^- annihilation (phase (i)) is given by [2]

$$\sigma(e^+e^- \rightarrow f\bar{f}) = 4\pi/3 \cdot N_c \cdot \alpha^2/s \cdot [Q_e^2 Q_f^2 + (V_e^2 + A_e^2)(V_f^2 + A_f^2) \cdot |\chi^2| + 2Q_e Q_f V_e V_f \cdot \mathrm{Re}(\chi)],$$

where s is the centre of mass energy squared and masses of the particles involved are much smaller than $\sqrt{s}$. The function χ describes the Breit-Wigner form of the Z resonance:

$$\chi = \frac{1}{4sin^2\theta_w cos^2\theta_w} \cdot \frac{s}{s - m_z^2 + im_z\Gamma_z},$$

with m_z being the mass of the Z boson, Γ_z the total decay width of the Z boson and θ_w is the weak mixing angle. Further, α is the electromagnetic fine structure constant, Q_f is the electric charge of the fermion f, and V_f and A_f are the vector and axial vector couplings to fermions and N_c is the number of colours of the fermion (1 for leptons , 3 for quarks). The first term in the cross section formula describes the photon s-channel, the second term the Z exchange contribution and the third term the γ-Z interference contribution to the total cross section.

It should be noted that the above formula for the total fermion cross section is the lowest order approximation. To get a result which can describe the experimentally observed cross section, further corrections must be applied for initial state radiation of photons and final state radiation of gluons and photons [3, 4].

1.3.2 Gluon radiation

The primary quarks produced in phase (i) of the diagram in figure 1.1 can radiate gluons. Subsequently, a shower or cascade is developed by further branching of these gluons into quarks or gluons in phase (ii) of figure 1.1. QCD predictions can be made about this phase using two different approaches.

In one approach, called the matrix element (ME) approach, the Feynman diagrams are exactly calculated within QCD order by order. The calculations of the Feynman diagrams for higher orders become increasingly difficult and to date only calculations up to second order exist. Thus, the final state in this approach consists of at most 4 partons which are allowed to hadronize according to one of the fragmentation models described below.

The second approach is known as the parton shower (PS) approach. This approach is constructed within the framework of the leading logarithm approximation (LLA), where only the leading terms are kept in the perturbative QCD expansion. Several extensions of these approximations exist, such as MLLA (M for modified), DLLA (D for double), or NLLA (N for next-to-), all of which try to take into account some subleading corrections.

The production of showers can be viewed as a sequence of $1 \to 2$ branchings $a \to bc$. Here, a is the mother parton and b and c are the daughters. Each daughter is allowed to branch further, so that a tree-like structure is formed. The branchings considered are: q $\to$ qg, g $\to$ gg, g $\to$ q$\bar{\text{q}}$. They are achieved in a probabilistic manner and the probability of a branching is given by the Altarelli-Parisi evolution equations [5]. The differential probability $\mathrm{d}\mathcal{P}$ for a parton to branch is given by

$$\mathrm{d}\mathcal{P}_a = \sum_{b,c} \frac{\alpha_s}{2\pi} P_{a\to bc}(z)\mathrm{d}t\mathrm{d}z$$

where

$$t = \ln(Q^2/\Lambda^2) \Rightarrow dt = d\ln(Q^2) = dQ^2/Q^2,$$

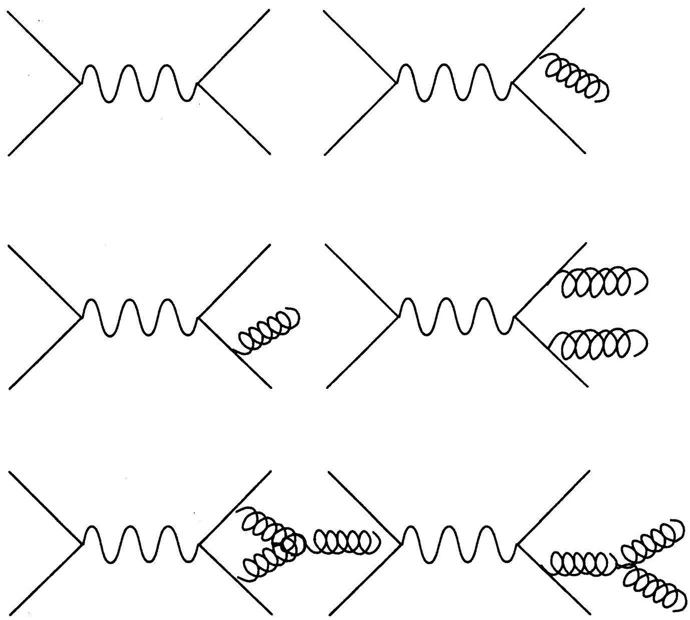

Figure 1.2: *Feynman diagrams for matrix element calculation for* $O(\alpha_s^2)$.

where z gives the sharing of energy of the parton a between the daughter partons b and c, with b taking a fraction z and c taking a fraction $1-z$. In the above expression, $P_{a\to bc}$ are splitting kernels given by

$$P_{\mathrm{q}\to\mathrm{qg}}(z) = \frac{4}{3}\frac{1+z^2}{1-z},$$

$$P_{\mathrm{g}\to\mathrm{gg}}(z) = 6\frac{(1-z(1-z))^2}{z(1-z)},$$

$$P_{\mathrm{g}\to\mathrm{q\bar{q}}}(z) = \frac{n_f}{2}(z^2+(1-z)^2).$$

Using the above expressions, one must make sure to conserve flavour and momentum at each branching.

1.3.3 Hadronization

Phase (iii) of figure 1.1 is called the hadronization or fragmentation phase. In this phase, the partons produced in phase (ii) form colourless hadrons. This transition must take place, since QCD leads to colour confinement and the coloured partons cannot be observed as free particles. At the end of phase (ii) the processes have become soft and the running

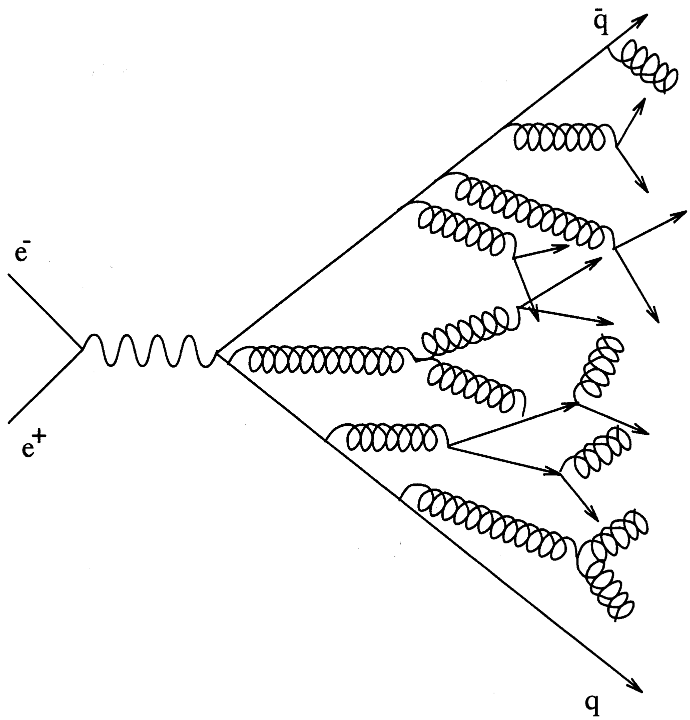

Figure 1.3: *Diagram showing a possible configuration in a parton shower evolution*

of the coupling constant makes α_s too large for perturbative QCD to be applied. At this point, one is compelled to use phenomenological models bridging the gap between the coloured partons and the colourless hadrons. Three main types of fragmentation models are used today [1]. They are the independent fragmentation (IF), the string fragmentation (SF), and the cluster fragmentation (CF), as briefly described below.

Independent fragmentation

Independent fragmentation (IF) was proposed in the seventies [6] and has gradually been replaced by string and cluster fragmentation models which fit the data better. Independent jet fragmentation considers each jet as an independent $q \to q' +$Meson cascade, repeating itself until there is insufficient energy to continue. The longitudinal fragmentation function does not depend on the energy of the primary parton but on the fractional momentum taken by the daughter meson. The same distribution is recursively used to generate each daughter momentum in a cascade. The relative abundance of quark flavours, the spin of the produced mesons, a parameterization of the transverse momentum distribution and the fragmentation function are the parameters of this model.

String fragmentation

The string fragmentation model [7] is based on a QCD inspired idea of a colour flux tube (also called a string) extending from a quark to an antiquark. Gluons are treated as kinks on the string. The partons produced move apart, thus increasing the energy stored in the string. If this energy reaches a critical value of 1 GeV/fm, then the string breaks into two and a new $q\bar{q}$ pair is created. The resulting string segments can further break up, thus producing more pairs of $q\bar{q}$. When no more break-ups can take place, the $q\bar{q}$ from adjacent string break-ups are combined to produce mesons. There are parameters in this model which control the transverse and longitudinal momenta of the produced hadrons, as well as the relative abundance of quark flavours and meson spins.

Cluster fragmentation

In the cluster fragmentation model [8], a cluster is considered to be the basic unit from which the hadrons are produced. A cluster is characterized by its total mass and its flavour content. Cluster fragmentation takes the parton configuration at the end of a parton shower or a parton configuration as generated by the matrix element approach. In the former approach, the gluons are split into $q\bar{q}$ and colourless clusters are formed which decay into smaller clusters or hadrons. In the latter approach, strings are stretched between the partons, which decay into clusters which in turn decay into hadrons. In this model there is only one basic parameter which is the maximum cluster mass.

1.3.4 Decays

In the last phase of the process of hadron production in e^+e^- collisions, the unstable particles decay into stable particles. Theoretical predictions for this phase are not possible, except for weak decays of heavy quark mesons, for which the known matrix elements can be used. Usually, however, one resorts to phenomenological models based on experimental information on particle life times and branching ratios.

1.4 Coherence effects in QCD parton showers

Two distinct consequences of gluon coherence effects have been identified in perturbative QCD [9]. They are the so-called intra-jet coherence effects which manifest themselves as angular ordering in parton showers as explained below and the inter-jet coherence effects which have come to be known as the 'String effect'.

Coherence effects in perturbative QCD gluon emission have been reported in [10, 11, 12]. It has been found in [10] that when calculating the cross section in doubly logarithmic perturbative QCD, contributions to the cross section come only from the region of phase space in which the soft gluon energies are ordered. In terms of angles this condition reads as

$$\theta_{ji} > \theta_{i,i1} > \theta_{i,i2} \ldots > \theta_{i,ir}$$

where the jth gluon emits the ith gluon, which in turn emits gluons $i_1, i_2, \ldots, i_r$ and $\theta_{i,ir}$ is the angle between these gluons.

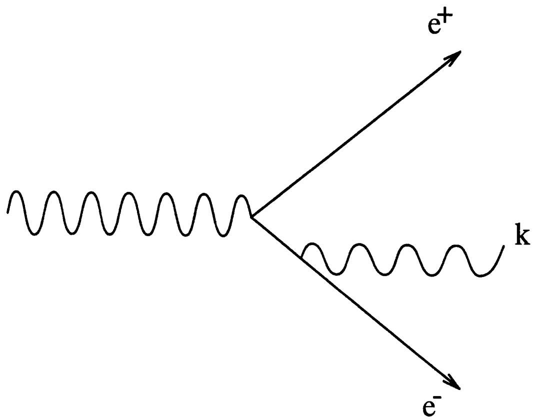

Figure 1.4: *Emission of a soft photon k after* e^+e^- *pair production*

An explanation of this phenomenon has been given in [9]. The authors take as a simple model of jet cascade, the radiation of a photon by a relativistic e^+e^- pair in a QED shower as shown in figure 1.4. The transverse separation $\rho_\perp^{e^+e^-}$ between the e^+e^- pair at the time of a photon emission by the $e^-(e^+)$ is given by

$$\rho_\perp^{e^+e^-} \approx \lambda_\perp \frac{\theta_{e^+e^-}}{\theta_{\gamma e^-}},$$

where $\theta_{e^+e^-}$ is the angle between the e^+ and the e^-, $\theta_{\gamma e^-}$ is the angle between the emitted photon and the $e^-(e^+)$ and $\lambda_\perp$ is the transverse wave length of the emitted photon.

It can be seen from the above expression that for $\theta_{\gamma e^-} > \theta_{e^+e^-}$, $\rho_\perp^{e^+e^-} < \lambda_\perp$, so that the emitted photon cannot resolve the internal structure of the e^+e^- pair and probes only the total electric charge of the e^+e^- system, which is zero. Thus, for $\theta_{\gamma e^-} > \theta_{e^+e^-}$, the emission of a photon is strongly suppressed.

The authors extend the above picture to QCD parton cascades in which soft gluons are emitted. The difference here is that gluons (and, therefore, the $q\bar{q}$ system) carry colour charge. As a consequence, the emission of a soft gluon by an unresolved $q\bar{q}$ pair is not zero, but the radiation acts as if it came from the parent parton. This situation is shown in figure 1.5, where the gluon emitted by the q or $\bar{q}$ at an angle larger than $\theta_{q\bar{q}}$ acts as if it was emitted from the parent gluon g. In fact, it turns out, that one gets all leading double and single logarithmic effects correctly by allowing the gluon emission independently, off the quark q when $\theta_{\mathrm{qk}} < \theta_{\mathrm{q\bar{q}}}$, off the anti-quark $\bar{\mathrm{q}}$ when $\theta_{\mathrm{\bar{q}k}} < \theta_{\mathrm{q\bar{q}}}$, and off the parent gluon when $\theta_{\mathrm{qg}} > \theta_{\mathrm{q\bar{q}}}$.

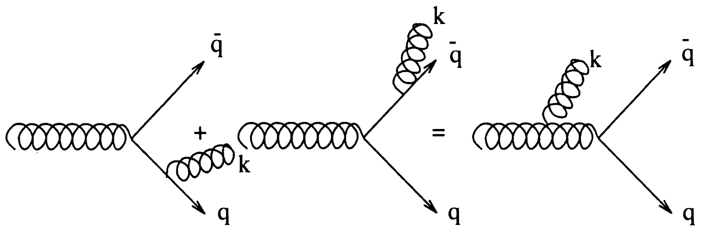

Figure 1.5: *Coherence in gluon emission where a wide angle emission acts as if it came from the parent gluon*

1.5 Intermittency

A further important property of branching in a QCD shower is its nearly self-similar character. As already pointed out as early as 1979 [13, 14, 15], this behaviour is expected to lead to a fractal structure of the QCD shower. In [16, 17, 18], it is shown that the (multi) fractal dimensions of a QCD shower are directly given by the anomalous dimensions $\gamma_{\circ} = 2\sqrt{3\alpha_s/2\pi}$ of QCD and, therefore, by the running coupling constant α_s. As discussed in short below the properties can be determined from the nature of particle density fluctuations, in particular their dependence on the resolution by which they are investigated.

In 1983, the JACEE collaboration published events with very high multiplicity (about 1000 particles) in a cosmic ray exposure of emulsion chambers [19]. These events show large fluctuations on an otherwise smoothly varying rapidity distribution. This observation has led the authors of [20, 21] to try to understand the fluctuations by the use of normalised factorial moments suppressing the statistical noise:

$$F_q(\delta) = \frac{\langle n(n-1)\ldots(n-q+1)\rangle}{\langle n\rangle^q},$$

where n is the (charged) particle multiplicity in a phase space cell of size δ.

The factorial moment analysis is designed to study the density fluctuations from event to event as a function of decreasing bin size of a phase space variable such as rapidity. If a scale invariant power-law like behaviour

$$F_q(\delta) \propto \delta^{-f_q}$$

is exhibited by the factorial moments, then the system is defined as an intermittent system [1]. The powers f_q , usually called intermittency indices, play the role of anomalous dimensions (or codimensions) of the fluctuation pattern and can be related to the Rényi dimensions D_q characterising a set of fluctuations [22],

$$D_q = D - \frac{f_q}{q-1},$$

where D is the usual topological dimension of the underlying phase space cells.

One possible explanation already given in [20] was that of a critical system with a quark-gluon plasma. However, later experimental observations have ruled out the quark-gluon plasma as responsible for the observed power-law behaviour of the factorial moments [23]. A number of attempts have been made to describe this power-law like behaviour, also reviewed in [23]. The most promising candidates are said to be random self-similar multiplicative branching type models. Such types of models can be applied not only in the perturbative phase of QCD as discussed above, but also in the non-perturbative hadronization phase and have in fact been used extensively in the Monte Carlo event simulation programs for e^+e^- collisions.

Recently, perturbative QCD calculations have indeed shown that perturbative QCD is *inherently intermittent* [18, 17]. Analytical calculations have been performed in DLLA in terms of angular phase space variables [18], and fixed coupling QCD factorial moments turn out to reveal the intermittency phenomenon with intermittency indices [17]:

$$\frac{f_q}{q-1} = D - \frac{q+1}{q}\gamma_\circ$$

with $\gamma_\circ = 2\sqrt{3\alpha_s/2\pi}$. The Rényi dimensions are then related to α_s simply as:

$$D_q = \frac{q+1}{q}\gamma_\circ$$

The authors of [18] further show that the factorial moments saturate at very small energy scale and that such a behaviour is a consequence of the large value of the running coupling constant in that region, which leads to the filling of space with soft gluons thus masking any density fluctuations originating from higher virtualities.

[1]The word *Intermittency* has been borrowed from fluid dynamics. The transition of a liquid from laminar flow to turbulent flow goes through a phase where there are sites in space and time at which there are small areas of wild fluctuations called 'turbulence slugs'. Such areas appear intermittently in space and time and thus the word *Intermittency*

Chapter 2

The Apparatus

2.1 LEP

LEP "The Large Electron Positron Collider" is a collider designed to store and accelerate beams of electrons and positrons to a high energy of about 55 GeV per beam in its first phase of operation (LEP100) and be able to take the energy to 110 GeV per beam in its second phase of operation (LEP200). It is situated at CERN in Geneva, Switzerland and the adjoining area of France. The accelerator is installed in an underground tunnel forming a closed circuit for the beams of electrons and positrons. The LEP tunnel is divided into 8 circular and 8 straight sections and its shape resembles a circle. The plane of the LEP tunnel is inclined by 1.4% and is at a depth of 50-150 meters below the ground level. The tilt in the LEP plane was necessary to avoid civil engineering problems in excavating the tunnel in the rocky terrain of the Jura mountains. There are four points on the tunnel where the particle detectors L3, Aleph, Opal and Delphi are situated. All four points have access shafts from the surface. In addition to the 4 access points for the detectors, there are 18 others points or "pits" from where the LEP machine is accessible for service.

Low energy accelerator systems previously built at CERN, two linear accelerators, a storage ring for electrons and positrons (EPA), the proton synchrotron (PS) and the super proton synchrotron (SPS) form the injection system for LEP. The beams of the electrons and positrons generated by an electron gun and a positron converter are first accelerated by two linear accelerators to 600 MeV. They are then stored in the electron positron storage ring (EPA). From the EPA, the beams are fed into the PS which increases their energies to 3.5 GeV and injects them into the SPS. The SPS does the final bit before injection into LEP, taking the energies of the beams up to 20 GeV.

The main components of LEP are a vacuum chamber or beam pipe running along the tunnel, bending magnets to bend the beams in the circular sections of the accelerator, the focusing magnets or magnetic lenses to focus and collimate the beams, the radio frequency cavities to accelerate the particles and to compensate for the energy lost by the particles due to synchrotron radiation.

After injection into LEP, the beams are further accelerated to the required energy

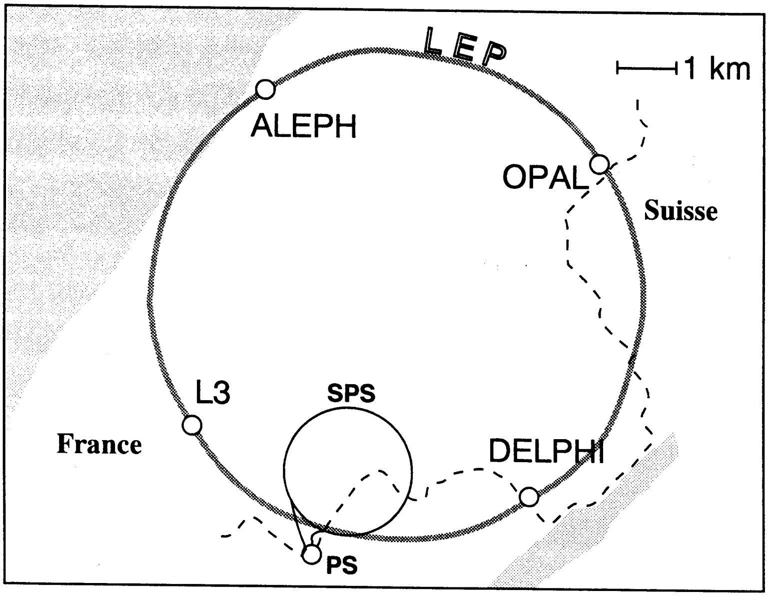

Figure 2.1: *The LEP layout*

and collimated. Once stable beams have been achieved, they are brought into collision in the four detectors. A detailed description of LEP can be found in [24]. Some of the important parameters of the LEP machine are given below in table 2.1 and figure 2.1 shows the layout of LEP. It should be noted that some of these parameters depend on the number of bunches in the machine which is taken to be 4 for the parameters quoted in this table.

2.2 The L3 detector

2.2.1 General overview

The L3 detector is situated in one of the four experimental areas of the LEP tunnel. It has been designed with an emphasis on high resolution energy measurement of electrons, photons and muons [25]. L3 is a hybrid detector consisting of five different types of detectors. All the active detecting elements in L3 are installed in a solenoidal magnet weighing 7800 tons which provides a magnetic field of 0.5 Tesla. From the beam interaction point towards the magnet, the active detecting elements are arranged as follows:

LEP Parameters	
Date of Commission	14 July 1989
Circumference	26.26 km
Number of Interaction points	8
Number of Experimental areas	4
Injection Energy	20 GeV
Energy per Beam	$\approx$ 45 GeV
Luminosity	$10^{31}cm^{-2}s^{-1}$
Beam Power	1.2 MW
Number of RF Cavities	128
RF Frequency	352.21 MHz
Number of Bunches	4/8
Revolution Time for a Bunch	88.92 μsec
Current per Bunch	0.78 mA
Total Current per Beam	2.98 mA
Total Current in both Beams	4.7 mA
Total RF Power	16 MW
Horizontal Beam Radius	300 μm
Vertical Beam Radius	12 μm
Pressure in Beam Pipe (No beam)	8×10^{-12} Torr
Pressure in Beam Pipe (with beam)	$\approx 10^{-9}$ Torr

Table 2.1: *LEP Parameters*

- A central tracking chamber called TEC to detect charged particles, measure their momenta and determine their charge.
- An electromagnetic calorimeter called BGO to measure the energy and production angles of electrons and photons with a high accuracy.
- A scintillation counter to measure the crossing time of muons in order to veto the cosmic ray muons.
- A hadron calorimeter to measure the energy and production angles of jets of hadrons. It also acts as a hadron absorber so that only a clean sample of muons reaches the next detector element.
- A precision muon chamber system to measure the momentum and spatial direction of muons.

In addition to these subdetectors, there is a luminosity monitor installed in the forward and backward direction, which measures the luminosity of the LEP beams by measuring the cross section of small-angle Bhabha scattering of electrons and positrons.

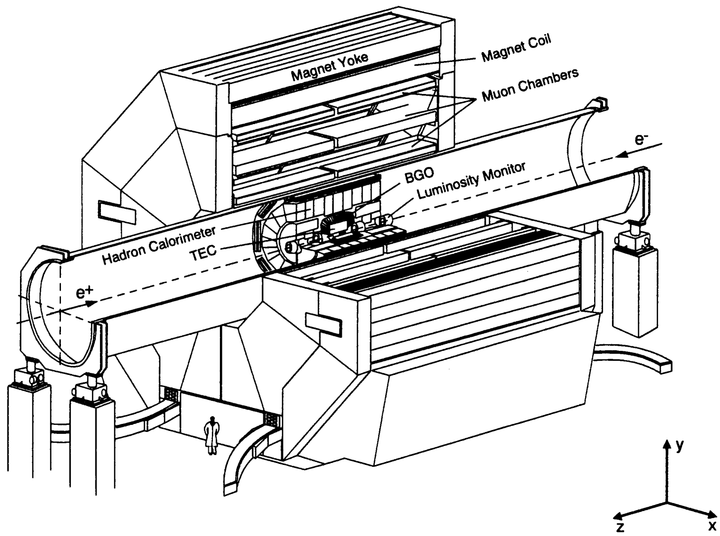

Figure 2.2: *The L3 Detector*

Except for the muon chambers, all the subdetectors are installed inside a support tube, which passes through the magnet and is concentric with the beam pipe. The length of the support tube is 32 m, it has a diameter of 4.45 m and it is made of stainless steel. The muon chambers are mounted outside the support tube but inside the magnet.

The data taking is initiated by a trigger system. Upon receiving the trigger, the data acquisition system collects the event information from different subdetectors, combines it into a single event and writes it out onto a magnetic tape. The events are later reconstructed on the off-line computers using the L3 reconstruction programs.

Figure 2.2 shows a pictorial view of the L3 detector. The geometrical coordinate system chosen for L3 is such that the Z-axis lies along the e^- beam direction, the X-axis lies in the horizontal plane perpendicular to the Z-axis and the Y-axis is in the transverse plane relative to the beam direction and X-axis to form a right handed coordinate system.

Each of the above mentioned components of the detector system will now be described in some detail.

2.2.2 Central tracking chamber

The design goals of TEC are as follows:

- Detection of charged particles and precise measurement of their location and direction.

- Determination of transverse momentum and sign of the charge of particles of momentum up to 50 GeV/c .
- Reconstruction of the vertex of the interaction, the secondary vertices and prediction of the point of entrance of the particle into the electromagnetic calorimeter.
- Determination of the multiplicity of charged particles originating from the interaction point for triggering.

The central tracking chamber is a multi-wire chamber working on the principle of a Time Expansion Chamber (TEC) [26]. TEC is built as a cylindrical structure around the beam pipe. The detection volume is formed by a 1.5 mm thick beryllium cylinder at the inner diameter, a 4 mm thick aluminium cylinder at the outer diameter and 4.5 cm thick aluminium end-plates. The wires are stretched along the beam direction and are supported by the end-plates. The inlet and outlet for the gas are also located on the end plates. The TEC operates with a gas mixture of 80% carbon dioxide and 20% iso-butane at a pressure of 1.2 bar absolute. The TEC consists of three parts as shown in figure 2.3, an inner chamber, an outer chamber and a Z-chamber.

The drift region in the chamber is divided into two parts, the low field drift region and a high field amplification region. This division is achieved by putting grid wires before the anode wires (see figure 2.4). This configuration optimizes the electron arrival-time distribution and the track length as seen by each anode wire.

The anode and cathode wires are stretched from one end-plate to the other, parallel to the beam pipe, forming planes which divide the whole TEC into 24 sectors in the outer TEC and 12 sectors in the inner TEC. The grid wires are stretched in the same way on both sides of the anode planes forming the two grid planes, one on each side of the anode plane. Each anode plane has 62 wires.

There are two types of anode wires, the standard wires for determining the position of the track in the R-ϕ plane and the charge division wires which determine the position of the track along the Z direction. Out of the 54 anode wires in an outer TEC sector, 14 have the left-right ambiguity resolved by reading out a set of 5 grid wires on each side of the amplification region. Comparison of the induced signals on these wires enables resolution of the left-right ambiguity for the corresponding anode wire. The anode and charge division wires are made of Tungsten and the cathode and grid wires are made of CuBe. The sensitive length of each of these wires is 982 mm. There are 6 standard and 2 charge division wires in each of the inner TEC sectors while the outer sectors contain 31 standard wires, 14 left-right ambiguity resolving wires and 9 charge division wires, giving a total of 62 wires per sector.

The Z-detector measures the position of the track along the Z-axis. It consists of two concentric cylindrical proportional chambers, with cathode strip readout, covering the outer cylinder of TEC. The strips of the 4 cathodes form angles of 90°, 70.1°, −70.1° and 0° with the beam direction. The effective length of the Z-Detector is 1068 mm, a thickness of 21.5 mm and an outer diameter of 980 mm. The polar angle coverage of the Z-Detector is $45° < \theta < 135°$.

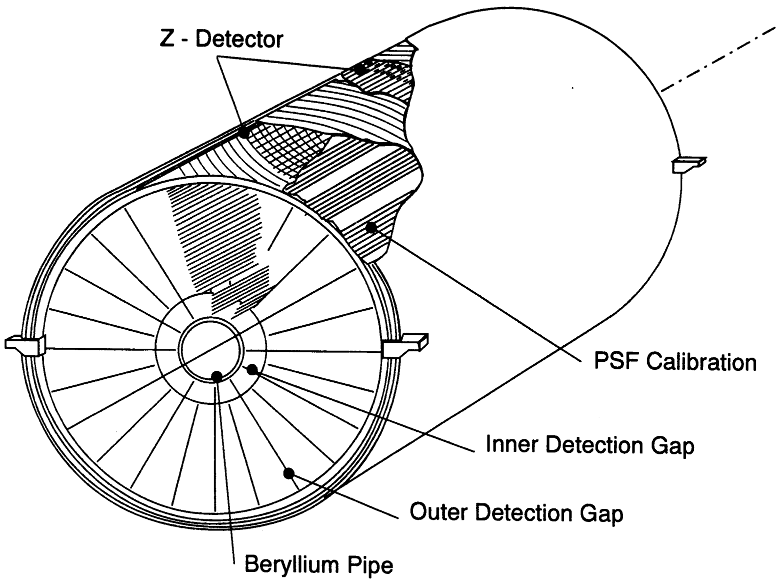

Figure 2.3: *The Central Tracking Chamber TEC*

The resolution obtained for a single point in the R-ϕ plane is 58 μm in the inner TEC chamber and 49 μm for the outer TEC chamber. The Z-chamber gives a position resolution of 320 μm just outside TEC [27].

2.2.3 Electromagnetic calorimeter

The electromagnetic calorimeter for L3 known as the BGO is made out of bismuth germanate crystals and is designed to

- measure the electromagnetic energy of particles in a wide range (100 MeV to 100 GeV).
- have a high stopping power for photons and electrons so as to get an accurate estimate of their energy.
- measure energy with a fine granularity so as to be able to determine with a high accuracy, the direction of the particles, especially photons, which leave no signature in the TEC.
- sustain the radiation damage from long periods of LEP operation.

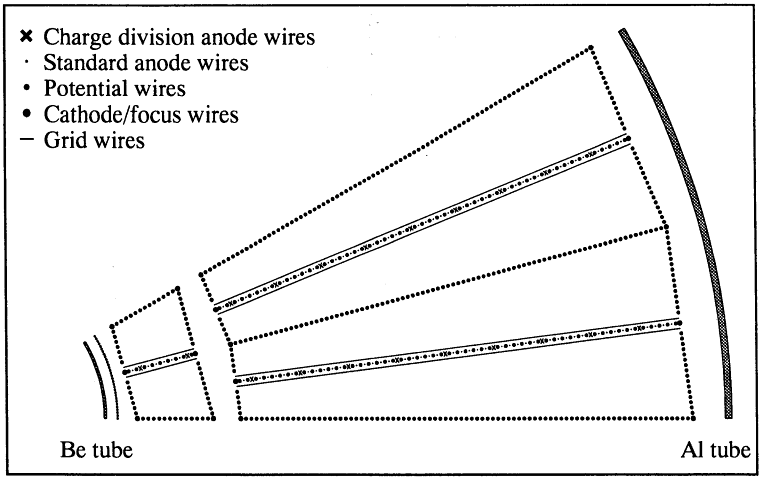

Figure 2.4: *One inner and two outer TEC sectors in the x-y plane.*

The material found, to meet best the above requirements is BGO ($Bi_4Ge_3O_{12}$), which is used both as scintillator and absorber. The $Bi_4Ge_3.O_{12}$ is made into crystals which are then machined into shape and polished. To contain the scintillation light in a crystal, the crystals are painted with a 40 to 50 μm thick layer of a high reflectivity paint. Figure 2.5 shows the typical shape and dimensions of a BGO crystal. The length of each crystal corresponds to 21.4 radiation lengths.

The shape of the BGO calorimeter is that of a hollow cylinder, called the barrel which surrounds the central tracking chamber TEC. The ends of the barrel are closed with endcaps also made of BGO crystals. The calorimeter can be sectioned into four main parts, the two half barrels and the two endcaps.

The crystals in the barrel and endcaps are arranged so that each of the crystals nearly points to the interaction point, exposing an area of 2×2 cm^2. All of the crystals have a small offset in the azimuthal angle ϕ to suppress photon leakage through the gap between the adjoining crystals. This configuration requires 24 different sizes of crystals as their shape changes slowly along the polar angle θ due to varying distance from the interaction point. There are some 11000 crystals in the whole of the BGO with 7680 of them in the barrel.

The mechanical structure holding these crystals in place is built of an epoxy-resin carbon-fiber composite. Cells are built over this structure for each crystal. The thickness of the mechanical barrel structure contributes 0.04 radiation lengths. The cell walls are made as thin as possible to minimise the dead areas. The total dead area due to crystal spacing is only 1.75 % of the total angular coverage of the BGO. The total polar angle coverage of the barrel BGO is $42° < \theta < 138°$.

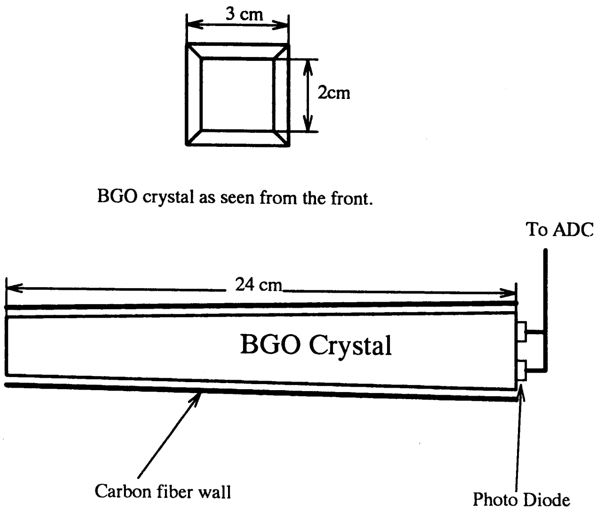

Figure 2.5: *A BGO crystal*

Each endcap has 1536 crystals and extends the angular coverage by 30° towards the beam pipe. The endcaps were put in place in the shutdown period between 1990 and 1991. Due to extra TEC shielding, which had to be installed to protect TEC from unwanted stray beam particles and due to the cabling of the TEC, the endcaps do not fit closely to the barrel but leave a hole between the barrel and endcaps. The endcaps also contain holes of 9×9 crystals through which the beam pipe of the RFQ is passed. The RFQ is a small accelerator installed in 1993, whose beam is to be used to calibrate the BGO.

Each crystal is fitted with two photodiodes glued to it at the rear end to collect scintillation light. The signals from the photodiodes are fed into preamplifiers also mounted behind the crystals. The amplified signals are then read out by the data acquisition system.

The energy resolution of the BGO varies from $\simeq$ 5% at 100 MeV to $\simeq$ 1.4% at highest energies (45 GeV). The spatial resolution above 2 GeV is better than 2 mm [27].

2.2.4 Scintillation counters

Scintillation counters are installed between the electromagnetic and the hadron calorimeter, with an azimuthal angle coverage of 93% and a polar angle coverage corresponding to $|\cos\theta| < 0.83$. They are used to veto cosmic muons and to trigger on the hadronic events. A cosmic muon can mimic a muon pair from an e^+e^- interaction, but it can be vetoed by considering the time difference of the hits on opposite scintillation counters.

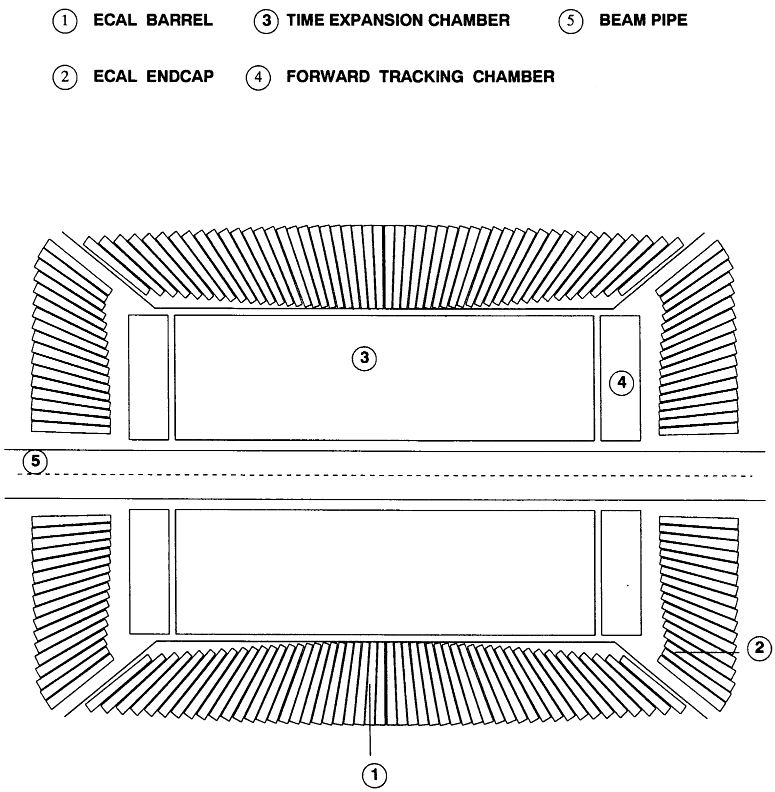

Figure 2.6: *The Electromagnetic Calorimeter BGO*

The difference for a cosmic muon would be 5.8 ns, whereas this difference for di-muon events is zero. The time resolution obtained by studying the time-of-flight of Z decays into muon pairs is 460 ps [27].

2.2.5 Hadron calorimeter

The hadron calorimeter for L3 is a sampling calorimeter and is called HCAL. It is designed to

- measure the energy of the hadrons using the total absorption technique together with the BGO calorimeter.
- stop all the showering particles and allow only the non-showering ones to reach the muon chambers.

- have sufficiently fine granularity to determine the spatial direction of energy flow.

The hadron calorimeter uses layers of proportional wire chambers as the active medium interspersed with layers of depleted uranium as an absorber. Uranium has a short absorption length so it gives a very compact medium for absorption of hadrons by showering.

The proportional wire chamber planes are made of brass tubes of equal length with a 0.3 mm thick wall and inner dimensions of 5×10 mm. The chambers operate with a gas mixture of 80% Ar and 20% CO_2. Gold-plated tungsten wires are used as the anodes which are crimped into gold-plated brass jacks. The jacks are held in place by plastic end pieces. The uranium is in the form of 5 mm thick plates sandwiched between the chambers. These chamber-uranium arrays are arranged into modules each of which covers an angle of $\Delta\phi=2\pi/16$ radians in azimuth and $\Delta\theta=\pi/15$ radians in polar angle. The arrangement of the chambers in the modules is such that alternate layers have their wires parallel and orthogonal to the beam direction. This configuration makes it possible to measure the θ and ϕ coordinates of the energy deposit. The so called long modules, which are positioned in the central part of the barrel, contain 60 planes of proportional chambers, 58 uranium plates and a top stainless steel plate whereas the short modules, positioned away from the interaction point, contain 53 chamber-planes, 51 uranium plates and a top stainless steel plate.

The calorimeter is divided into barrel and endcaps. The barrel covers the angular region $35° < \theta < 145°$, whereas the endcaps cover $5.5° < \theta < 35°$ and $145° < \theta < 174.5°$. Figure 2.7 shows a cutout view of the hadron calorimeter and its endcaps.

The barrel part has a modular structure consisting of 9 rings with 16 modules each. The central ring, which has long modules, is centered at the interaction vertex. It is flanked on each side by one long and three short module rings. The hadron calorimeter is 4725 mm long; it has an inner radius of 885 mm for the inner rings and 979 mm for the outer rings. The barrel weighs 261 tons.

The endcaps for the hadron calorimeter also have a modular structure. Each endcap consists of three rings, one outer and two inner. Each ring is further split vertically into 'C' shaped half rings resulting in 12 modules. Because of the modular structure, the endcaps can be installed and removed easily allowing a fast access to the inner detector components for service, if necessary. The number of channels read out is reduced by grouping the wires into towers [25]. Each tower covers $\Delta\theta=2°$ and $\Delta\phi=2°$.

The total energy of Z decays into hadrons can be determined using the calorimeter system with a resolution of 10.2%. The fine segmentation of the calorimeters allows the determination of the jet axis with a resolution of approximately 2.5° [27].

A muon filter is installed on the inner side of the support tube in front of the hadron calorimeter, which consists of 8 identical octants. Each octant has 6 layers of brass 1 cm thick which act as absorber and 5 layers of proportional tubes. The proportional counters and absorbers form alternate layers. The last layer of absorber, closest to the support tube is a 1.5 cm thick plate which matches the shape of the support tube. In total, the muon filter adds 1.03 absorption lengths to the barrel hadron calorimeter.

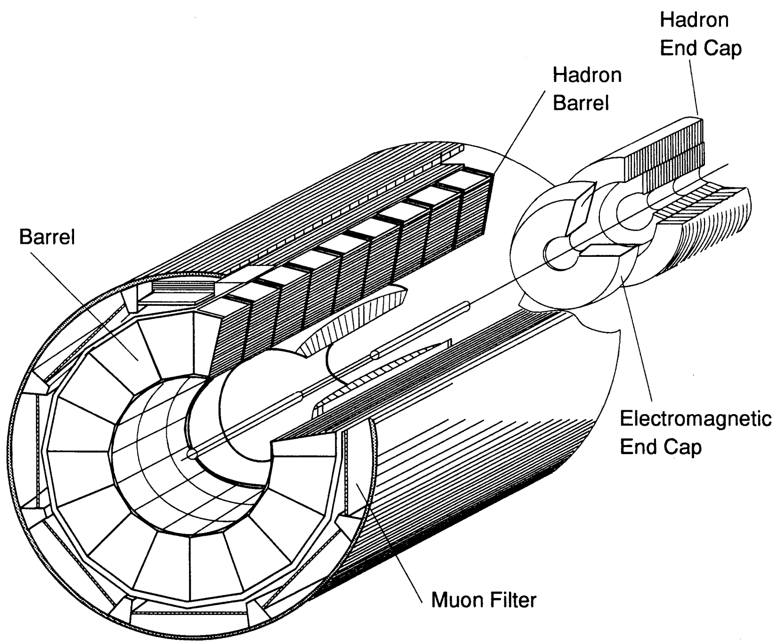

Figure 2.7: *The Hadron Calorimeter HCAL*

2.2.6 Muon chambers

The L3 muon chamber system is designed to

- measure the momentum of high energy muons with an accuracy of Δp/p = 2% at 50 GeV.
- accurately determine the position of muons in space.

To achieve this accuracy, drift chambers are installed between the support tube and the magnet. They measure the curvature of the muon tracks in the bending plane of the magnetic field.

The muon system is octagonal in shape and consists of two Ferris wheels, each with eight independent units called octants. Each octant consists of three layers of chambers mounted on a special support structure which slides over the support tube and into the magnet. The muon chamber covers the full azimuthal angle, but in the polar angle the coverage is $35° < \theta < 145°$.

An octant is divided into three layers of drift chambers, an inner layer (MI) a middle layer (MM) and an outer layer (MO). There are two types of chambers: the P-chambers, which measure the momentum of the muon tracks and the azimuthal angle ϕ, and the Z-chambers which measure the angle θ. The inner and outer layers have both types of chambers; the middle layer has only P-chambers. Figure 2.8 shows a schematic diagram of an octant of the muon chamber system.

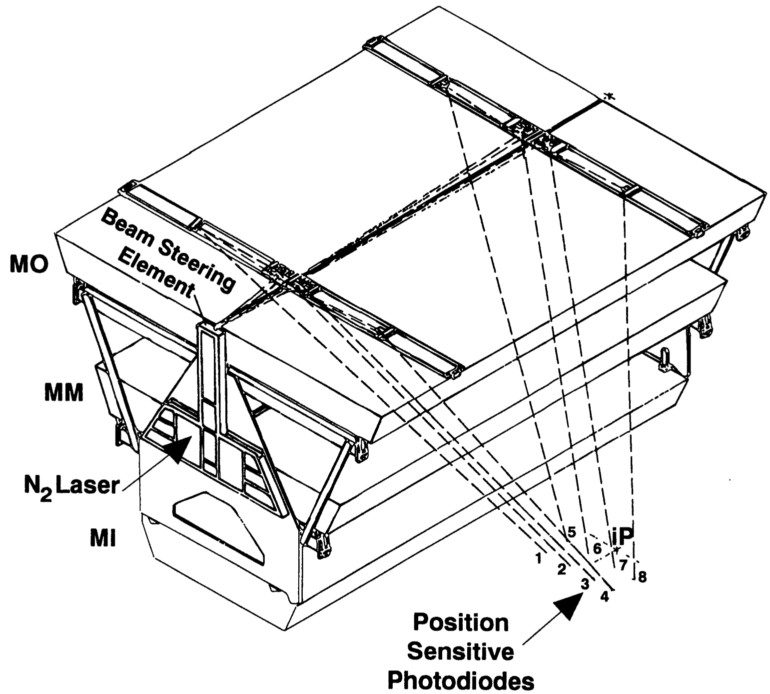

Figure 2.8: *A Muon Chamber Octant*

Each P-chamber is divided into a number of drift cells, the MI chambers consist of 19 cells each, MM chambers have 15 and the MO have 21. The drift cells in MO have 16 signal wires, MM have 24 signal wires and MI have 16 signal wires. The signal wires are alternated by field shaping wires. The P-chambers use a gas mixture of 61.5% of argon and 38.5% ethane [28]. The wires are stretched in the Z-direction across bridges made of pyrex glass and carbon fiber. There are three bridges in each chamber, two at the ends and one in the middle, the latter is to prevent sagging of the wires due to gravity. Each P-chamber contains about 320 wires.

The Z-chambers cover the outer and inner sides of the MI and MO chambers. These chambers have two layers of drift cells, with their wires in the X-Y plane, offset with respect to each other by half a chamber. The offset in chamber positioning resolves the left-right ambiguity of the tracks. The gas mixture used is 91.5% argon and 8.5% methane.

Systems for alignment of the wires in the chambers and the alignment of the chambers relative to those in other layers are built-in with the chambers and the mechanical structure of the octants respectively.

The resolution obtained for the muon chambers by analysing the reaction Z $\rightarrow \mu^+\mu^-$ is estimated to be $\sigma(E_{\mathrm{beam}}/E_\mu) = 2.5\%$ [27].

2.2.7 Luminosity monitor

The integrated luminosity of a LEP running period is measured by means of an electromagnetic detector made of BGO crystals. The cross section for Bhabha scattering ($e^+e^- \rightarrow e^+e^-$) is well known, thus by counting the number of Bhabha events in a fixed angular region during a running period, the integrated luminosity for the period can be found as:

$$L_{\mathrm{int}} = N_{\mathrm{Bhabha}}/\sigma_{\mathrm{Bhabha}}.$$

The luminosity monitor comprises two identical modules positioned on either side of the interaction point. Each module consists of a calorimeter containing 304 BGO crystals. The angular coverage of the luminosity monitor is from 24.93 to 69.94 mrad in θ with respect to the beam line. Each crystal carries a photodiode to collect the scintillation light. This produces an analog signal which is read out to provide a trigger and is digitised to provide a measure of the energy. The energy resolution of the calorimeters is 2% at 45 GeV, the angular resolution is 0.4 mrad in θ and 0.5° in ϕ [27]

2.2.8 The trigger

The function of the trigger system is to

- determine if and when an e^+e^- interaction has taken place,
- to initiate the recording of the event if an interesting interaction has indeed taken place; otherwise to clear the electronics and get the detector ready for the next beam crossing. The tape writing rate is thus reduced to a few Hz from the beam crossing rate of 45 kHz,
- to monitor the detector parameters for detector calibration and safety.

The online computer system consists of a VAX 8800 system clustered with five smaller monitoring VAX systems, one for each main subdetector. The cluster is connected to personal computers which monitor the detector for safe operation and to workstations which are used for controlling the running conditions of the detector. The data from an event are read from the front-end electronics and are buffered during the time that the triggers need for making a decision. In case of a positive decision, the data are digitised and written out to tape, otherwise the buffers are cleared. The only dead time introduced in the data taking is due to the digitisation of the detector signals in case the event is accepted by the trigger system. The trigger system consists of three levels with increasing complexity and sophistication.

The LEVEL-1 trigger is a logical OR of the trigger conditions as obtained from five sources: the calorimeter trigger, the muon trigger, the TEC trigger, the scintillator trigger and the luminosity trigger.

The calorimeter trigger bases its decision on the total energy deposited in the calorimeters and the number of clusters of localised energy deposits found in the calorimeters. The muon trigger searches for a track in the muon chambers which has a scintillator hit in coincidence. The TEC trigger searches for back to back tracks within a cone of 20° and the scintillator trigger searches for scintillator hits in coincidence.

If the event is accepted by any of the five sources of LEVEL-1 trigger, the signals are digitised and the higher level trigger LEVEL-2 comes into action. If, however, the event is rejected by the LEVEL-1 trigger, the electronic buffers are cleared and the data acquisition is reinitialised for the next beam crossing.

The LEVEL-2 trigger uses the coarse data used by LEVEL-1, the results of LEVEL-1 and some more data that have become available at this step. Events selected by more than one sources of LEVEL-1 trigger, pass through LEVEL-2 without any processing. LEVEL-2 improves the LEVEL-1 results by spending more time per event in order to correlate information from different subdetectors without introducing extra dead time. The LEVEL-2 trigger is able to remove calorimeter triggers arising from electronic noise and some of the TEC triggers generated by beam gas or beam-wall interactions as well as by synchrotron radiation. A positive decision at LEVEL-2 results in the collation of the event data by an 'event builder' and its transfer to LEVEL-3, whereas a negative decision results in resetting of the event builder.

The LEVEL-3 trigger uses completely digitised data for the event and processes the event using several algorithms corresponding to the LEVEL-1 trigger that selected the event. The calorimeteric algorithms scrutinise the event with more precise thresholds and noise problems are further reduced. In TEC triggered events, TEC tracks are required to have a correlated energy deposit in the calorimeters and are examined for a common vertex. The muon triggers are passed through more stringent scintillator coincidence criteria. The luminosity trigger events pass through untouched. If a positive decision is made by LEVEL-3 trigger, then the event is written to tape.

Chapter 3

Production Control System for L3

3.1 Introduction

It is very important to have a record of the progress of an experiment. One needs to keep track of all the happenings during an experiment, so as to be able to trace back and reproduce the conditions as they existed at some point in the past. This becomes increasingly difficult as the size of the apparatus increases and it becomes more complex.

The size and lifetime of the detectors in high energy physics has been growing with the energy of particle colliders. The last few decades have seen the introduction of electronic detectors to take the place of the earlier visual detectors such as bubble chambers. Electronic detectors have the advantage of high speed and more selective triggering. In contrast to visual detectors, electronic detectors can thus accumulate a large number of interesting events in a short running time, provided of course that the accelerator delivers high luminosity. Present-day electronic detectors are complicated systems and require sophisticated software to process the raw data collected.

A typical detector at LEP occupies a volume of the order of 1000 m^3, the number of electronic channels of a detector which are read out are around a million, the duration of data taking is of the order of a decade and the number of events collected by a LEP detector is of the order of 10000/day. It is desirable to do a prompt analysis of the data collected and to keep track of all the steps taken during the analysis. The lifetime of data is another important consideration. The data collected today is stored on magnetic tapes and can be reanalysed at some time in the future if new ideas arise which could be tested with the data already available or to get better results with increased statistics after many years of data collection. This means that the data live on for decades and anyone reanalysing the data in the future must have information about the preprocessing of the data available to him.

With millions of events to analyse per year, one runs into the problem of finding the computer power needed for data analysis. It is often difficult to provide sufficient computer power at the site of the experiment. One has then to rely on the computing power available at the institutes collaborating in the experiment. This in turn means that the information necessary to run a data processing job must be available remotely.

Furthermore, results of recently run data processing jobs must be available to the entire collaboration.

With the above mentioned points in mind it seems very logical to go from the hand-written log-book of the past, to a computer aided log-book for the new generation of experiments such as L3. Automation of the whole process is also desirable in order to minimize human intervention with its inevitable human errors. In L3 this is achieved by a "Production Control System" using a database, which will be described in this chapter.

3.2 Processing of L3 data

Processing of data involves the following main steps:

- Reading and decoding the data from the online data acquisition system.
- Reconstruction in the different subdetectors of L3.
- Global reconstruction using the information from the previous step to produce physically meaningful quantities.

The data acquired by the online data-acquisition system is written onto IBM 3480 tapes in the form of ZEBRA-FZ [29] data records. The data-acquisition system also performs the calibration of different detector components, the results of which are written out to a database. The data tapes along with the relevant information on the data acquisition conditions are sent to the offline data analysis system. The format of the data is checked online in a step named "Validate" to make sure that the data have the right format as required by the reconstruction software and to detect as soon as possible if some of the detector components are not functioning properly.

REL3 is the software responsible for steering the reconstruction phase of the analysis. REL3 decodes the data from the ZEBRA-FZ format and stores them in the form of ZEBRA banks. The data are then calibrated and/or corrected using information stored in the database. This step is called the preprocessing of the data. The individual data objects after preprocessing correspond to the digitised hits in different detector components.

After data preprocessing, reconstruction in different subdetectors of L3 takes place. In this phase data for each subdetector, namely TEC, SCINTILLATORS, BGO, HCAL, and MUON CHAMBERS are reconstructed independently under the control of REL3. The result of this component reconstruction are data objects which are clusters of energy deposits in the calorimeters and tracks in the tracking chambers.

Once the component reconstruction has been performed, the global reconstruction of the data takes place. This is done by the AXL3 software (Across L3 reconstruction) again steered under the control of REL3. During this phase of reconstruction, the relationship between objects in different subdetectors is established and the data objects representing different physical entities are produced. Following is a list of the data objects produced by the AXL3 software which are then available for physics analysis:

1. ASRCs are the smallest resolvable clusters produced by combining the clusters of energy deposits in the electromagnetic and hadronic calorimeters. Each ASRC can be considered to be a particle in the detector although in part it may be the result of more than one particle. Information on the direction of energy flow is also available.

2. ATRKs are the tracks formed by the track fitting algorithm in the central tracking chamber TEC using the hits found on the wires. Track parameters, momentum, distance of closest approach to the interaction vertex, charge of the particle leaving the track and azimuthal angle ϕ are available. The polar angle θ is determined by matching tracks to calorimetric clusters.

3. AMUIs are the objects comprised of a TEC track, hits in the calorimeters and a correlated track in the MUON chambers. These objects represent a muon crossing the detector.

4. ASJTs are the jets reconstructed from the ASRCs.

5. AJETs are the jets as reconstructed using only information from the data in the calorimeters.

The events are passed through a set of very loose selection criteria to eliminate unwanted events and to classify the events under different physics categories such as $q\bar{q}$, Bhabha, $\tau^-\tau^+$, etc. Corresponding information is written out with the event. Events of each category are written to a separate file.

There are a number of parameters which can be changed during the reconstruction of the data producing different results. An example is the use of different calibration constants which are calculated from the data in an iterative process and improve each time the data are reprocessed. These calibration constants are stored in the database. One needs to keep track of the identification of the set of parameters used in a particular reconstruction job.

3.3 Processing of L3 Monte Carlo events

The production of Monte Carlo events involves the following steps:

1. Generation of physics processes using the Monte Carlo event generators,

2. Tracking of the particles produced by the event generators through the detector,

3. Digitization of detector response to produce the same data format as is produced by the online data-acquisition system,

4. Reconstruction of the events by the same programs as used for real data reconstruction.

The event generation, which takes the role of actual collisions in LEP, is performed using one of the many physics event generators available for different possible final states. Each of these generators has a number of parameters which can be changed to produce a desired effect.

Output of the event generators is used as input for the L3 detector simulation program called SIL3. Based on GEANT [30], SIL3 simulates the response of the detector to the particles as they would traverse the detector. The detector response is then digitised to produce the same form of output as is produced by the actual data-acquisition system. The reconstruction of the simulated events then follows the same stream as the real data. The analysis stream of data and Monte Carlo is shown in figure 3.1.

As is evident from the above discussion and as can be seen from figure 3.1, a large number of operations have to be performed on data and Monte Carlo events before they can be used in any physics analysis. At every step there is a number of parameters that determine how the data are processed. For physics analysis of data it is necessary to know what parameter settings were used for processing the data. A database is used to keep track of this entire process.

3.4 DBL3 the database package for L3

The need for a database package for L3 became evident in the very early phase of construction of the experiment. The question was which database system to use? A range of tests were conducted on commercially available database packages and packages written for HEP [31]. On the basis of these tests it was decided to write a package of our own since a homemade database system would be cheap, easily portable to other computers and could be tailored to the needs of the experiment. A full description of the DBL3 package can be found in [32]. For the sake of completeness a brief description of DBL3 is given below.

The DBL3 package is written on top of the ZEBRA-RZ direct access package written at CERN [29]. The ZEBRA-RZ package provides a structure in which data can be stored in a hierarchical manner in the form of directories similar to the UNIX file system. An entry in a directory has two components, "keys" which are used to identify a set of data and the data themselves. Each key is a word of 32 bits. ZEBRA-RZ allows a maximum of 100 keys for each data object.

DBL3 uses the first 7 keys as "Standard" keys. Thus, every object must have at least these first 7 keys. The definition of the first 7 keys is:

- Key 1 = Serial number of the object (internal to DBL3)
- Key 2 = Used for update mode (internal to DBL3)
- Key 3 = Start time of validity period of data object
- Key 4 = End time of validity period of data object

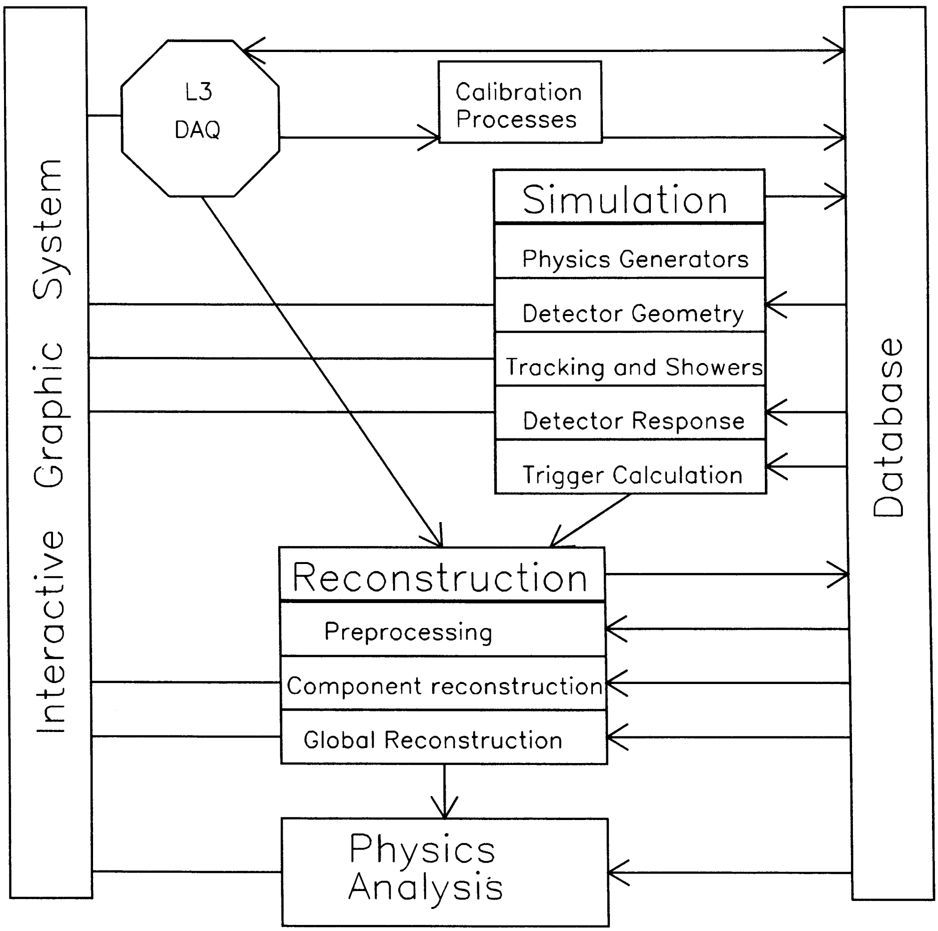

Figure 3.1: *Flow of analysis stream for data and Monte Carlo*

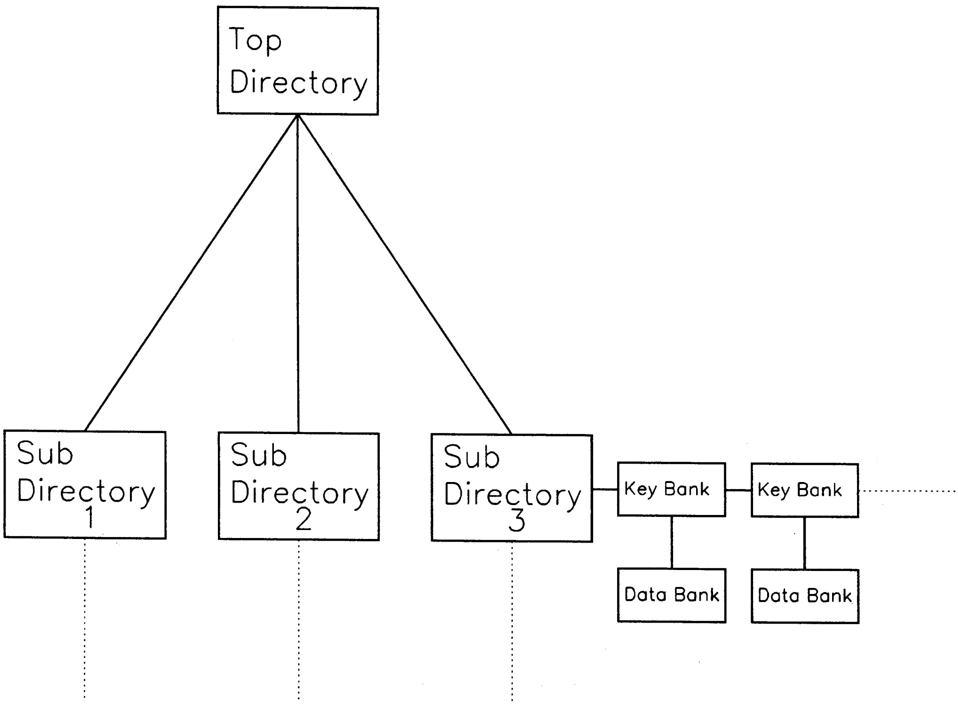

Figure 3.2: *Directory key structure of the ZEBRA-RZ package*

- Key 5 = Identity of program inserting the object
- Key 6 = Bit information on packing type (internal to DBL3)
- Key 7 = Time of insertion of the data object (internal to DBL3)

The start and end of the validity period (in date and time) of the data objects are packed to an accuracy of seconds into one word, whereas the insertion time is packed to an accuracy of minutes. Data and keys are stored in separate ZEBRA banks with a key bank linked to the corresponding data bank as shown in figure 3.2. The keys can be cached into memory for searching for the data required. Once identified the data can be loaded into memory thus making an economical use of the memory and achieving fast search times for data objects. The keys can also be used to store single word data objects which are frequently used and thus can be retrieved in a real time orders of magnitude faster than that required if they were resident on disk as data objects.

In addition to the facilities provided by DBL3 such as data compression by packing, real time optimisation by directory partitioning, and a dictionary of the alias names for data, DBL3 has the additional features, described briefly below, which are of great importance for production control:

ASCII data objects

DBL3 allows to store and retrieve data objects of data type ASCII in the database. The maximum record length allowed for such data objects is 80. This is of great importance for production control since production jobs produce some information about their performance in ASCII format. Job submission information is also stored in ASCII format.

Interactive interface

The DBL3 package allows to query the database interactively through an interactive version of DBL3 based on the KUIP package [33]. This feature is useful for the people doing analysis when they want to make queries about the output of a particular production job. This feature is also useful for the people running the production jobs to make regular checks on the running jobs.

Journaling

In order to preserve the integrity of the database in the event of a computer crash, DBL3 provides the feature of journaling the updates made to the database. While updating the database, DBL3 makes a sequential ZEBRA-FZ file in which it keeps these updates. In the case of a computer crash or database corruption, these sequential files known as the "journal files" can be used along with the last backed up version of the database to obtain an uptodate version. This feature is also exploited for updating the remote databases through servers.

L3DBSM

DBL3 has an auxiliary package called L3DBSM which is a set of servers which can be run on the main computer, where the "Master" database resides (in this case "LEPICS", an IBM 3090/200J mainframe) and on the remote computers. Any updates to the database, requested by a "client" process attempting to write to the database on the main computer or a remote computer, are given to the server on the main computer. The server makes the update to its own database and sends a copy of the update as a journal file to the remote servers which in turn make the updates to their copies of the database. This system of servers and clients makes concurrent writes to the database possible. It also ensures the synchronisation of all the databases residing on different computers. A schematic design of this "Client-Server" environment is shown in figure 3.3.

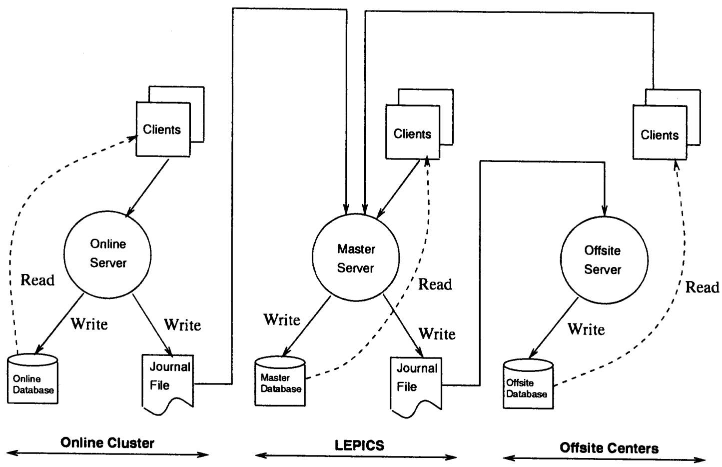

Figure 3.3: *Client server environment of the DBL3 package L3DBSM*

3.5 Production control

Having briefly described the tools available for implementation of a production control system, we now turn to describe a few important concepts that are used in the implementation of this system.

3.5.1 Production programs

The computer jobs up to and including the reconstruction of data and Monte Carlo, run in a controlled fashion by an officially appointed group, are defined as "Production Jobs" and their output files are used in the physics analysis. Any of the programs which are run as Production Jobs are thus defined as "Production Programs". Examples are Monte Carlo event generators, the simulation program SIL3 which simulates the effects of the detector on the generated events and digitises the output, a reconstruction program REL3 which converts the digital signals into meaningful quantities such as energy deposits in different parts of the detector and track trajectories. A standard set of procedures which produce the executable modules of the Production Programs are also categorised as production programs. The computer code for all the production programs is maintained using the code management package PATCHY [34].

3.5.2 Identification of programs

Although great care has been taken in writing the software for L3 to make the code portable to a wide range of computers, some system dependent features were unavoidable. An example is the FORTRAN file opening which is different on different computers.

Most programs can be run in different modes of operation. For example, the simulation program SIL3 may be run to create the simulation library, to generate 'Frozen Shower' files, to create program and detector initialisation structures, to go through a tracking phase with recording of hits or to run a digitisation phase with or without noise addition. All of these operations done separately or combined together can be considered as different modes of operation.

In order to identify a program for a given computer at a given computer center, we use the following convention: Each program is identified by a program identifier 'P', a mode of operation 'M', and a code for the computer center 'CC' where it is supposed to run. Thus we get a unique identifier 'PMCC' for every program, for every mode of operation, at every computer center. These three components in actual implementation are integer numbers assigned to each field and stored in a file from where they can be retrieved using alias names. The 'P' and 'M' fields each occupy 3 digits of the 6 digit integer number forming the 'PM'. The three digits of the 'M' field are further split into 'M_{DC}' the two left most digits, and 'M_{IO}', which identify the datacard alterations and the input/output alterations, respectively.

3.5.3 Identification of jobs

The output of programs depends on a number of factors such as the detector conditions, the calibration constants that are used for different subdetectors and the program parameters set via datacards. It is very important to know which output file is the result of what program run. To ensure this, each job is assigned a unique identifier, the JOBID, and this JOBID is incorporated into the names of the output files. One constraint in deciding the file names for output files is that many production jobs are run on IBM computers with the VM/CMS operating system. In this system, files are identified by a filename and a filetype, each of which can be no more than eight characters.

In order to overcome this limitation , we have chosen to construct the JOBID from a sequentially increasing number (given out by a server residing in the computer itself) and the computer center number 'CC':

$$\mathrm{JOBID} = \mathrm{JOB\_NUMBER} \times 100 + \mathrm{CC}.$$

For use in the filename of the files produced in a job, the JOBID is converted to base 36 using the alphanumeric characters. Using this technique and taking only 6 characters of the 8 characters allowed, we are able to construct more than 21 million unique job identifiers for jobs on any computer center CC. All the files produced in a job are given the same filename which is constructed from the JOBID and two characters identifying the program. The filetype is used to identify the different files that are produced in the same job. An example of a JOBID and the corresponding files is as follows:

- Decimal JOBID = 160 (Job number 1 on computer number 60)
- Base 36 Jobid = 00004G.

If the job were a reconstruction program run, then an 'RE' is prepended to the JOBID. Different files produced during this run could be:

- RE00004G.MDRE, the Master Reconstructed data set,
- RE00004G.PDRE, the Physics Reconstructed data set,
- RE00004G.MDSU, the Master summary of the reconstructed data set,
- RE00004G.SMRY, the summary of the program run.

In this way we are able to keep track of the different files that are produced in a particular program run by using the JOBID of the run.

3.5.4 Datacards

The L3 software provides flexibility in running programs by allowing the mode of operation and other program parameters to be changed by the use of the FFREAD (Free Format READ) package [35]. This package reads records (for historical reasons called datacards) containing a key word followed by parameter values. The datacards in production jobs play a key role in determining the output of the programs. It is thus very important to know the specific set of datacards that was used in a particular job. Each set of datacards that is used in production is allotted a 'Datacard ID' which corresponds to a particular program ID, mode of operation and computer center. The datacard IDs are integer numbers incremented by 1 each time a new set of datacards is inserted into the database for a particular PMCC.

3.5.5 Template

On different computers, the production jobs perform a set of operations at the beginning and end of every job. These operations are the same for every job with the same PMCC and thus can be standardised for every computer. This standardised set of instructions is called the template and is unique for every computer. It contains the initialisations, reading in of any parameters changed by the operator, setting up the job for the machine configuration and some free fields which are filled in automatically according to the run time instructions provided by the operator, e.g., the datacards and the name of the module to be executed. The template also contains the instructions for inserting the information about the job performance after the completion of the job into the database. The cleaning-up of the disks after a job has completed its task is also a part of the template. Each template is allotted a 'Template ID' which is an integer number incremented by 1 every time a new template is added to the database for a given PMCC.

3.5.6 Special conditions

The datacards described above are used to change some parameters for a particular job, but sometimes more is needed than just the change of a datacard. For example, a particular analysis may require a sample of Monte Carlo $\tau\tau$ events where all the τs decay to muons. There might also be special conditions for the simulation of a particular set of events, say a different threshold of a hit in the muon chambers. Such special treatment of a particular set of events must be kept track of. Since the bulk of events processed in the Monte Carlo production are the standard events and since the possible number of combinations of the special conditions is huge, it is not practical to store separate sets of modules, datacards, and templates for all such sets of events into the database.

To cope with this problem, the concept of special conditions is used. If there are some special features for a particular set of events and the number of such events required is not large enough to make a separate processing stream with a module, datacards and a template, then such a special condition is allotted an integer number. These numbers are kept in an ASCII file with the description of the corresponding special treatment. The special condition numbers are logged into the database by the jobs as keys in the relevant directories. At a later time, a user can find some special events by looking in the special condition file, finding the condition number and then searching the database to find all the JOBIDs that have been processed with the particular special condition.

3.5.7 Module

As explained earlier, every machine needs a different executable module for a program due to the difference in system configuration and due to a set of different FORTRAN system dependent features. Furthermore, the constant evolution of the detector hardware and subsequent program revisions require many versions of a given program. To identify executable modules for different machines and different program versions, each module is allotted a 'Module ID' which is an integer number made up in the same way as explained for the datacard and template ID.

3.6 L3 run control database

The Run Control database 'L3RC DATABASE' is designed to keep track of the running conditions of LEP and L3. This database also serves as a log book for the production jobs. A schematic layout of the database is shown in the figure 3.4. A brief description of the directories of the database and their contents can be found in appendix A.

It should be noted that for production control a maximum use of the keys has been made to allow fast access to data. Many of the directories do not contain any data objects but consists only of keys. Such directories are used only to make cross reference between different objects in the database.

3.7 Performance

The production control system for data was installed at the same time as L3 started collecting data in August 1989. The production control system for Monte Carlo event processing was put into operation in mid 1991.

3.7.1 Data

As a policy, the processing of data is done on LEPICS, an IBM 3090/200J mainframe dedicated to L3. The number of events accumulated by L3 since it started collecting data in 1989 is of the order of 2.5 million. The system has worked reliably and has been able to keep track of the detector conditions and off line processing of the data. Figure 3.5 shows the steps involved in processing the data, where 'DAQ' stands for the data acquisition system, 'CAL 1' is the process that determines calibration constants using online data, 'DBL3' stands for the database, 'REL3 PASS 1' and 'REL3 PASS 2' stand for reconstruction processes, 'SPLT' and 'CCAT' stand for splitting the data sets and their concatenation as explained in section 3.2 Finally, 'SCAN' stands for the process of scanning the events visually on workstations.

3.7.2 Monte Carlo

In the case of Monte Carlo, the setting-up of the system was a bit more complicated. The computer power required to simulate the detector response to the Monte Carlo generated events is about 60 times more than that required for reconstruction. Furthermore the number of parameters that can be changed in the Monte Carlo jobs is much larger than for data.

The Monte Carlo production jobs are submitted by an officially appointed Monte Carlo group at CERN. The event generation part is always done at CERN. The reasons for adopting this policy are:

- Mostly the people doing analysis and asking for a particular set of special events are at CERN, so processing the special events at CERN allows for better communication and fast processing.
- Since running events with special conditions involves special procedures, it is better not to spread such complicated tasks among too many people.
- The computer time needed for event generation is quite small as compared to the time needed for detector simulation.

However, for simulation use has been made of the computing resources of the collaborating institutions wherever they were available. The central system is setup on the Apollo workstations at CERN. These Apollos along with CSF (Central Simulation Facility) [36], a farm of HP 9000/720 and HP 9000/750 workstations, also do some simulation work. The remote computing centers are sent the job files ready to run on their machines, these jobs automatically produce and send the updates to the database through the server system as explained in section 3.4. This system requires minimum human intervention and has worked reliably.

Reconstruction of the simulated events is not as time consuming a process as the simulation. The events simulated at the off-site centers and also those simulated on-site are reconstructed at CERN. This policy ensures that the same reconstruction program is used for both data and Monte Carlo.

Figures 3.6, 3.7, and 3.8 show the steps involved in event generation, event simulation and reconstruction of the Monte Carlo events, respectively.

To date over 10 million Monte Carlo events have been processed and the system has been able to keep their record efficiently.

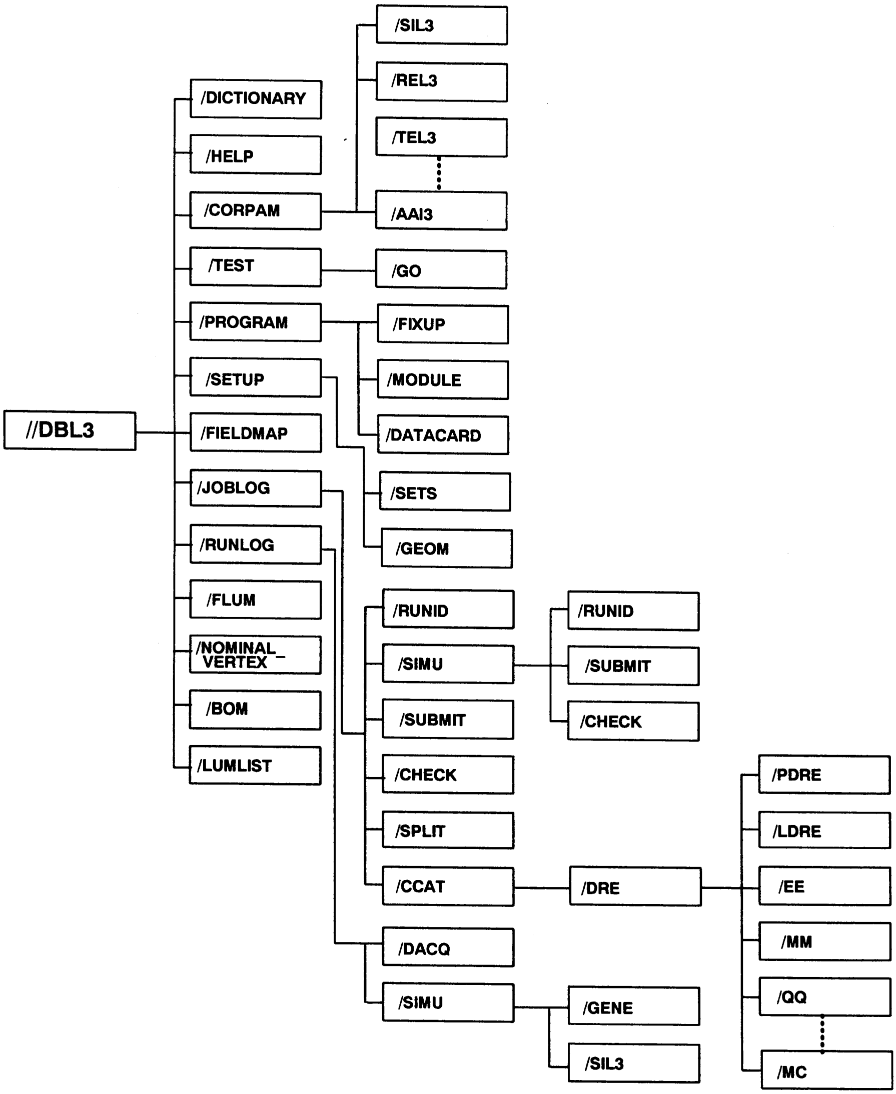

Figure 3.4: *Directory structure of the L3RC database*

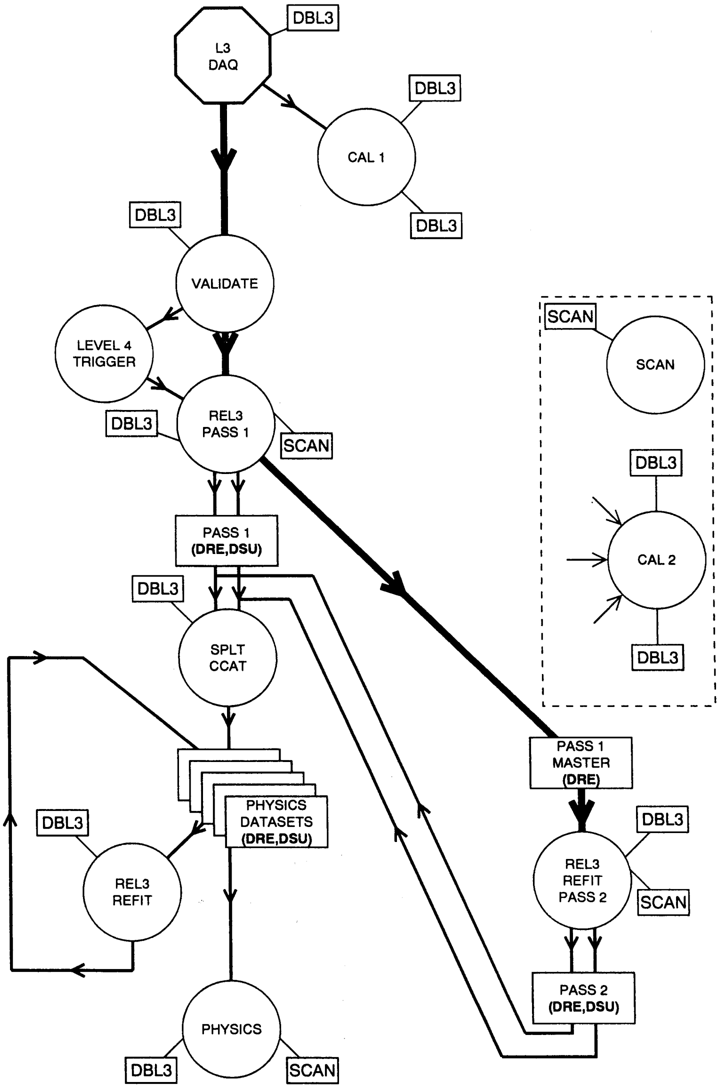

Figure 3.5: *Figure showing the steps involved in reconstruction of L3 data*

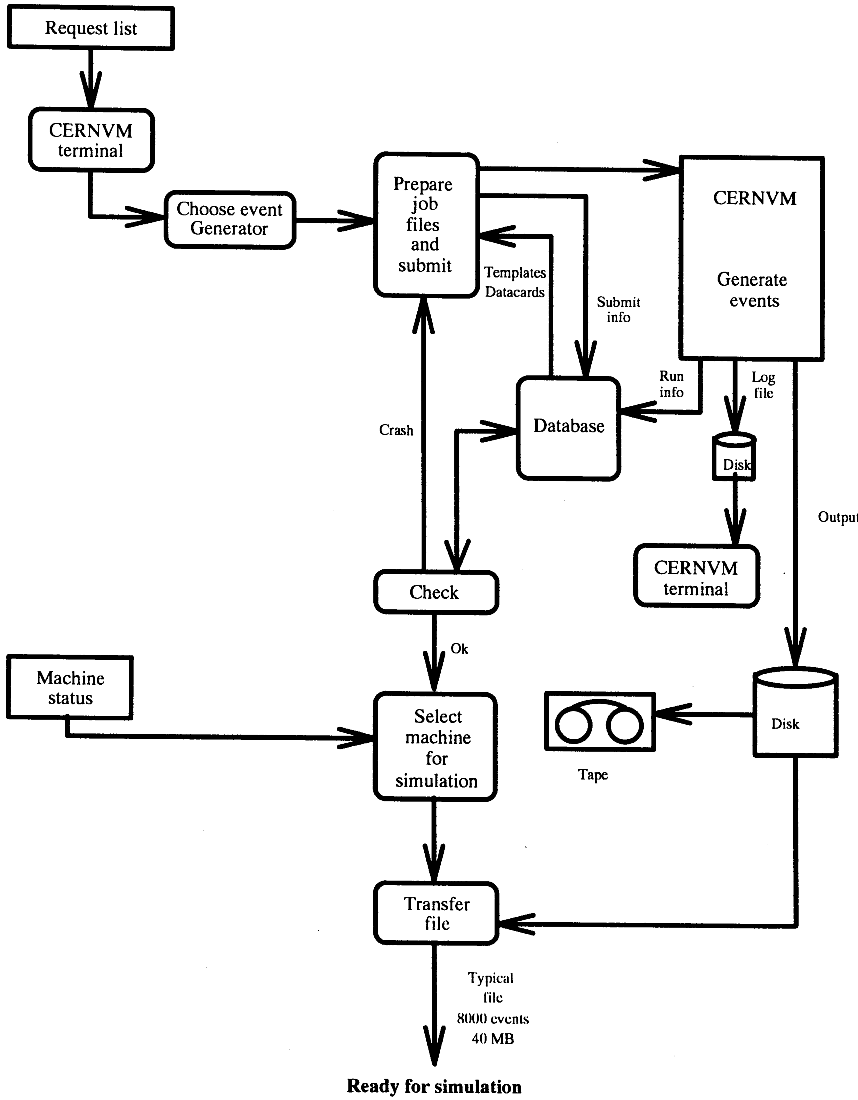

Figure 3.6: *Flow diagram showing the steps involved in generation of Monte Carlo events using different event generators.*

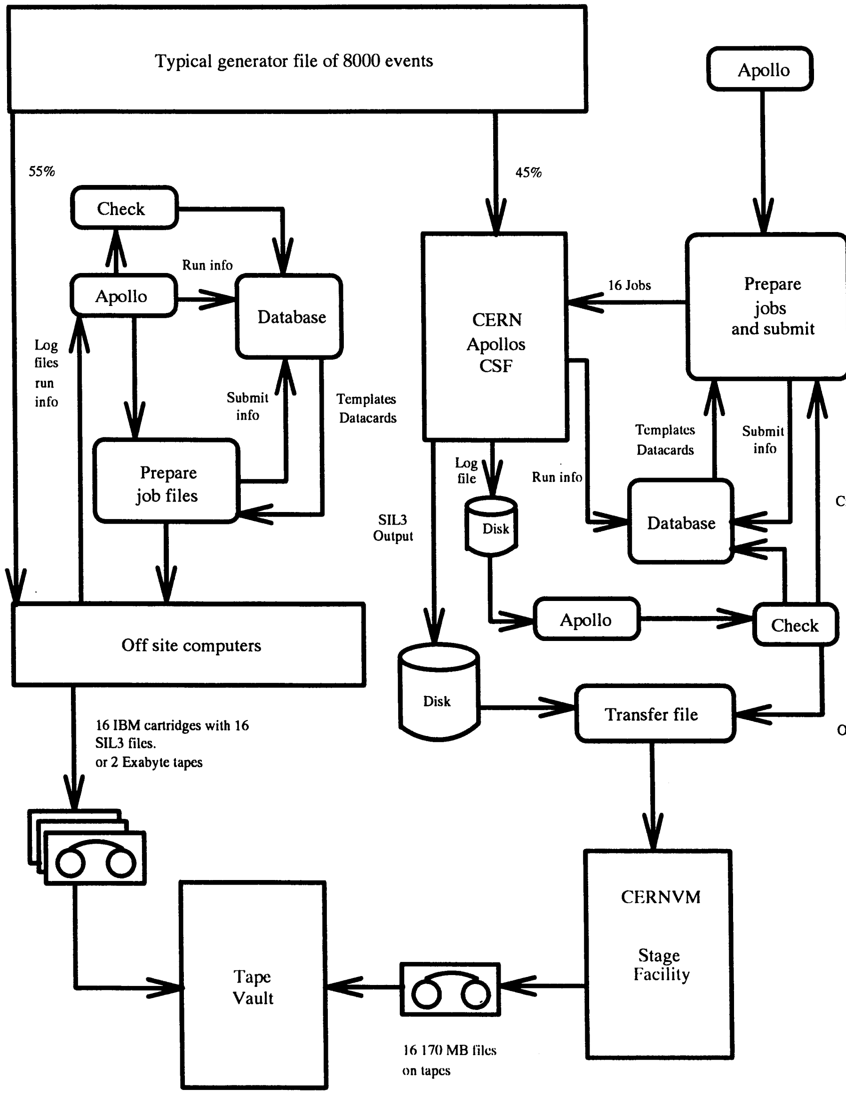

Figure 3.7: *Flow diagram showing the steps involved in simulation of Monte Carlo events using different event generators.*

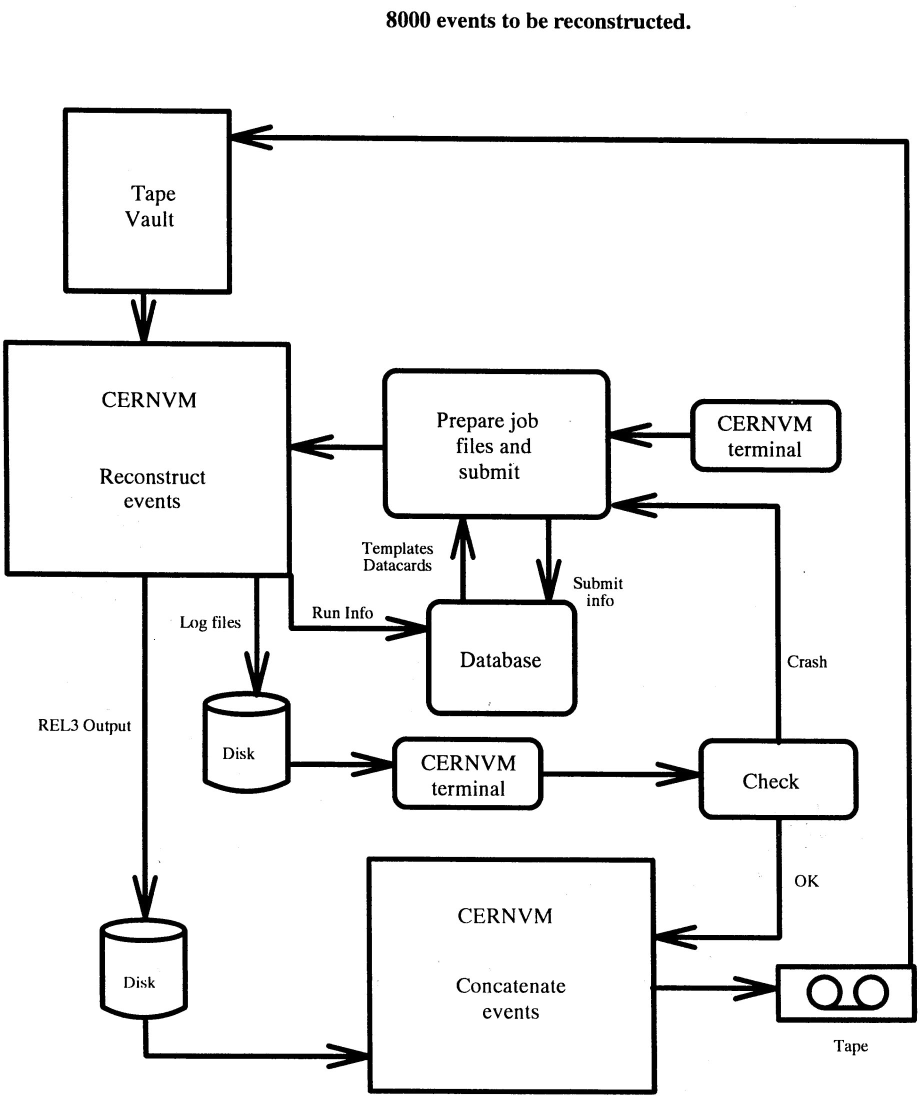

Figure 3.8: *Flow diagram showing the steps involved in reconstruction of Monte Carlo events using different event generators.*

Chapter 4

Event Selection

4.1 Introduction

The trigger for the L3 data-acquisition system is designed to accept events arising from e^+e^- interactions with a high efficiency, while rejecting most of the background processes such as beam-gas or beam-wall interactions, cosmic rays and synchrotron radiation [27]. However, in order to obtain a high efficiency, the selection criteria are kept as loose as possible consistent with an acceptable dead time and manageable tape writing. This results in a tape writing rate of a few Hz compared to the 45 kHz of the beam crossing rate. In what follows, the term 'hadronic event' is to be understood to mean an event produced in the process:

$$e^+e^- \to \gamma/Z^0 \to q\bar{q}.$$

The trigger efficiency for hadronic events is greater than 99.9% [37].

In this chapter, first the selection of the hadronic event sample is described. However not all hadronic events are suitable for the analysis presented here. This necessitates a further selection which is motivated and presented. Furthermore it is important to understand the detector behaviour, especially the resolution and efficiency of detection. Also these topics are discussed in this chapter.

4.2 Selection of hadronic events

The hadronic decays of the Z boson at LEP have some very distinct properties. These properties can be used to identify and extract a sample of these events as explained below:

- The total visible energy of hadronic events is always around the center of mass energy of the e^+e^-collision. There are some losses because the neutrinos are invisible and because the resolution of the detector plays its part in smearing the energy around the true value. In contrast the beam-gas, beam-wall, synchrotron radiation, two photon events in the cases when one or both electrons remain inside the beam pipe, and the cosmic ray events rarely have a total energy close to the center of mass energy of the collision. The total energy can, therefore, be used to identify hadronic events and reject most of these background events.

- Since at LEP the laboratory frame and the center of mass frame are the same, the hadronic events are well balanced in energy flow and their energy imbalance should be small. Imbalance of energy along the beam direction (Z-axis) or in the plane perpendicular to it (X-Y plane) can be used to identify the hadronic events and reject the background processes which would not necessarily have balanced energy. For example, the beam-gas events would have high energy imbalance along the beam direction while beam-wall events would be imbalanced in the plane transverse to the beam direction as well as along the beam direction.

- The charged particle multiplicity of hadronic events can also be used as an indicator. The QCD prediction for average charged particle multiplicity is just over 20 charged particles around the Z resonance [38]. The average charged particle multiplicity in hadronic events at LEP is measured to be 20.79±0.03±0.52 [37]. For other types of events, the charged particle multiplicity is usually much lower. Thus by determining the charged particle multiplicity of the events, one can reject background such as the low multiplicity hadronic decays of the τ lepton.

During the off-line reconstruction of events, a preselection procedure is run with loose checks on the event characteristics described above. The following cuts are applied to obtain a relatively pure sample of hadronic events:

- $0.5 \leq E_{\mathrm{tot}} \leq 1.5$
- $0.5 \leq E_{\mathrm{had}} \leq 0.95$
- $E_{\mathrm{t}} \leq 0.6$
- $E_{\parallel} \leq 0.6$
- $N_{\mathrm{cluster}} \geq 10$,

where E_{tot} is the total energy observed in the calorimeters normalized to $\sqrt{s}$, E_{had} is the energy observed in the hadronic calorimeter normalized to E_{tot}, E_{t} is the transverse energy imbalance normalized to E_{tot} , $E_{\parallel}$ is the longitudinal energy imbalance normalized to E_{tot} and N_{cluster} is the number of energy clusters found in the calorimeters.

4.3 The need for a special selection

Detectable particles found in any event are hadrons, electrons, photons and muons. The behavior of these particles in the L3 detector is as follows: Neutral particles deposit their energy in the calorimeters leaving no signature in the tracking chamber. Photons normally deposit all their energy in the electromagnetic calorimeter. Charged particles, however, do leave a signature in TEC and deposit most of their energy in the calorimeters. The electrons deposit most of their energy in the electromagnetic calorimeter, while hadrons pass into the hadron calorimeter and usually are stopped there, depositing all of their energy. Besides the "invisible" neutrinos, the muons are the only particles that make it through to the muon chambers.

A charged particle can thus be identified in L3 as a track crossing the central tracking chamber, which also determines its direction. The energy deposits of all particles (charged and neutral) can be used as signatures of single particles and their direction can be determined by the position of the energy deposit. However since the granularity of the calorimeters is not fine enough and the width of the showers produced by the particles is not very narrow, two nearby particles can be seen as a single energy deposit. Thus one is confronted with a reduced efficiency for the detection of particles that are very close to each other in space. On the other hand, a single energetic particle can produce a shower not only along its initial direction of motion but can at times produce a shower at large angle to its initial direction of motion. Such a secondary shower may be considered a separate energy deposit by the reconstruction program. It is, therefore, not always possible to establish a one-to-one correspondence between an energy deposit and a particle entering the calorimeters. Since neutral particles can only be detected in the calorimeters, their detection efficiency and resolution is generally lower than that of charged particles which can be detected with a relatively high resolution and efficiency using the central tracking chamber.

Since the analysis of intermittency and correlations basically involves counting particles in events according to a given selection function, it is important not only to be able to determine their direction accurately but also to have a good two-particle resolution and to avoid double counting. As explained above, it is not always possible to have a good two-particle resolution if one uses the energy deposits to count them. Therefore, only the charged particles are used for the analyses presented in this thesis.

After the loose selection cuts described in the previous section, a further selection is performed as described below which uses only the tracking chamber. The calorimetric clusters are matched to the tracks in space in order to improve the resolution of the polar angle θ. This procedure is not necessary for the azimuthal angle ϕ, for which the TEC resolution is much better than that of the calorimetric clusters.

4.4 Track quality

The first step in the selection process is to define the criteria for well reconstructed tracks in the central tracking chamber TEC. There are a number of parameters on the basis of which one can decide if a track is good or not. A good track must have a high probability of coming from the interaction vertex and not being a misidentified track segment, a cosmic ray crossing the TEC or a stray beam particle. The quantities used to determine the goodness of a track are listed and described below. Figures show the cuts applied to reject badly reconstructed tracks. In all the figures, all other cuts described in this section have been previously applied.

Number of hits caused by a track

A track originating at the interaction vertex and passing through the TEC to the ECAL can cause a signal called a hit, on a maximum of 62 wires in TEC (8 in the inner TEC and 54 in the outer TEC). Misidentified track segments would usually have a smaller number of hits. Therefore a cut on the number of hits caused by a track helps in determining if the track is really coming from the vertex and is not a misidentified track segment. Figure 4.1(a) shows a distribution of the number of hits caused by Monte Carlo and data tracks. A cut at the slowly varying part of the curve is indicated by the arrow. The tracks are required to have at least 40 out of the 62 possible hits. The agreement between data and Monte Carlo is not very good as in data there are more tracks which have hits missing. Part of this discrepancy comes from the tracks in data which miss hits in the inner TEC as pointed out below.

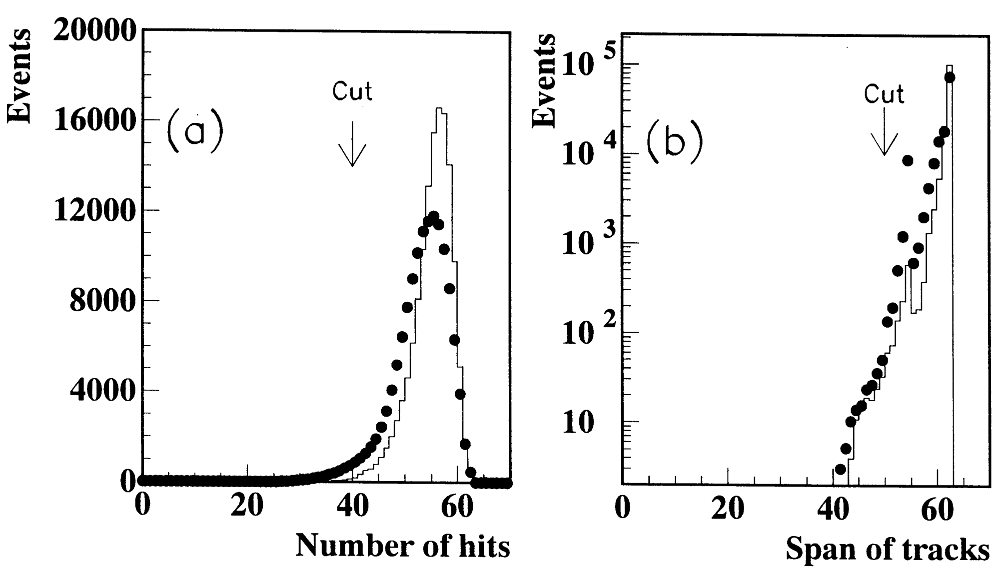

Figure 4.1: *(a) Number of hits caused by a track, (b) Span of tracks. Data are represented by dots and Monte Carlo by the histogram*

Span of the track

Tracks are reconstructed by a track-finding algorithm which combines hits to form tracks. Sometimes this algorithm reconstructs track segments from hits belonging to different tracks. These track segments usually have a length less than that expected for tracks originating at the vertex and crossing through the entire TEC. A measure of track length called Span is used to reject such track segments. A track is required to have a minimum length in terms of number of hits. The span of a track is defined as:

$$\text{Span} = \text{Wn}_{\text{Out}} - \text{Wn}_{\text{In}} + 1$$

Where Wn_{In} is the wire number of the innermost hit and Wn_{Out} is the wire number of the outermost hit recorded for a track. Figure 4.1(b) shows a comparison of the span of tracks coming from Monte Carlo events and those from real events. The cut is shown by the arrow in the figure. All tracks are required to have a span of at least 50. The small peak at around 54 comes from tracks for which the hits in the inner TEC were not used by the track fitting algorithm in reconstructing the track.

Outermost hit

If a track has a transverse momentum larger than 100 MeV/c, then it is expected to cross the TEC and enter the calorimeters. This can be checked by looking at the wire number of the last hit recorded for the track. A requirement on tracks to have at least one hit in the last 4 wires of a TEC sector ensures that the tracks leave TEC and enter the calorimeters. This cut helps to reject badly reconstructed track segments. Figure 4.2(a) shows this distribution for data and Monte Carlo tracks.

Distance of closest approach

To check if the tracks originate at the interaction vertex, each track is extrapolated back towards the interaction vertex. The distance of closest approach (DCA) is then calculated in the plane transverse to the beam direction. A requirement on the distance of closest approach to the interaction vertex ensures that the track originates at the vertex of interaction. Tracks are required to have a DCA less than 5 mm. Figure 4.2(b) shows this distribution for tracks from Monte Carlo and real events, with the cut values indicated on the figure by arrows.

Transverse momentum

The TEC measures the momentum of a track from its curvature in the plane transverse to the beam axis, which is the bending plane of the magnetic field. The momentum component of tracks in this plane is required to be greater than 100 MeV/c. Tracks with a transverse momentum less than 100 MeV/c curl up in the magnetic field and can not be measured accurately.

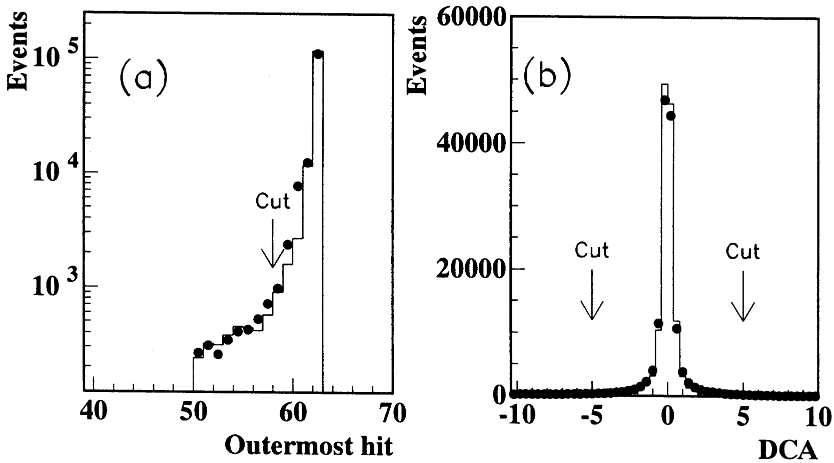

Figure 4.2: *(a) Outermost hits recorded by a track, (b) Distance of closest approach in the plane transverse to beam direction. Data are represented by dots and Monte Carlo by the histogram.*

4.5 Special hadronic event selection

The sample of hadronic events selected by the procedure described in section 4.2 still contains some background events and events in which track quality is not good. For the analysis presented here, however, one needs to select events with good tracks as described in section 4.4. For this reason, the sample of events is passed through a selection procedure which uses only good tracks. This results in a sample of hadronic events with good quality tracks. The cuts applied in this procedure are described below.

Average charged particle multiplicity (N_{ch}) cut

The measured average charged particle multiplicity in hadronic events at LEP on the Z resonance is 20.79±0.03±0.52 [37]. Figure 4.3(a) shows a plot of the charged particle multiplicity distribution for data and for Monte Carlo (JETSET 7.3). The hatched histogram in the figure is the result of Monte Carlo simulation of τ events. The τ Monte Carlo events are known to reproduce the data [39]. The low multiplicity tail of the data distribution comes from:

$$e^-e^+ \rightarrow e^+e^-(\gamma)$$

$$e^-e^+ \rightarrow \tau^+\tau^-(\gamma)$$
$$e^-e^+ \rightarrow \mu^+\mu^-(\gamma)$$

and two-photon processes. Also some beam-gas events that remain after the preselection are of low multiplicity. The requirement $N_{ch} \geq 5$ removes most of the $\tau^+\tau^-$, e^-e^+ and $\mu^+\mu^-$ events, as well as the events from two-photon processes, beam-gas interactions and beam-wall interactions.

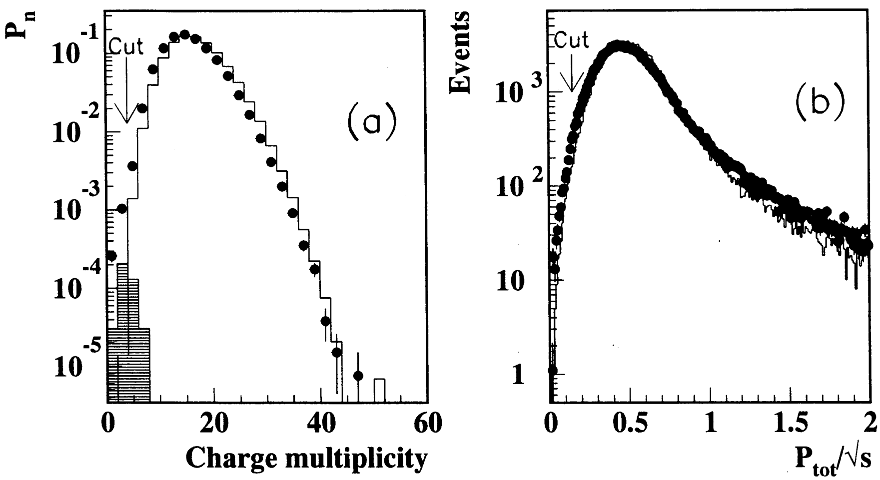

Figure 4.3: *(a) Charged particle multiplicity, (b) Total momentum normalized to $\sqrt{s}$. Data is represented by dots and Monte Carlo by the histogram. The hatched histogram is the τ hadronic decays predicted by Monte Carlo.*

Total momentum (P_{tot}) cut

This cut rejects the background arising from the beam-gas and beam-wall interactions events or two-photon processes in which one or both electrons remain within the beam pipe. Figure 4.3(b) shows the distribution of the total momentum sum of the tracks as seen in the TEC, P_{tot} normalized to the total beam energy for real data events and its comparison with Monte Carlo. To eliminate noise events, a cut is applied on the lower tail of this distribution as indicated by an arrow on the figure. P_{tot} is required to be more than 0.15.

Parallel momentum sum ($P_{||}$) cut

The sum of momentum components of tracks along the beam axis, normalized to the total visible momentum, called $P_{||}$ in an event should ideally be zero for hadronic decays of the Z boson. This is because at LEP the laboratory frame is also the center of mass frame. Two-photon, beam-gas and beam-wall interactions give rise to events in which the momentum is not necessarily balanced along the beam direction. To reject such events, $P_{||}$ is required to be less than 0.75. Figure 4.4(a) shows this distribution of $P_{||}$ for both data and Monte Carlo.

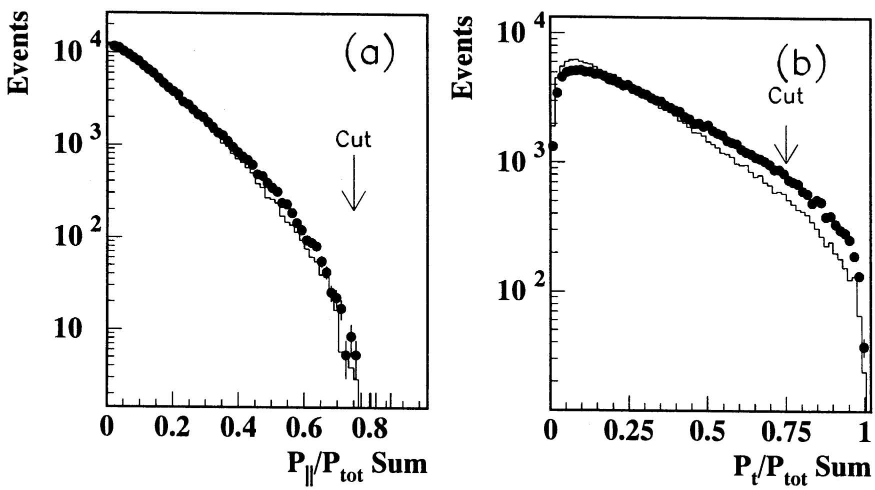

Figure 4.4: *(a) Imbalance along the beam axis, (b) Imbalance in the plane transverse to the beam axis. Both imbalances are normalized to total momentum. Data are represented by dots and Monte Carlo by the histogram.*

Transverse momentum sum (P_t) cut

The vector sum of momenta of tracks in the plane perpendicular to the beam, normalized to the total visible momentum, called P_t should be zero. Large values of P_t can arise from poor track measurements or presence of high momentum neutrinos. Figure 4.4(b) shows this distribution for data and for Monte Carlo. P_t is required to be less than 0.75; the cut is shown in the figure by an arrow.

The ϕ_2 cut

The $\tau^+\tau^-$ events in which both τ particles decay into charged particles are a background to the hadronic events. By imposing a cut on the second largest angle ϕ_2 between any two neighboring tracks in the R-ϕ plane to be less than 170°, this contamination can be removed. Figure 4.5 shows the distribution of the angle ϕ_2 for data and hadronic Monte Carlo events. The background expected from τ Monte Carlo events is shown by the hatched histogram in the figure; it lies predominantly above 170°. The τ Monte Carlo events are known to reproduce the data distributions [39].

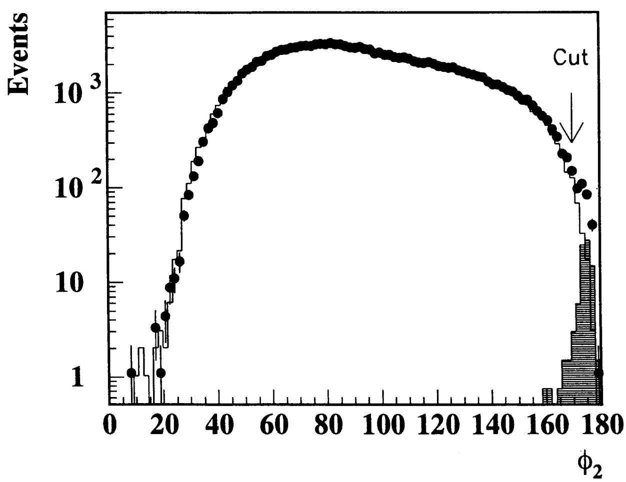

Figure 4.5: *Second largest angle between two neighboring tracks. Data are represented by dots and Monte Carlo by the histogram, the hatched histogram is the Monte Carlo τ hadronic decays predicted by Monte Carlo.*

Theta of thrust axis θ_{thrust} cut

Events are required to be contained in TEC as much as possible. This is achieved by requiring the polar angle of the thrust axis of the event θ_{thrust} to be in the polar angle range covered by TEC, i.e., $45° < \theta < 135°$.

All of the above mentioned cuts on the events are applied in a logical AND. After selection the final sample consists of approximately 150 thousand events on the peak of the Z resonance. The selection efficiency of this selection procedure is estimated from a Monte Carlo study to be 66% .

4.6 Simulating TEC inefficiency

As described in chapter 2, TEC is a complex multiwire chamber and requires constant monitoring. In case of problems, the whole TEC or parts of it can be turned off. Situations have been encountered during data taking when TEC indeed had to be partially or totally switched off. For the reconstruction of the Monte Carlo events, however, it is assumed that the TEC is switched on all the time and is 100% efficient. Thus, the Monte Carlo events do not simulate data according to the data acquisition conditions. In order to reproduce the conditions at the time of data acquisition, a so-called '4 Minute' interval test is performed for the Monte Carlo events [40].

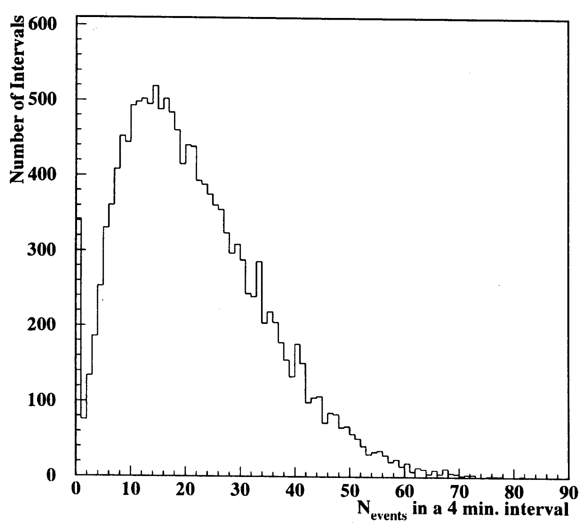

Figure 4.6: *Distributions of the number of events found in a 4 minute interval of data taking.*

The idea behind the 4 minute interval test is to switch off TEC sectors in the Monte Carlo events that were not functioning during the actual data taking. The way this is done is that the Monte Carlo events are assigned run numbers and acquisition times which correspond to the real events. The real hadronic events in the 4 minute time window for which the analysis is being performed are analyzed and searched for tracks in different TEC sectors. As explained above, the mean charged particle multiplicity in hadronic events is about 20 tracks. Further, one expects an average of 21 events within the 4 minute time window, given the LEP luminosity and the cross section of the hadronic events. Figure 4.6 shows the distribution of the number of hadronic events found during a 4 minute running-time interval for data. Assuming that the approximately 400 tracks expected in a 4 minute time window are distributed uniformly over over all 24 sectors, there is a high probability of finding at least one track in a sector. If a track is found in a sector, then that sector is declared to be alive during the 4 minute time interval and any tracks in the corresponding Monte Carlo events that fall into that sector are considered for analysis. If no tracks are found in a 4 minute interval in a sector, then this sector is declared dead during the 4 minute time interval and any tracks from the corresponding Monte Carlo event sample that fall into that sector are not considered for analysis. One thus obtains a detector simulation of the Monte Carlo events which takes into account the run-time conditions of TEC.

While in the above described procedure one assumes that a TEC sector is on and 100% efficient even if only one track is found in the sector during a 4 minute interval, individual sectors have some intrinsic inefficiency, as well. To correct for this inefficiency, distributions of data in azimuthal angle ϕ are used to find the relative inefficiency of a particular sector. These inefficiencies are then used to randomly throw out Monte Carlo tracks in the inefficient sectors. The resulting Monte Carlo distribution in ϕ is compared with data in figure 4.7. A good agreement between data and Monte Carlo is seen after the correction.

The polar angle θ of a track is determined using the charge division information from the TEC and the clusters in the BGO calorimeter to which the track points. Some times neither information is available and the track is put at $\theta = 90°$. The probability for this to happen is larger in data than in Monte Carlo giving a bad agreement between data and Monte Carlo for polar angle θ. It has been found that this occurs randomly in data and therefore, to correct for this effect, tracks are randomly put at $\theta = 90°$ in Monte Carlo to get a good agreement between data and Monte Carlo.

4.7 Resolution

As mentioned above, a good angular resolution for the tracks is imperative for the study of particle correlations. The authors of [23] have pointed out how one can reach wrong conclusions while studying particle correlations, if two particle resolutions are not well understood.

Numbers are quoted in chapter 2 for the resolution as obtained in TEC. These numbers give the resolution for a single track, whereas in the study of correlations the knowledge of double track resolution is necessary to choose suitable bin sizes for the distributions of various correlation functions. In the following, the double track resolution for the quantities used in the analysis are discussed. The major quantities used in the analysis

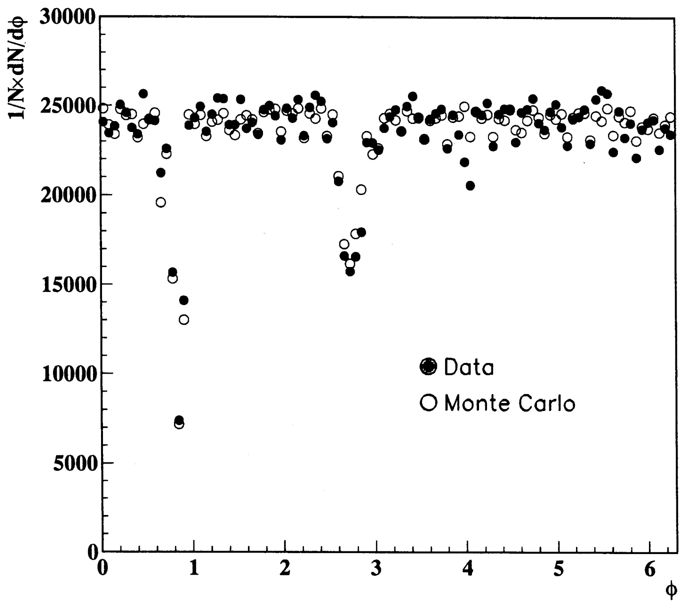

Figure 4.7: *Distribution of azimuthal angle ϕ for data and Monte Carlo events after the Monte Carlo events were corrected for TEC ineffiencies*

are:

- The azimuthal angle ϕ_{12} between two tracks about the beam axis.
- The polar angle θ_{12} between two tracks, or equivalently, pseudorapidity separation η_{12} between two tracks calculated with respect to the beam axis.
- The angular separation between two tracks in space ψ_{12}.
- The squared four momentum difference between two tracks Q^2_{12} .
- The transverse momentum P_t of tracks .

4.7.1 Determination of resolution

Suppose the true value of the quantity that one wants to measure is X. But what one actually measures with any real detector is not the true quantity X but X′, the true quantity smeared with the detector resolution and acceptance.

The L3 detector simulation program SIL3, simulates the detector response to Monte Carlo events. SIL3 includes a detailed description of the detector geometry including permanent imperfections, such as the hole between the ECAL endcaps and the barrel.

Taking the true value of the quantity of interest X to be the value at the Monte Carlo generator level, SIL3 is used to simulate the response of the detector to X and produce X′ with the effects of limited resolution and acceptance. By histogramming

$$\delta = \mathrm{X} - \mathrm{X}'$$

with sufficiently large statistics, one can estimate the resolution function for a particular quantity taking into account the detector acceptance.

In Monte Carlo simulation one tries to imitate the data as much as possible by simulating the response of the detector to the particles as they pass through it. Since this is only an approximation of the real phenomena, one must make sure that the Monte Carlo simulation does indeed reproduce the data before one can trust the Monte Carlo in trying to find the resolutions. This can be done by comparing the distributions of the data and Monte Carlo for some variables. It has been shown [37] that the JETSET 7.3 Monte Carlo event generator together with the Monte Carlo detector simulation program SIL3 reproduces the general event shape variables very well.

For the correlation studies presented in this thesis it is also necessary to show that variables involving pairs of tracks are also well reproduced by Monte Carlo events. Figure 4.8 shows the distributions in θ_{12} and ϕ_{12}, the separation in polar and azimuthal angles between any two tracks, in the detector frame of reference for data and for Monte Carlo. As can be seen, Monte Carlo simulation of the generated events does indeed reproduce the distributions of data. One can conclude from these distributions and the event shape variable distributions in [37] that the gross features of detector effects are present in the SIL3 Monte Carlo simulation and can thus be used to determine the resolutions for different quantities.

4.7.2 The resolution and efficiency

The resolutions for particle pairs have been obtained from a Monte Carlo study of about 2500 Monte Carlo hadronic events. For every track pair in an event the quantities ψ_{12}, ϕ_{12}, Q^2_{12}, η_{12}, θ_{12} and p_t are calculated, first using generator level information and then using the information after detector simulation. The difference is the effect of detector resolution. These differences (Generator level - Detector level) are histogrammed in figure 4.9 for the above mentioned variables. All distributions are peaked at zero as one would expect, but all of them have large tails. The existence of these tails inhibits one from quoting a single number for the resolution. The tails on these distributions cause a pair of particles with bad resolution to add to the non-correlated background both in data and Monte Carlo. The experimental results given here will therefore be a lower limit for the actual correlation, but the Monte Carlo comparison remains meaningful.

The primary use of the resolutions in this study is to determine the smallest meaningful bin size for the correlation studies. The half width at half maximum (HWHM) of

Quantity	HWHM
ψ_{12}	1.39×10^{-2} radians
ϕ_{12}	3.10×10^{-3} radians
Q^2_{12}	1.60×10^{-2} $[GeV/c]^2$
θ_{12}	2.40×10^{-2} radians
η_{12}	2.79×10^{-2}
p_{t12}	4.00×10^{-2} GeV/c

Table 4.1: *Resolutions*

the resolution distribution suffices for this purpose. The values of HWHM for different variables are listed in table 4.1

The efficiency of detection was also calculated using the Monte Carlo events and was found to be 94% for the track pairs which lie in the angular region $45°<\theta<135°$ and have a transverse momentum greater than 0.1 GeV/c. For single tracks this number is 96%.

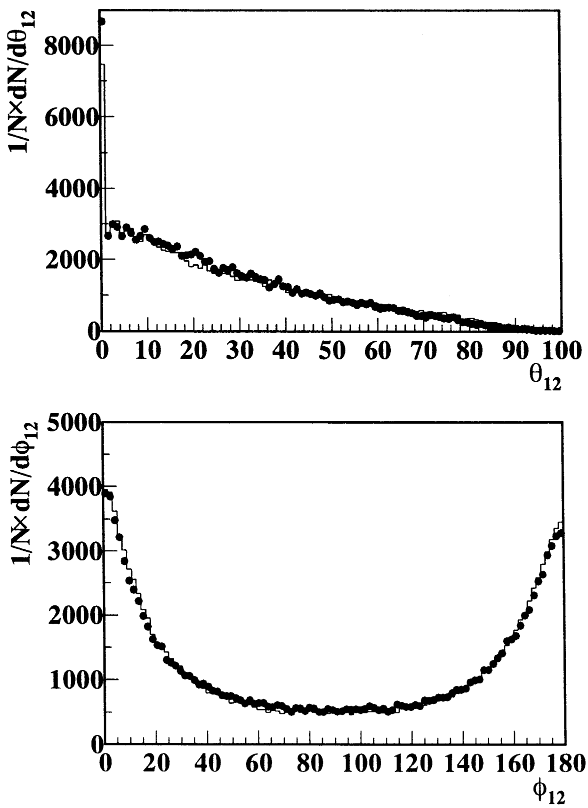

Figure 4.8: *Distributions of θ_{12} and ϕ_{12} the polar and azimuthal angle separation between two tracks in the detector frame. Data are represented by dots and Monte Carlo by the histogram*

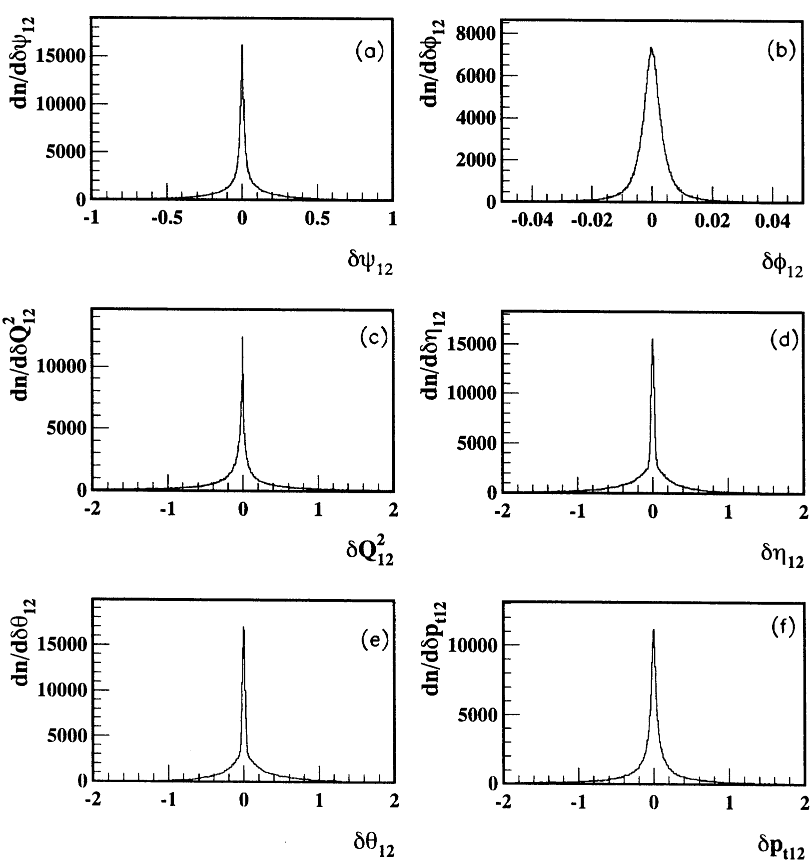

Figure 4.9: *Double track resolution distributions for various variables (see text)*

Chapter 5

Intermittency

5.1 Introduction

The phenomenon of intermittency has already been introduced in Chapter 1. Here, we present the analysis of the L3 data in terms of two different variables. The data are compared to the predictions of a number of models commonly used in e^+e^- collisions at LEP and simulated by means of the Monte Carlo method. First we present different analytical tools used in the analysis, then the results of the analysis are presented and discussed.

5.2 Tools for density fluctuation analysis

To study dynamical density fluctuations in multiparticle production, analytical methods have been devised which can extract the information on non-statistical fluctuations in particle density from an event or a sample of events [20, 21]. In this section we briefly describe these tools.

5.2.1 Factorial moments

Following the observation of a high multiplicity event by JACEE [19] in which peaks were found in the pseudo-rapidity distribution, it was proposed [20] to study scaled factorial moments in order to pick out dynamical density fluctuations from a background of purely statistical fluctuations. Later, the authors extended this formalism so that it is possible to study more than one event and also events with lower multiplicity, such as the events encountered in present day collider experiments [21].

There are two distinct types of factorial moments, *vertically normalized* and *horizontally normalized* factorial moments, both proposed by the authors of [21]. The horizontally normalized factorial moments are defined as:

$$F_q^{\rm h}(\delta y) = \frac{M^{q-1}}{< N >^q} \left\langle \sum_{m=1}^{M} n_m(n_m-1)...(n_m-q+1) \right\rangle ,$$

where q stands for the order of the moment. To calculate these moments, one considers an initial phase space interval Δy and divides it into M bins, each of bin size $\delta y = \Delta y/M$. Then, for each event, one counts the number of particles per bin $(n_m, m = 1, ..., M)$ and the total number of particles $N = \sum_{m=1}^{M} n_m$. The symbol $\langle ... \rangle$ represents the average over all events. Note that in the above expression, y can be any phase-space variable such as rapidity y, azimuthal angle ϕ, p_t, or a combination of these variables. The initial phase-space interval should be chosen large enough to allow many subdivisions, but should be small enough to avoid energy-momentum constraints for the total collision [41].

The vertically normalized moments are defined as

$$F_q^{v}(\delta y) = \frac{1}{M} \sum_{m=1}^{M} \frac{\langle n_m(n_m-1)...(n_m-q+1)\rangle}{\langle n_m \rangle^q},$$

where $\langle n_m \rangle$ is the average number of particles in the bin m in the event sample.

The vertically normalized factorial moments are more sensitive to bin by bin variations within events, but they become unstable at small bin sizes, whereas the horizontally normalized factorial moments remain stable over a larger range [41]. It should be pointed out here that both types of factorial moments are the same when $\langle n_m \rangle = \langle N \rangle / M$ for all m, i.e. the under lying distribution in the particular phase space variable is flat.

Properties of factorial moments

A number of important properties of the scaled factorial moments are listed below:

- The factorial moments act as filters, allowing only contributions from bins with $n_m \geq q$.
- If there are self-similar non-statistical density fluctuations in the event sample considered, the scaled factorial moments rise with decreasing δy according to a power law:

  $$F_q \propto \delta y^{-f_q}, \qquad f_q > 0,$$

  If, however, the fluctuations in the event sample are merely statistical, then the scaled factorial moments are independent of the bin size.
- The scaled factorial moments rise steadily with decreasing bin size, so long as the region of phase space probed (i.e bin size) is larger than the correlation length and remain constant for smaller bin sizes [42]. A similar behaviour is exhibited around the bin size equal to the experimental resolution and for Monte Carlo events when detector resolution has been included in the simulation.

The slopes of power law fits on a double-logarithmic plot, given by the intermittency indices f_q in the above expression, are used to quantify the intermittency observed in an experiment. A word of caution is in place here: the authors of [43] and [44] have pointed out that the signal of intermittency, even if present in higher dimensions, can be lost if one considers one-dimensional factorial moments. This is due to the projection of a three dimensional density distribution in momentum space onto a single axis. The one-dimensional factorial moments, therefore, can give evidence that intermittency exists, but cannot definitely exclude the presence of intermittency. To overcome this problem, it is necessary to study the factorial moments in more than one dimension, or atleast find the most sensitive distance measure.

5.2.2 Density strip integrals

Recently, a new development in the tools for the study of density fluctuations has been proposed [45] as a natural extension of the factorial moments. The vertically normalized factorial moments can be written in terms of density integrals as follows [45]:

$$F_q^{\mathrm{v}}(\delta y) \equiv \frac{1}{M}\sum_{m=1}^{M}\frac{\langle n_m(n_m-1)...(n_m-q+1)\rangle}{\langle n_m\rangle^q} = \frac{1}{M}\sum_{m=1}^{M}\frac{\int_{\Omega_m}\prod_i \mathrm{d}y_i\rho_q(y_1,...,y_q)}{\int_{\Omega_m}\prod_i \mathrm{d}y_i\rho_1(y_1),...,\rho_1(y_q)},$$

Where $\rho_q(y_1,...,y_q)$ is the q-particle density function and $\rho_1(y_1)...\rho_1(y_q)$ is the product

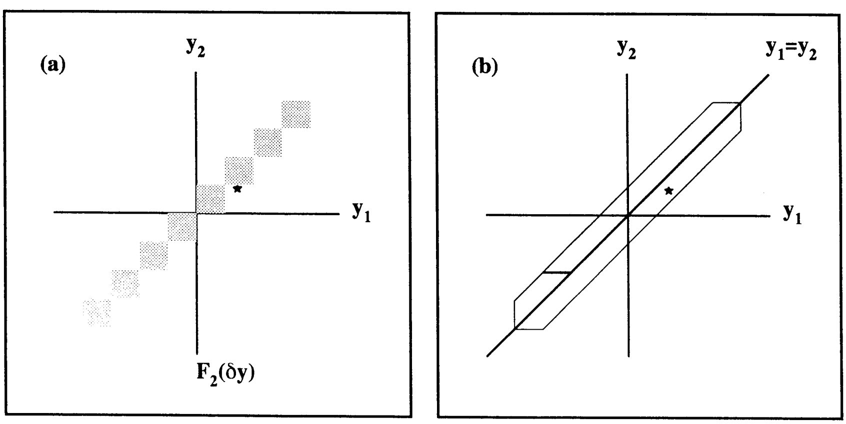

Figure 5.1: *a) The integration domain $\Omega_B = \sum_{m=1}^{M}\Omega_m$ of $\rho(y_1,y_2)$ for the bin averaged factorial moments, b) the corresponding integration domain Ω_s for the strip integration.*

of single particle density functions. The integration domain $\Omega_B = \sum_{m=1}^{M}\Omega_m$ thus corresponds to M q-dimensional hyper-boxes with an edge of length δy. If we consider the case $q=2$, the integration domain Ω_B is the one shown in figure 5.1(a). A point in any box corresponds to a pair of particles (y_1,y_2) lying in the same bin and being separated from each other by a distance $\mid y_1 - y_2 \mid$ less than the length of the diagonal of the box. On the other hand, there are many pairs with distance even less than δy, not lying in the same but in adjacent bins (one such point is shown as a star in the figure 5.1(a)). These pairs, therefore, do not contribute to factorial moments. Such a treatment results not only in a loss of statistics, but also in the splitting of spikes in the phase space distribution, such as the ones observed by JACEE [19] and NA22 [46], if the spike happens to lie near the box or bin boundary.

The authors of [45], therefore, suggest an improvement of the integration domain by changing it from the box domain shown in figure 5.1(a) to a strip domain as shown in figure 5.1(b). For the second order moments in a one-dimensional analysis, this improvement results in approximately doubling the statistics. For higher orders q, the improvement is roughly proportional to the order of the correlation considered. The gain factor for statistics is even larger when working with 2 or more dimensional phase space.

The vertical density integrals for a strip (or hyper-tube in case of $q > 2$) integration domain are then given by:

$$F_q^{\mathrm{vs}}(\delta y) \equiv \frac{\int_{\Omega_s} \prod_i \mathrm{d}y_i \rho_q(y_1, ..., y_q)}{\int_{\Omega_s} \prod_i \mathrm{d}y_i \rho_1(y_1), ..., \rho_1(y_q)},$$

where the superscript s stands for strip and the integration domain Ω_s corresponds to the strip domain shown in figure 5.1(b) for the case of $q = 2$.

The horizontally normalized factorial moments can be written in terms of particle density functions as:

$$F_q^{\mathrm{h}}(\delta y) = \frac{1}{M} \sum_{m=1}^{M} \frac{\int_{\Omega_m} \prod_i \mathrm{d}y_i \rho_q(y_1, ..., y_q)}{\int_{\Omega_B} \prod_i \mathrm{d}y_i \rho_1(y_1), ..., \rho_1(y_q)},$$

where $\Omega_B = \sum_{m=1}^{M} \Omega_m$. The strip-integration equivalent of the horizontally normalized factorial moments is then

$$F_q^{\mathrm{hs}}(\delta y) \equiv \frac{\int_{\Omega_s} \prod_i \mathrm{d}y_i \rho_q(y_1, ..., y_q)}{\langle n \rangle^q \cdot S^{\mathrm{vol}} / \Delta^q},$$

where Δ is the full volume of the phase space and S^{vol} is the volume of the strip. In the case of one dimension, for example y the rapidity, Δy is the full range of rapidity y considered. To calculate the density strip integrals for data, one has to compute the numerator and the denominator of the above expression, separately. The numerator can be calculated by simply counting the number of q-tuples that have a distance smaller than δy. Mathematically, this procedure can be expressed as:

$$\int_{\Omega_s} \prod_i \mathrm{d}y_i \rho_q(y_1, ..., y_q) = \left\langle q! \sum_{i_1 < ... < i_q} \Theta(\delta y - D^q(y_{i_1}^{ev}, ...y_{i_q}^{ev})) \right\rangle .$$

where $D^q(y_{i_1}^{ev}, ...y_{i_q}^{ev})$ gives the largest value of the absolute inter-particle distance between q particles and Θ is the Heaviside unit step function. The calculation of the denominator is different for *vertically* and *horizontally* normalized cases. The *vertical* normalization is performed by using uncorrelated events. The way this is done, is that the tracks from real events are used to create a pool of tracks. Each normalization event is assigned a multiplicity N according to a poissonian distribution with an average multiplicity N_{Norm}. Then N particles are randomly extracted with equal probability from the track pool, imposing the constraint that all particles should originate from different events. Since these tracks are uncorrelated, $\rho_q(y_1, ..., y_q)$ factorises to $\rho_1(y_1), ..., \rho_1(y_q)$. To get the denominator, the same counting procedure is used as for the real events. Finally a correction factor is applied to correct for the difference in average multiplicity of the poissonian and the experimental distribution. For horizontal normalization, in many cases analytical expressions for the strip volume S^{vol} exist and, therefore, the horizontal normalization factors can be calculated analytically.

Advantages of density strip integrals

The density strip integrals have a number of advantages over the usual factorial moments [45]:

- Strip Intergrals have a larger integration domain. Therefore, the statistical error on their measurement is significantly less.
- Strip Integrals do not require artificial binning of an event and thus avoid artificial fluctuations in the δy dependence of $F_q(\delta y)$ due to splitting fluctuations (spikes) near the bin boundaries.
- It is possible to study correlations in a variety of new variables, not possible with the usual factorial moments. An example is that of $Q^2_{ij} = -(p_i - p_j)^2$, the squared four-momentum difference between two particles, which is a theoretically preferred variable in jet evolution studies and particle decays.

5.3 Factorial moment analysis

In this section, an analysis of factorial moments performed on the L3 data collected during the 1991 running period is presented.

The main purpose of this piece of analysis is to see whether an intermittency effect can be seen in the data and to compare to the Monte Carlo models commonly used for e^+e^- collisions at LEP.

As is shown in section 4.7.2, the resolution for quantities involving the polar angle θ is not very good in L3. The resolution is not only poor, but it also varies over a wide range. However, for the case of the azimuthal angle ϕ in the plane perpendicular to the beam axis, the resolution is particularly good and stable. One can resolve track pairs down to 4 mrad separation with a high confidence. Keeping in mind the remarks made in [23] on the pitfalls that one encounters when calculating the factorial moments due to limited two particle resolution, the azimuthal angle ϕ has been chosen as a variable to study the factorial moments in one dimension. The horizontal normalization has been applied to the factorial moments. This is deemed legitimate because the distribution of tracks in azimuthal angle ϕ is flat and as explained in section 5.2.1, vertical and horizontal normalisations are expected to give the same result.

In order to be able to compare the predictions of the various Monte Carlo models with the experimental data, we have corrected the data for detector response. We calculate correction factors for the data using samples of JETSET 7.3 parton shower (JETSET 7.3 PS) and HERWIG 5.4 events run through the detector response simulation program SIL3 and reconstructed by the REL3 program. The distributions of event shape variables are well reproduced by both of these Monte Carlo models [37] and uncorrected factorial moments reproduced by JETSET 7.3 PS Monte Carlo after detector simulation and reconstruction, as shown in figure 5.2. The downward bending of the higher order moments at large -lnδy is due to a combination of detector effects and the so-called "empty-bin effect" [42].

The correction factors are calculated as follows: Let N_i^P be the number of entries in bin-i of the input distribution at the generator level, and N_i^D be the number of entries in bin-i of the distribution at the detector level (i.e. after detector simulation and event selection). Then, the correction factors $C_i^{\rm det}$ are

$$C_i^{\rm det} = \frac{N_i^{\rm P}}{N_i^{\rm D}}.$$

The correction factors for initial and final state radiation effects $C_i^{\rm rad}$ are calculated with the same logics as applied for detector effects and are defined as:

$$C_i^{\rm rad} = \frac{N_i^{\rm off}}{N_i^{\rm on}}$$

where $N_i^{\rm off}$ and $N_i^{\rm on}$ stand for entries in ith bin with initial and final radiation off and on respectively. Multiplying the $C_i^{\rm det}$ and $C_i^{\rm rad}$ by the measured factorial moments in bin bin-i (D_i), we get the corrected result in bin-i (U_i):

$$U_i = C_i^{\rm rad}.C_i^{\rm det}.D_i.$$

The distributions U_i can then be compared directly with the Monte Carlo model predictions at the generator level.

For this study, we have used correction factors calculated from approximately 200k JETSET 7.3 PS fully simulated and reconstructed events. The corrections from HERWIG 5.4 give results similar to those from JETSET 7.3 PS.

The systematic errors are calculated by varying the track selection cuts about their mean values and by varying the efficiency of the TEC sectors. The error bars in the figures include the contributions from both statistical and systematic sources added in quadrature.

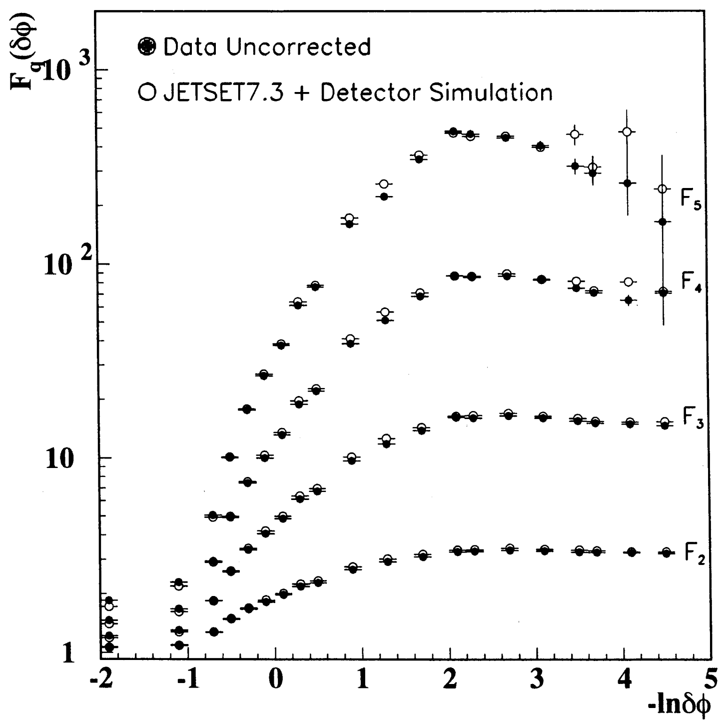

Figure 5.2: *Factorial moments in azimuthal angle ϕ of order q=2-5 for uncorrected data and for the JETSET 7.3 parton shower Monte Carlo model after simulation of detector response by the SIL3 program and reconstruction by the REL3 program.*

5.3.1 Comparison with models

Figure 5.3 shows a comparison of our corrected data with JETSET 7.3 (PS), JETSET 7.3 (ME), COJETS 6.22 and HERWIG 5.4, for scaled factorial moments ranging in order from 2 to 5. All of these models have been tuned for L3 data [37]. Whereas all models give a fairly good description of the data, the best description is provided by JETSET 7.3 PS. The factorial moments of all orders show a rise for large bin sizes, but tend to flatten out for small bin sizes. The resolution for azimuthal angle ϕ as discussed in section 4.7.2 is better than 4 mrad. The resolution, therefore, cannot be responsible for the flattening since the smallest bin size used in this figure is 10 mrad. Since we are using a one-dimensional projection of angular variables, the observed flattening can have two possible causes. The first possible cause can be the projection effects, while a second cause can be the findings in [18] that the small angular bins would show a saturation effect due to running of the coupling constant α_s. Since we are using one-dimensional factorial moments in this section, it is not possible to exclude the existence of intermittency in our data, but the conclusion that can be drawn from this exercise is that the Monte Carlo models reproduce the data in the azimuthal angle ϕ.

5.3.2 Effect of multiplicity

While a definite decrease of the intermittency indices with increasing multiplicity has been reported for the high energy hadronic collisions [47], studies based on rapidity have, so far, not revealed such an effect for LEP. We again use the horizontal normalization and the azimuthal angle ϕ as the phase space variable. The data are divided into two event samples, one containing events with multiplicity larger than 15 charged particles and the other events with multiplicity smaller than 15 charged particles.

Factorial moments are calculated for both of these samples and are compared with those of the full data sample. The comparison is shown in figures 5.4 and 5.5. The full symbols correspond to the data, the open ones to JETSET 7.3 PS after detector simulation and reconstruction.

A first observation on these figures is that the model can describe the data. A second observation is that the slopes at larger $\delta\phi$ (small $-\ln\delta\phi$) differ for the three samples. They are smaller for the $N_{ch} > 15$ sample than for the full sample, but bigger for the $N_{ch} < 15$ sample.

5.4 Density strip integral analysis

In this section, we present the analysis performed on data and Monte Carlo using the 'density strip integrals' described in section 5.2.2. We have used two variables for the study of strip integrals, the azimuthal angle ϕ measured in the plane transverse to the beam axis and the squared 4-momentum difference Q^2 between any pair of tracks in an event. In the results shown in this section, the data distributions have been corrected for

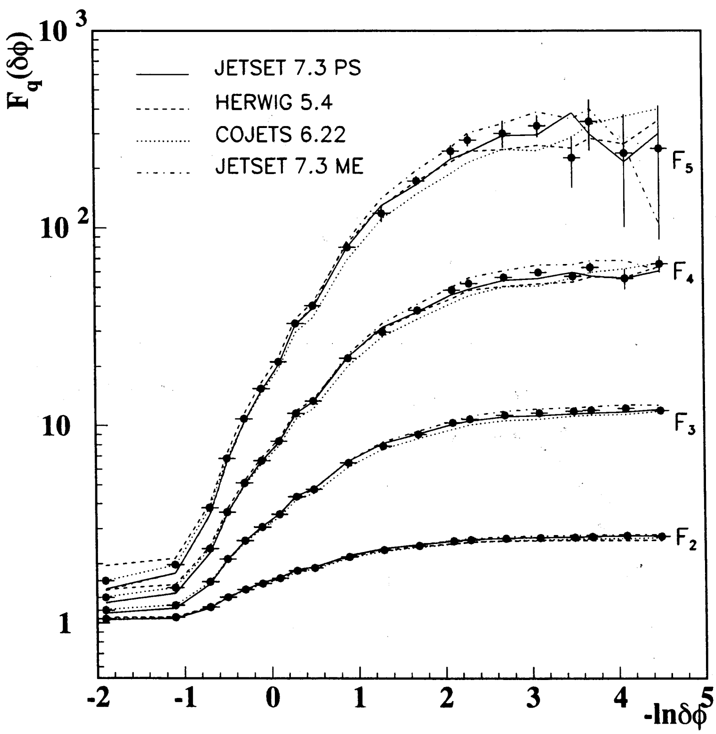

Figure 5.3: *Factorial moments in azimuthal angle ϕ for corrected data compared to the predictions from Monte Carlo models tuned to L3 data by means of event shape variables.*

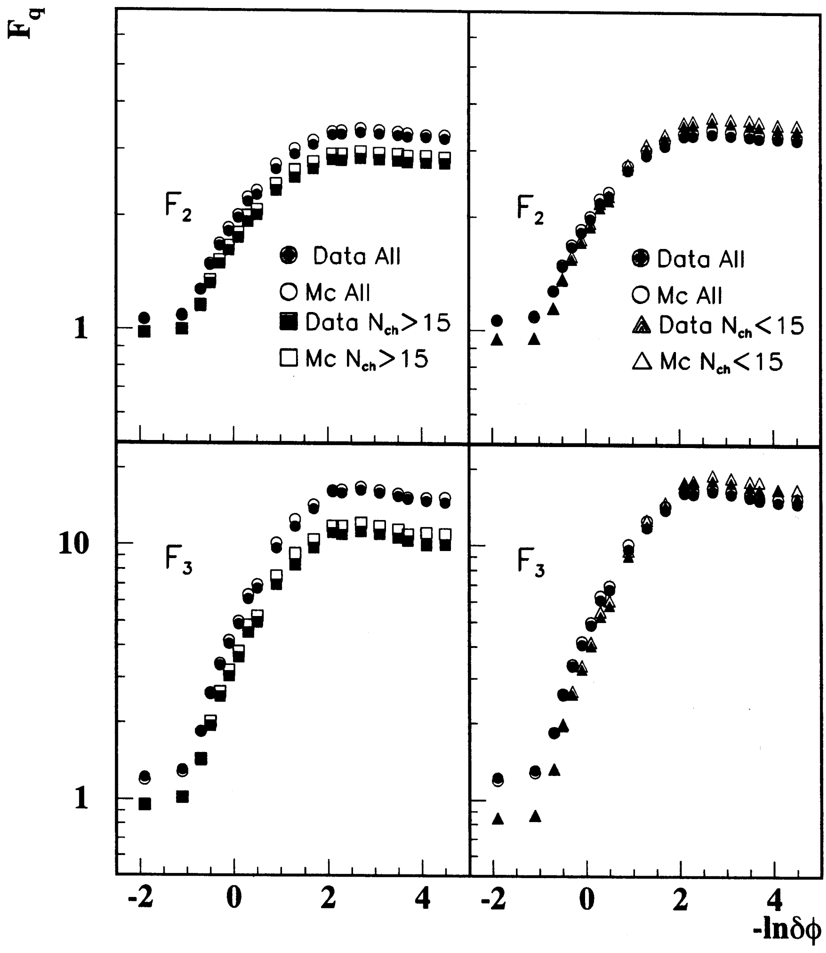

Figure 5.4: *Uncorrected factorial moments for azimuthal angle ϕ with multiplicity cuts for orders 2 and 3 compared to the JETSET 7.3 parton shower Monte Carlo events after detector simulation and reconstruction.*

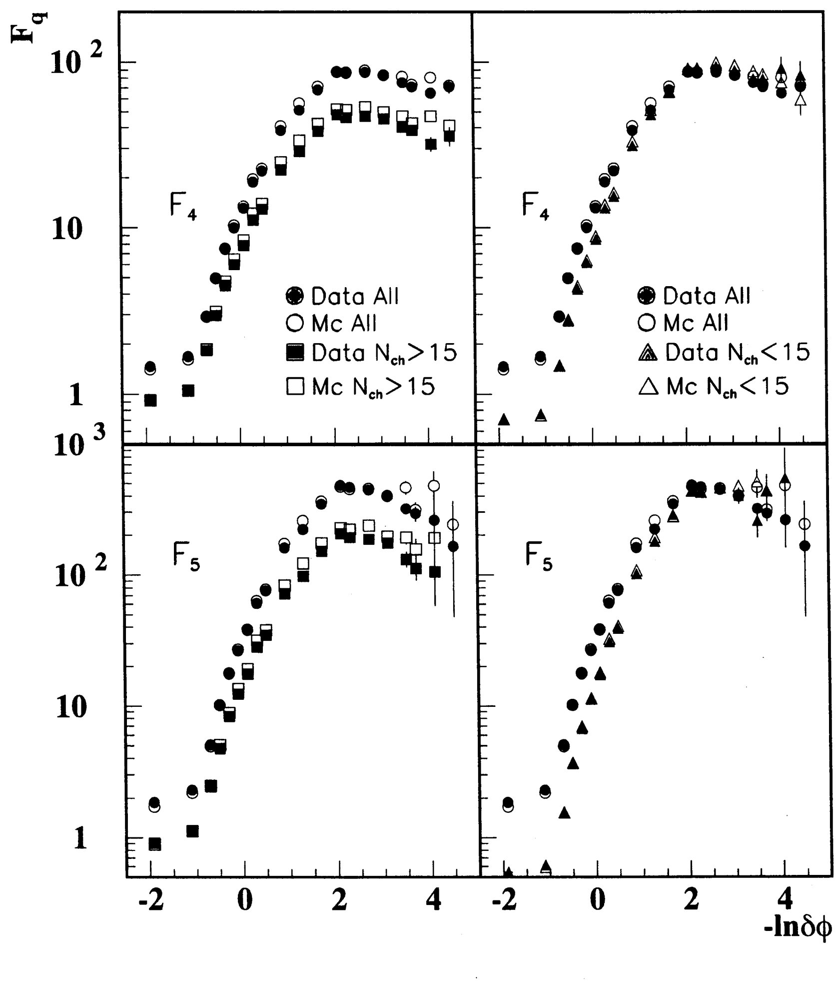

Figure 5.5: *Uncorrected factorial moments for azimuthal angle ϕ with multiplicity cuts for orders 4 and 5 compared to the JETSET 7.3 parton shower Monte Carlo events after detector simulation and reconstruction.*

detector effects by the procedure described in section 5.3. Monte Carlo here should be taken to mean JETSET 7.3 PS tuned to the L3 data on event shape variables.

5.4.1 Density strip integrals in ϕ

As discussed in section 4.7.2, the experimental resolution for the azimuthal angle is better than 4 mrad. We are, therefore, justified in using a bin size as small as $\delta\phi$=10 mrad for this study. In the evaluation of F_q^{vs}, vertical normalization and event mixing are used.

Figure 5.6 shows F_q^{vs} for corrected data and JETSET 7.3 Monte Carlo tuned to L3 data [37]. The Monte Carlo predictions reproduce the data very well. Once again, as was the case for the factorial moments presented in section 5.3, the distributions show a flattening behaviour at small $\delta\phi$ (large -ln$\delta\phi$). As we shall see in section 5.4.2, this is not the case for our data when one considers Q^2 as the phase space variable. This flattening is thus consistent with the findings of [18]. Another effect to notice is the peak between –ln $\delta\phi$=–2 and –ln $\delta\phi$=–1. This has been found to be a result of energy-momentum conservation and emphasizes the point made in [41], that the phase space bin considered for an analysis of intermittency should not be so large as to include the trivial effects of energy-momentum conservation.

5.4.2 Density strip integrals in Q^2

Here, we present the results of the analysis using the variable $Q^2 = -(p_1 - p_2)^2$, the squared four-momentum difference between two tracks. This is a theoretically preferred variable in jet evolution studies and particle decays and also has the advantage of showing the effects of a three dimensional analysis [42]. The resolution of the L3 detector in Q^2 is discussed in section 4.7.2. Based on those findings, the smallest meaningful bin size in Q^2 is 0.01 GeV^2.

Figure 5.7 shows a comparison of data and JETSET 7.3 Monte Carlo in F_q^{vs} using Q^2 as the phase space variable. We see that both data and Monte Carlo now show a power-law like rise, the hallmark of intermittency, in particular for higher orders. There are small differences between Monte Carlo predictions and data in the small Q^2 range where the Monte Carlo overestimates the F_q^{vs}.

Power-law fit

The moments F_q^{vs} have been fitted with the power law [42]:

$$F_q^{vs}(Q^2) = a_q(Q^2)^{-f_q}, \qquad f_q > 0.$$

Since we plot lnF_q^{vs} as a function of -lnQ^2, taking the logarithm on both sides, the above equation becomes:

$$\ln F_q^{vs}(Q^2) = a_q - f_q \ln Q^2.$$

The parameters a_q and f_q have been fitted to the data using MINUIT [48] in the range $1 < Q^2 < 0.05$ GeV ^{2}. The results of the fit are presented in table 5.1. We observe that

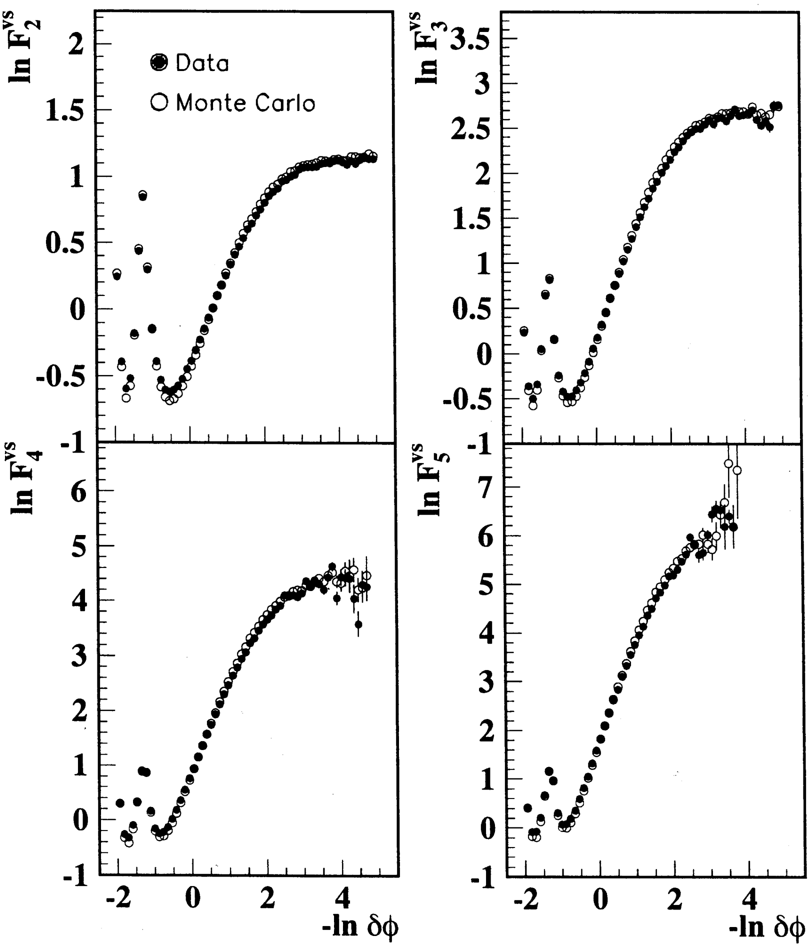

Figure 5.6: F_q^{vs} *for azimuthal angle* ϕ *measured in the plane transverse to the beam axis.*

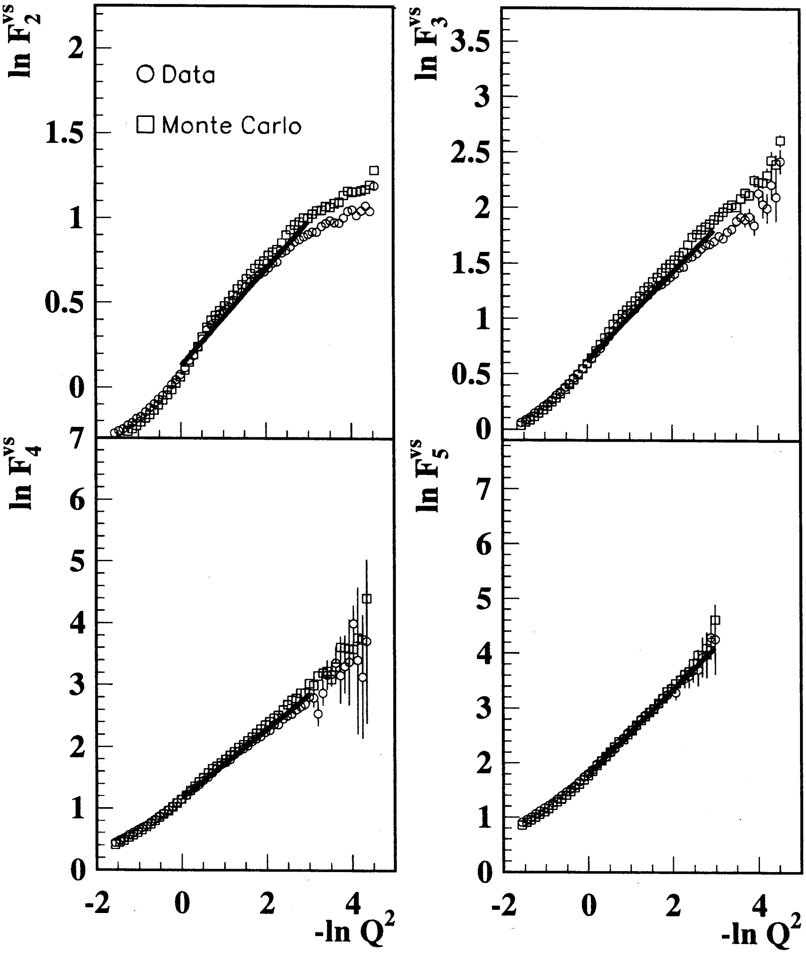

Figure 5.7: F_q^{vs} *for* Q^2 *for orders q=2,3,4 and 5, the solid lines are the result of power law fit to data*

the slopes increase in magnitude with increasing order of the moment. The numbers presented in this table are an indicator for the strength of intermittency found in our data. This strength is larger than that observed for hadronic collisions [49], but much smaller than expected from the QCD in the perturbative region, e.g. at $Q^2 \approx$ Z mass as calculated from DLLA [17].

Fit Parameters			
Order	f_q	a_q	χ^2/NDF
2	$0.285 \pm 0.10 \times 10^{-2}$	$0.127 \pm 0.15 \times 10^{-2}$	44/29
3	$0.396 \pm 0.21 \times 10^{-2}$	$0.622 \pm 0.23 \times 10^{-2}$	10/29
4	$0.561 \pm 0.50 \times 10^{-2}$	$1.158 \pm 0.41 \times 10^{-2}$	.91/29
5	$0.772 \pm 0.11 \times 10^{-1}$	$1.808 \pm 0.74 \times 10^{-2}$	.35/29

Table 5.1: *Values of the parameters f_q and a_q from power law fits to* F_q^{vs}

5.4.3 Charge dependence

To study the effect of charge on F_q^{vs}, we distinguish between a sample of all charged tracks which we call 'all charged', a combination of positive and negative tracks which we call 'mixed' sample, and combinations of like charges which we call 'positives' and 'negatives'. The normalization of each sample is carried out with a track pool of the same track combination, i.e. for the mixed sample the F_q^{vs} are normalized by uncorrelated events constructed from negative-positive track combinations taken from the track pool. We calculate F_q^{vs} separately for each of these samples.

Figure 5.8 shows F_q^{vs} for all of the above categories of charge combinations, except for positives, since these are very similar to the negatives. Figure 5.9 shows the same distributions for Monte Carlo events. Bose-Einstein correlations are included in Monte Carlo[1] We make the following observations:

- All charge combinations show a power-law like behaviour.
- At the large Q^2 (-ln$Q^2 < 0$), the slope is the same for all charge combinations. This is consistent with the expectation from QCD which does not distinguish between the charges.
- In the intermediate Q^2 region, the mixed sample shows a steeper rise of F_q^{vs} than the negatives. This difference can be attributed to resonances contributing to mixed. but not to negative combinations. Note that $-\ln Q^2 = 0.65$ corresponds to the peak of the ρ meson and $-\ln Q^2 = 1.77$ is the value corresponding to the K^0 mass.

[1] The parameter settings used to switch on the effect in JETSET 7.3 PS are: MSTJ(51)=1. MSTJ(52)=3, PARJ(92)=2.5 and PARJ(93)=0.2.

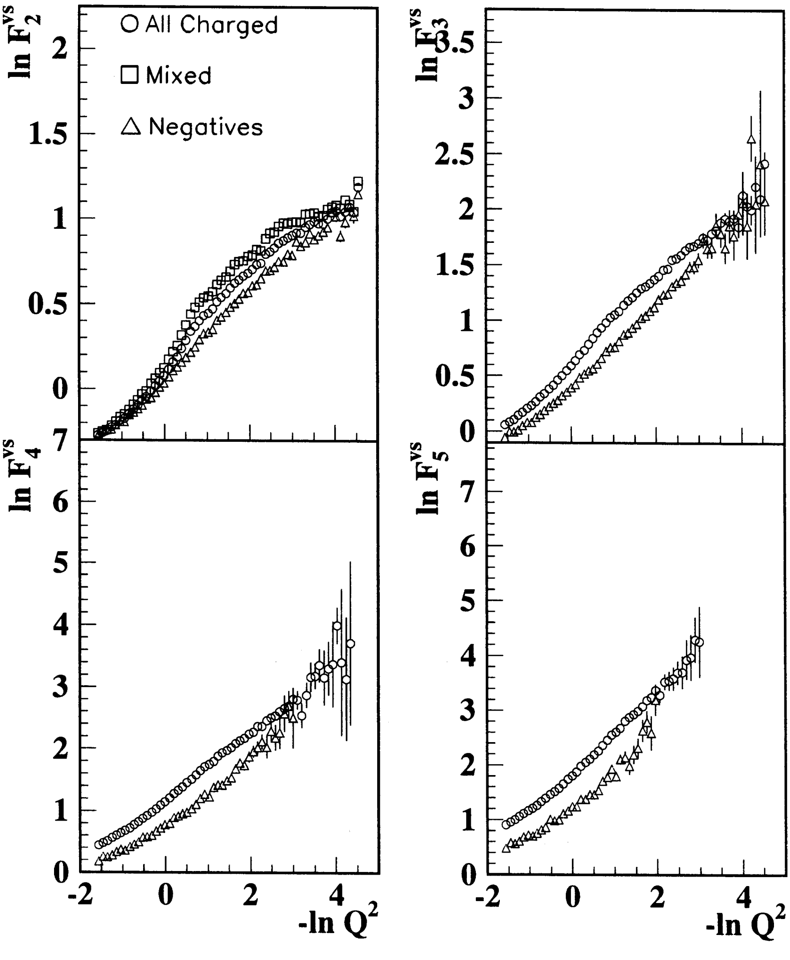

Figure 5.8: *Corrected data F_q^{vs} for Q^2 for orders q=2,3,4 and 5 with different combinations of charges. 'All' corresponds to all possible combinations, 'mixed' corresponds to positive-negative combinations only and 'negatives' corresponds to negative-negative combinations only.*

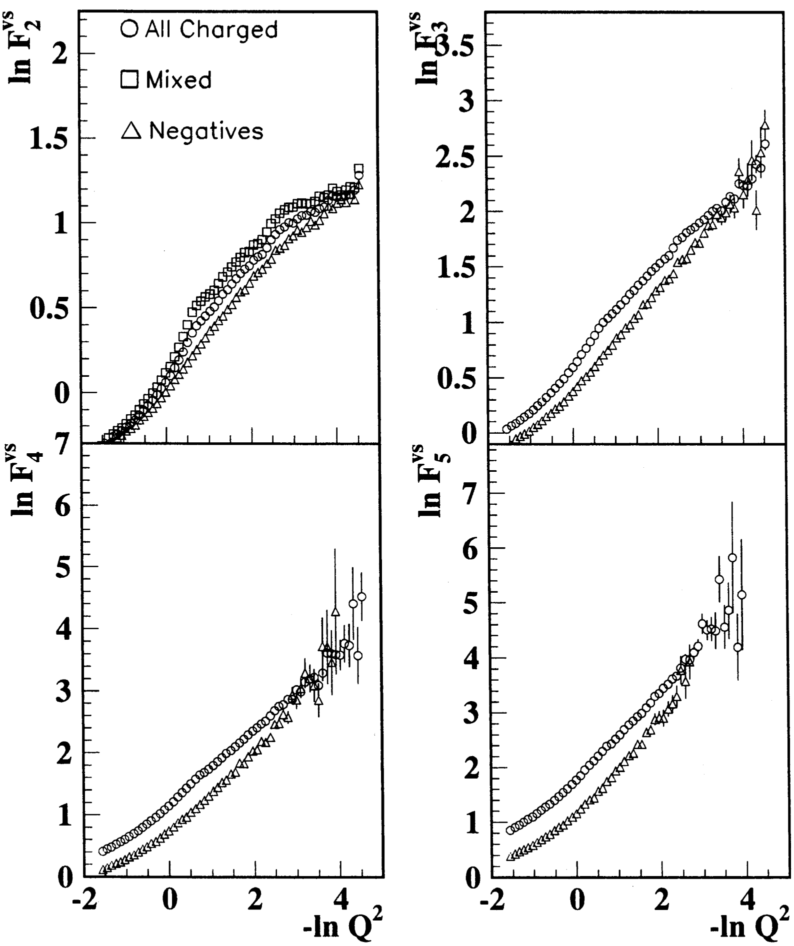

Figure 5.9: *JETSET 7.3 parton shower Monte Carlo* F_q^{vs} *for* Q^2 *for orders q=2,3,4 and 5 with different combinations of charges. 'All' corresponds to all possible combinations, 'mixed' corresponds to positive-negative combinations only and 'negatives' corresponds to negative-negative combinations only*

- In the small Q^2 region ($-\ln Q^2 > 2$), the mixed sample shows a tendency to flatten off, as expected from running coupling constant α_s. The negatives, however continue to rise, for the case of F_3^{vs} and F_4^{vs} even with an increased slope. It has been shown recently [49, 50] that this is due to the Bose-Einstein correlations dominating the like-charged combinations at these low Q^2 values.

- The Monte Carlo predictions show the same trend as the data but Monte Carlo overestimates F_q^{vs} in particular at the small Q^2.

5.4.4 Multiplicity dependence

To study the effect of multiplicity on the F_q^{vs} we have divided our data and Monte Carlo into two samples. The first sample contains events with a charged particle multiplicity of more than 15, the second of events with charged particle multiplicity of less than 15. We calculate the F_q^{vs} for these samples separately.

Figure 5.10 shows a comparison of F_q^{vs} for the above samples, for data as well as for Monte Carlo. We make the following observations:

- The low multiplicity sample shows a steeper rise of F_q^{vs} than the high multiplicity one.

- Furthermore, we observe that the slopes are different for the two samples only in the large Q^2 region and that they are almost the same in the small Q^2 region.

- The effect of resonance decays (e.g. seen as a peak at $-\ln Q^2 \simeq 0.65$) is much more pronounced in the second order moment and tends to fade out for higher order moments suggesting that the higher moments are better suited for studying intermittency.

- Monte Carlo predictions show the same trend as data. but Monte Carlo overestimates F_q^{vs} in the small Q^2 region. The agreement is very good in the large Q^2 region but in the small Q^2 region, i.e. above $-\ln Q^2 \simeq 2$, the Monte Carlo overestimates F_q^{vs}.

5.4.5 Jet topology dependence

To study the dependence of F_q^{vs} on jet topology, we extract from our data samples of events with two jets and with three jets. We use the JADE algorithm [51] with a $Y_{cut} = 0.02$.

Figure 5.11 shows the distribution of F_q^{vs} for both data and Monte Carlo. We observe that:

- For all cases there is a power-law like behavior and the 2-jet sample shows a steeper rise than the 3-jet sample.

- The Monte Carlo predictions reproduce the data distributions except in the soft Q^2 region where Monte Carlo overestimates F_q^{vs}.

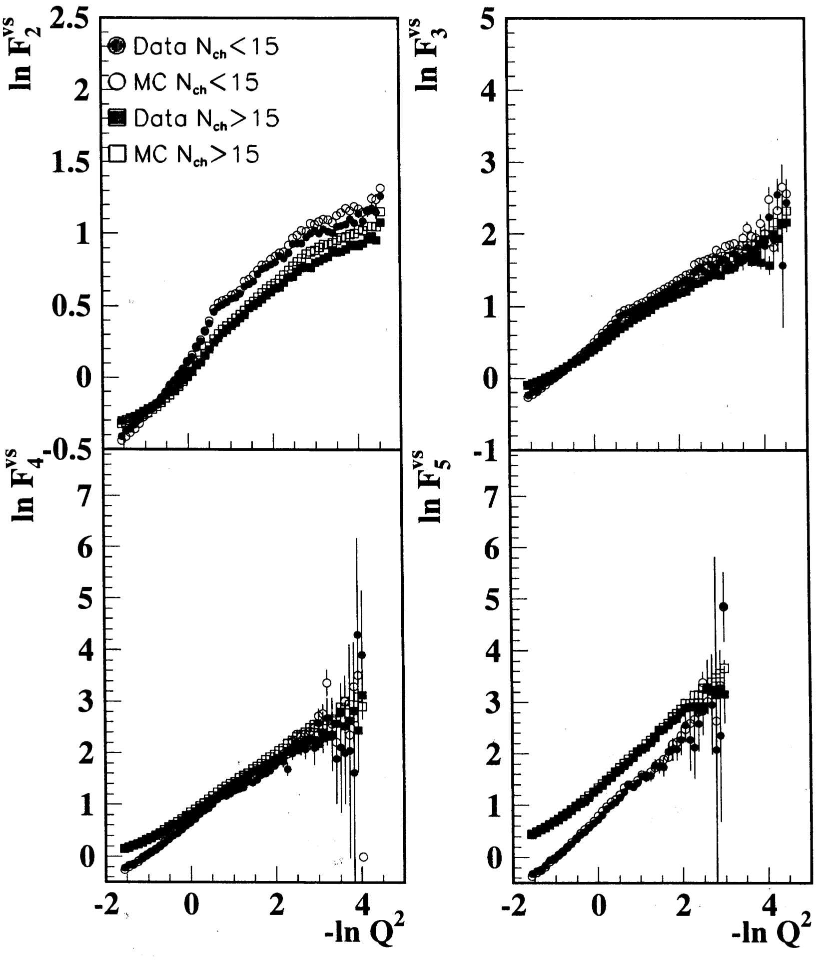

Figure 5.10: *Corrected data and JETSET 7.3 parton shower Monte Carlo* F_q^{vs} *for* Q^2 *for orders q=2,3,4 and 5, for multiplicity more than 15 and multiplicity less than 15 charged particles.*

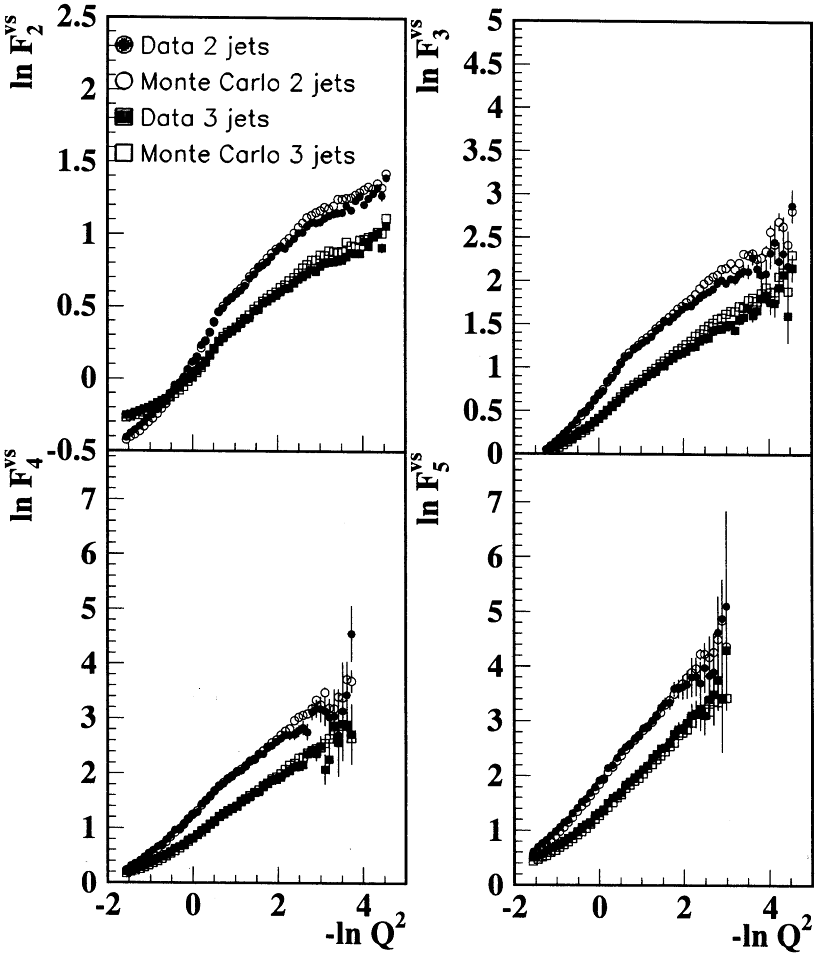

Figure 5.11: *Corrected data and JETSET 7.3 parton shower Monte Carlo* F_q^{vs} *for* Q^2 *for orders q=2,3,4 and 5 for 2-jet and 3-jet event samples.*

5.4.6 p_t dependence

In this section the dependence of F_q^{vs} on transverse momentum p_t is studied. We calculate the transverse momentum with respect to the thrust axis of each event. We use a cut on the p_t of every track ($p_t > 0.25$ GeV/c and $p_t < 0.25$ GeV/c) and calculate F_q^{vs} for both of these samples, for data as well as for Monte Carlo.

Figure 5.12 shows the distributions of F_q^{vs} both for data and Monte Carlo. We find that:

- The high p_t sample shows a larger slope and thus more intermittency than the low p_t sample in particular at small Q^2. This suggests that the effect of intermittency comes mainly from the hard part of the transverse momentum spectrum.
- The Monte Carlo shows the same trend as data but again overestimates F_q^{vs} in the small Q^2 region.

It is interesting to note that the deviation at small Q^2 ($-\ln Q^2 \geq 3$) observed in figure 5.7 mainly appears at small p_t.

5.5 Conclusion

We conclude from this study that we observe a signal for intermittency in e^+e^- collisions at LEP on the Z resonance. The signals are particularly well seen when using the four-momentum distance Q^2 as the phase-space variable. The effect is stronger than observed in hadronic collisions, but smaller than expected from QCD for the perturbative region (e.g. at μ=m_z). At $Q^2 > 1$ GeV^2, the effect is in agreement with the behaviour expected from QCD in the transition to the non-perturbative region. Resonances and Bose-Einstein interference contribute at lower Q^2. For the first time, a multiplicity dependence is seen also in e^+e^- collisions. It is present for $Q^2 > 1$ GeV^2, but not for smaller values. The effect is stronger in two-jets than in three-jets events and stronger in transverse momenta above average. The Monte Carlo program JETSET 7.3 PS provides a good qualitative description of the data, but tends to overestimate the effect at small Q^2 and small p_t.

In the future, there are two very important tasks to be performed. One is the verification of the analytical QCD predictions recently becoming available. This verification can best be done in terms of the interparticle angles. The second is the saturation at small binnings (high resolution) expected from the running α_s. In Q^2 an indication, so far, only exists for the mixed-charge combination, while like-charged combinations continue to increase down to the smallest Q^2 measured. Within L3, the Silicon Microvertex Detector used in the 1994 run can be expected to add the necessary resolution in the polar angle θ to study both of these effects.

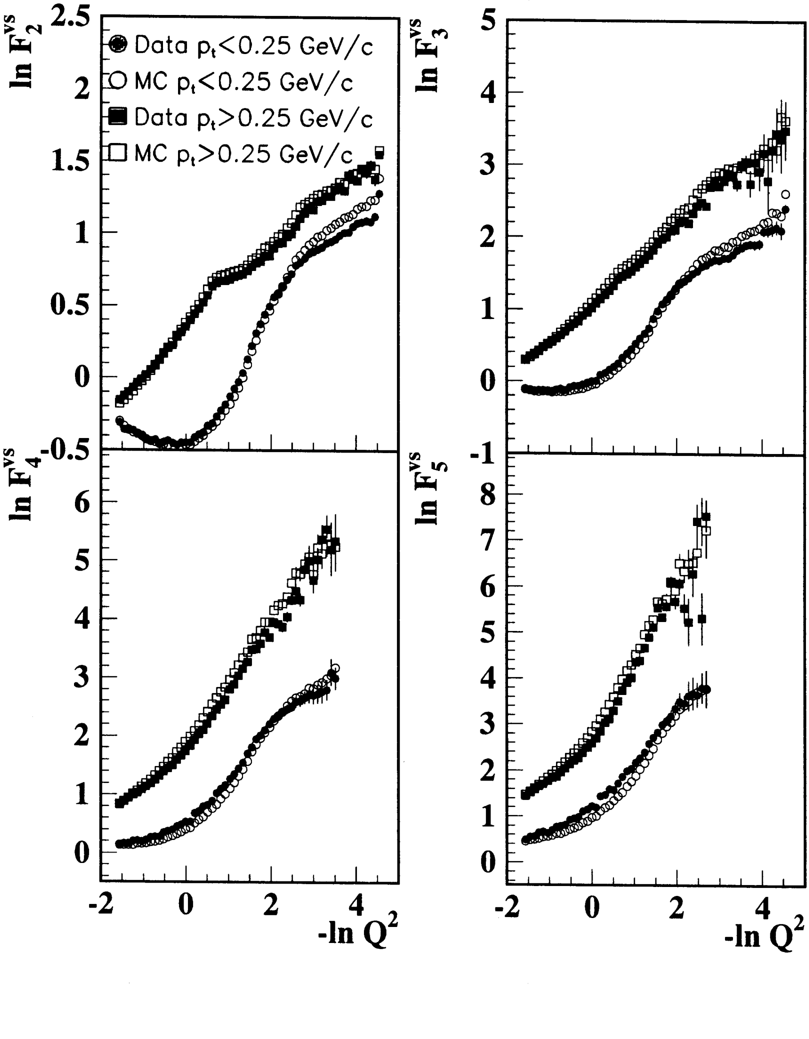

Figure 5.12: *Corrected data and JETSET 7.3 parton shower Monte Carlo* F_q^{vs} *for* Q^2 *for orders q=2,3,4 and 5 for events in which every track is selected with a criteria* $P_t > 0.25$ *or* $P_t < 0.25$.

Chapter 6

Coherence effects in QCD

6.1 Introduction

The phenomenon of colour coherence in the QCD parton shower development and its consequences have been presented in chapter 1. Although some investigators have claimed evidence for the coherence effects in the parton showers [52] others have not found convincing evidence [53].

Here we present an analysis performed on L3 data in an attempt to observe the intra-jet colour coherence effects. We observe angular ordering in parton showers, one of the consequences of coherence effects, and therefore infer colour coherence in the underlying partonic system. We compare our results with predictions from Monte Carlo models.

First we discuss the method we use to study angular ordering, we justify the use of some Monte Carlo models whose predictions we compare with our data and finally we present our results and we draw the conclusion from this study.

6.2 Particle correlations as a tool

Angular ordering (AO) in parton showers is one of the consequences of the coherence effects in perturbative QCD. As described in section 1.4, colour coherence implies that in a parton shower, subsequent partons are emitted at an ever decreasing angle with respect to their parent parton. The situation is depicted in figure 6.1 where the angular ordering condition dictates that: $\Theta_1 > \Theta_2 > \Theta_3 \ldots$.

The idea of Local Parton Hadron Duality (LPHD) has been proposed in [54]. This idea suggests a correspondence between the analytically described features of the partonic system and the corresponding characteristics of the final state hadronic system. Experimentally, one has the possibility of observing the general features of the hadronic systems produced in hard processes, such as multiplicity distributions, inclusive energy spectra and correlations, angular patterns of multiplicity and energy flow. LPHD allows to compare them to the predictions of perturbative QCD directly, without invoking any fragmentation scheme. Experimental data indeed indicate the presence of the LPHD

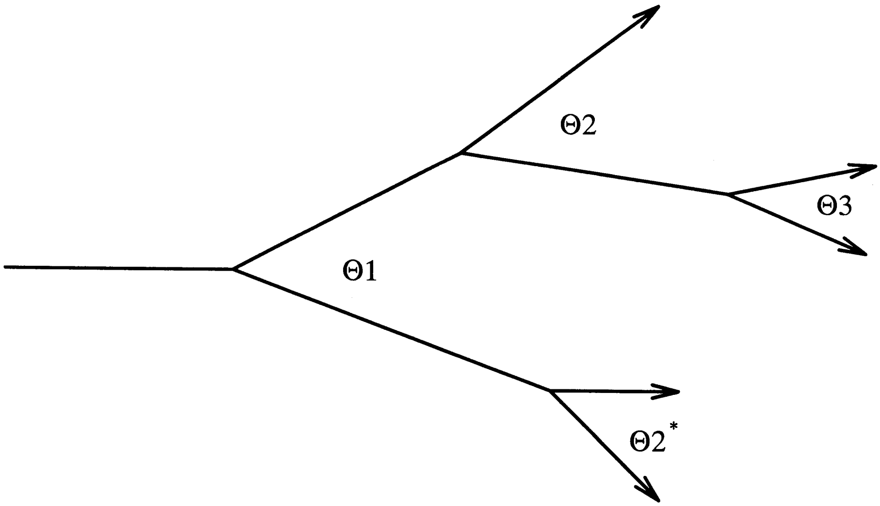

Figure 6.1: *Angular-ordering in subsequent parton branchings in a parton shower.*

phenomenon [55, 56].

Considering AO as a consequence of QCD colour coherence and assuming LPHD, one can test the data for the existence of coherence in the angular correlation of the particles produced in the hadronic final state of e^+e^- collisions at LEP. We use the so-called 'Particle Particle Correlation Asymmetry' (PPCA) [57, 58] for our analysis. The 'Particle-Particle Correlations' (PPC) are the same as the 'Energy-Energy Correlations' (EEC) [59] except for the energy weighting of the EEC. The PPC are given by:

$$\mathrm{PPC}(\chi) = \frac{1}{N_{\mathrm{Event}}} \frac{1}{\Delta\chi} \sum_{1}^{N_{\mathrm{Event}}} \sum_{i=1}^{N_{\mathrm{ch}}} \sum_{j=1}^{N_{\mathrm{ch}}} \frac{\delta(\chi_{\mathrm{bin}} - \chi_{ij})}{N_{\mathrm{ch}}^2}$$

where χ_{ij} is the angle between any two charged particles i and j in an event, $\Delta\chi$ is the bin size, χ_{bin} is the value at the center of a bin, $\delta(\chi_{bin} - \chi_{ij})$ is 1 for angles χ_{ij} inside the bin around χ_{bin} and 0 otherwise, N_{ch} is the number of charged particles in an event, and N_{Event} is the total number of events in the sample.

As will be explained shortly, the asymmetry of the PPC, defined as

$$\mathrm{PPCA}(\chi) = \mathrm{PPC}(180^\circ - \chi) - \mathrm{PPC}(\chi),$$

reveals differences between the two halves of an event, if the event is divided into two hemispheres. Since at LEP the fraction of 2-jet events is very high, the PPCA actually compares the PPC between particles in the same jet ($\chi < 90°$) of the event with the PPC between particles in different jets ($\chi > 90°$). Let us consider PPC between particles belonging to the same jet and call this correlation PPC_{ii} and correlation between particles belonging to different jets we call PPC_{ij}. If the particles in each jet have a similar angular structure then the two correlations PPC_{ii} and PPC_{ij} would be similar and the PPCA would be approximately zero. If however, the angular structure within the jets is not similar then the correlations PPC_{ii} and PPC_{ij} would be different, resulting in the PPCA being significantly non-zero.

Figure 6.2(a) and (b) show a graphic representation of an angular-ordered and a non-

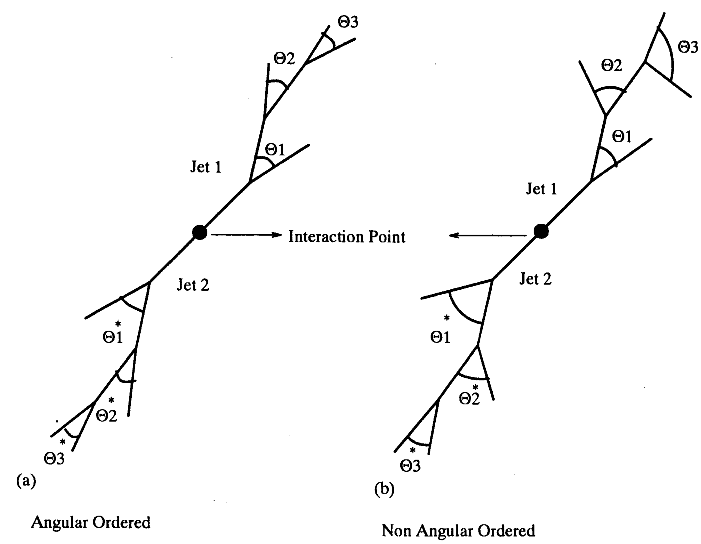

Figure 6.2: *Picture depicting (a) parton shower with angular ordering, (b) parton shower without angular ordering*

angular-ordered parton shower, respectively. One can see, that in the case of angular-ordering (figure 6.2(a)), there is an underlying symmetry, namely $\Theta_1 > \Theta_2 > \Theta_3 \ldots$, in each jet. One can visualize that one would get less asymmetry in this case if one compares the angular correlations between the two jets. On the other hand, in the case of non-angular-ordered jets, the underlying symmetry is absent and one can deduce that the amount of asymmetry between the two jets in this case would be larger (see figure 6.2(b)).

6.3 Monte Carlo models

In the present study we compare our data with the predictions of JETSET 7.3 PS [60], ARIADNE 4.4 [61] NLLJET 2.0 [62], HERWIG 5.6 [63] and COJETS 6.23 [64]. These

Monte Carlo programs differ widely in their implementation of the perturbative QCD and fragmentation processes.

- The JETSET 7.3 PS. parton shower Monte Carlo program simulates e^+e^- annihilation into partons with subsequent quark and gluon branchings. It is based on the leading logarithmic approximation with an option to choose between angular-ordered and non-angular-ordered parton showers. The JETSET program provides the choice of string fragmentation or independent fragmentation. We have used the string fragmentation option.

- ARIADNE 4.04. is a parton shower based Monte Carlo program. It treats the initial $q\bar{q}$ generated by another program (JETSET 7.3 in our case) as a colour dipole which radiates a gluon. The dipole is then replaced by two dipoles formed by qg and $g\bar{q}$ which in turn can radiate creating additional gluons and dipoles, thus producing a shower. This formulation naturally incorporates interference phenomena of perturbative QCD as ordering of P_t of the subsequent branchings. ARIADNE uses the fragmentation routines of JETSET 7.3 for fragmentation. We have used the string fragmentation option.

- NLLJET 2.0 is a parton shower Monte Carlo program based on the next-to-leading logarithmic approximation. It provides the option of generating angular-ordered or non-angular-ordered parton showers. Like ARIADNE it does not provide its own fragmentation routines, but uses the fragmentation routines of JETSET 7.3.

- HERWIG 5.6 is a Monte Carlo program based on parton shower simulation within the framework of the leading logarithmic approximation. It incorporates a very detailed simulation of QCD interference phenomena and treatment of parton shower development. The fragmentation is performed by a cluster fragmentation model.

- COJETS 6.23 is a Monte Carlo program which simulates the multiple gluon radiation in the leading logarithmic approximation with incoherent branching. This simulation is integrated with independent jet fragmentation.

6.3.1 Assessing the quality of Monte Carlo models

The Monte Carlo models described above have been tuned to L3 data by fitting several event shape variables [37]. It has been found that the best description of the data is provided by the JETSET 7.3 PS program with angular ordering. In what follows we will use the JETSET 7.3 PS description of one dimensional distributions as representative of the data. We use some event shape variables such as Thrust, Major, Minor, Sphericity, and Aplanarity to check if JETSET 7.3 PS without angular ordering and NLLJET 2.0 without angular ordering predict similar event shape quantities as their angular-ordered counterparts. For this purpose, we use the predictions of JETSET 7.3 PS with angular-ordering as a reference.

Figure 6.3 shows the event shape variable distributions for JETSET 7.3 PS with and without angular ordering. We find that the distributions for all variables with angular ordering are in good agreement with those without angular ordering.

Figure 6.4 shows the event shape variable distributions for JETSET 7.3 PS with angular ordering and NLLJET 2.0 without angular ordering. We observe significant differences between the models for all variables.

The distributions of JETSET PS, HERWIG, ARIADNE and NLLJET all with AO have been found to be in good agreement with data, especially in the 2-jet and 3-jet region [37], however, NLLJET does not reproduce the data in the multi-jet production dominated region. COJETS gives slight differences in variables describing the transverse structure of an event such as oblateness and 2-jet production dominated regions where it produces 2-jet events which are slightly narrower. The distributions of NLLJET with AO give results very similar to those of NLLJET without AO and are not shown here.

We conclude that since JETSET 7.3 PS AO, ARIADNE 4.04, HERWIG 5.6, JETSET 7.3 PS NOAO (NOAO stands for no-angular-ordering) and COJETS 6.23 all agree well with the data for one-dimensional distributions, a comparison of the observed PPCA with the predictions is warranted. In the case of NLLJET 2.0, we find that the model fails to describe the event shape variables both with and without angular ordering.

6.4 Assessing the effect of Monte Carlo parameters on PPCA

To check the sensitivity of PPCA to the Monte Carlo parameters, we use JETSET 7.3 PS to calculate the PPCA after changing the tuned parameters by one standard deviation one at a time. Table 6.1 gives the values of these fitted parameters taken from [37]. The value of parton shower termination parameter Q_0 is set to 1 GeV in our analysis.

Parameter	$Q_0 = 1$ GeV	$Q_0 = 2$ GeV
Λ_{LL} (GeV)	0.30 ± 0.03	0.29 ± 0.03
σ_q (GeV)	0.39 ± 0.03	0.48 ± 0.05
b (GeV^{-2})	0.76 ± 0.08	0.82 ± 0.10
χ^2/(Data Points)	19.4/36	24.7/36

Table 6.1: *The optimized parameter values for JETSET 7.3 PS Monte Carlo program with different values of the parton shower termination parameter Q_0. The fragmentation parameter a is set to its default value of 0.5. We use $Q_0 = 1$ GeV in our analysis.*

Figure 6.5 shows the effect of changing the scale Λ_{LL}, the width of the Gaussian transverse momentum distribution of the primary quarks σ_q , and the b parameter in the symmetric Lund fragmentation function [65]. We see that the PPCA is not very sensitive to these changes in parameters.

6.5 Effect of Bose-Einstein correlations on PPCA

To determine the effect of Bose-Einstein correlations (B.E.) on the PPCA, we use JETSET 7.3 PS with angular ordering. Figure 6.6 compares the PPCA from this program run with and without B.E. We observe that at small angles, from 0° to 18°, the effect of B.E is rather large but that it decreases for larger angles. JETSET 7.3 PS is used with B.E switched on in this study.

6.6 Calculating the PPCA

To calculate the PPCA, we use charged particles from the selected data sample described in chapter 4. The bin size of 6° is much larger than our two-track resolution for the angle in space between two tracks, ψ_{12}, as discussed in section 4.7.2. We compare the PPCA calculated from the data with the predictions of the Monte Carlo programs briefly described above.

Figure 6.7 shows the PPCA as a function of χ for the JETSET 7.3 PS model with and without AO. We point out here, that the bins below 18° should not be considered since these bins may include rather large effects from Bose Einstein correlations as shown in section 6.5. The angular region between 55° and 90° is not relevant since this region corresponds to the asymmetry of the correlations in the inter-jet region. Thus, the region of interest lies between 18° and 55°, which also corresponds to the average jet opening angle. As seen in figure 6.7, there is a large difference in this region between JETSET 7.3 with and without angular ordering.

6.6.1 Correction of PPCA

Comparison of data with the predictions of a Monte Carlo model is done best if the effects of detector acceptance and limited resolution are included by Monte Carlo simulation of detector effects. This process, however, requires so much computer time that it is not feasible. Therefore, to make a comparison between data and the various Monte Carlo models without doing detector simulation, we correct our data for detector effects using $\approx$ 150k events generated by JETSET 7.3 PS with detector simulation. The option of angular ordering in parton showers is used to generate these events. We first correct the PPC(χ) distribution and then calculate the PPCA(χ) from this corrected distribution. The correction factors C_i^{PPC} for PPC(χ) are calculated bin by bin as follows: Let N_i^{P} be the number of entries in bin i of the input PPC distribution at the generator level, and N_i^{D} be the number of entries in bin i of the PPC distribution at the detector level (i.e., after detector simulation and event selection), then the correction factors C_i^{PPC} are

$$C_i^{\mathrm{PPC}} = \frac{N_i^{\mathrm{P}}}{N_i^{\mathrm{D}}}.$$

These correction factors are applied to the data PPC(χ) distribution to obtain the corrected distribution of PPC(χ) as follows:

$$\mathrm{PPC}_i^{\mathrm{Corr}} = \mathrm{C}_i^{\mathrm{PPC}} \cdot \mathrm{PPC}_i^{\mathrm{Uncorr}}$$

where $\mathrm{PPC}_i^{\mathrm{Uncorr}}$ is the measured PPC value in the ith bin, PPC_i^{Corr} is the corrected PPC value in the ith bin and $\mathrm{C}_i^{\mathrm{PPC}}$ is the correction factor in the ith bin. Using this corrected distribution of PPC(χ), we calculate the corrected distribution of PPCA(χ) as follows:

$$\mathrm{PPCA}_{\mathrm{corrected}}(\chi) = \mathrm{PPC}_{\mathrm{corrected}}(180^\circ - \chi) - \mathrm{PPC}_{\mathrm{corrected}}(\chi).$$

6.7 Results

Figure 6.8 shows a comparison of our corrected data with the incoherent Monte Carlo models. We see that in the region of interest, JETSET 7.3 PS without angular ordering disagrees with the data. COJETS 6.23 is seen not to reproduce the data over the entire angular range. However, NLLJET 2.0 without angular ordering lies very close to the data points.

The comparison with the coherent Monte Carlo models is shown in figure 6.9. We see that all the coherent models reproduce the data over the full angular range except NLLJET 2.0 with angular-ordering. NLLJET overshoots the data and, unlike both the data and the other Monte Carlo predictions, shows a positive asymmetry.

6.8 Conclusion

From the above study, we conclude that the PPCA is a good variable to distinguish between angular-ordered and non-angular-ordered parton showers. The comparison of data with Monte Carlo models with and without QCD coherence effects reveals that the PPCA for data is best reproduced by models that include coherence effects. The models which do not include coherence effects in parton showers fail to describe PPCA observed in the data. The only exception to this conclusion is provided by the NLLJET model where the non angular ordered model best fits the data. However since NLLJET does not reproduce the one-dimensional distributions (see section 6.3.1), this discrepancy cannot be attributed to angular ordering.

We conclude, therefore, that the data indicate the presence of QCD coherence effects in parton showers.

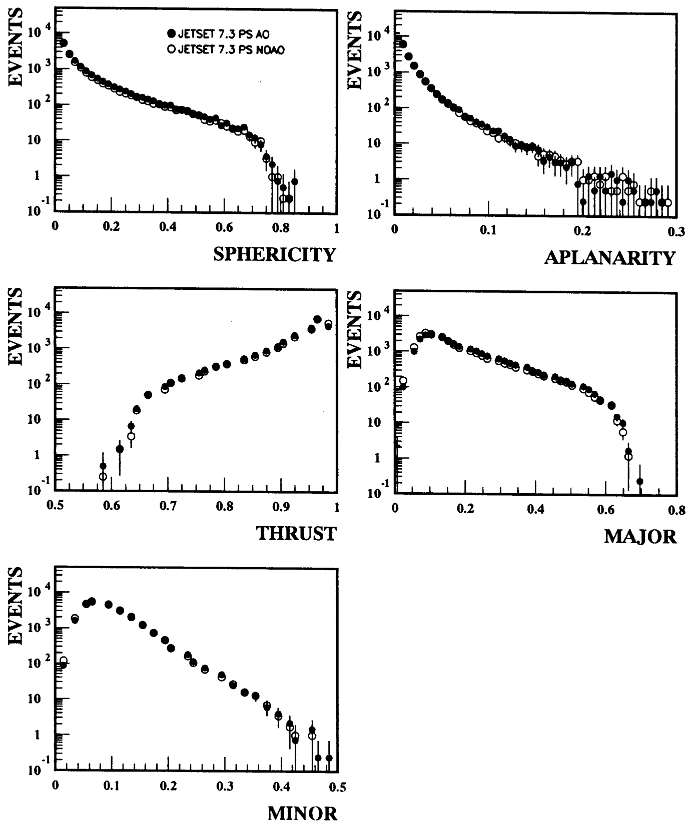

Figure 6.3: *Comparison of event shape variables for JETSET 7.3 PS with angular ordering AO and JETSET 7.3 PS without angular ordering (NOAO).*

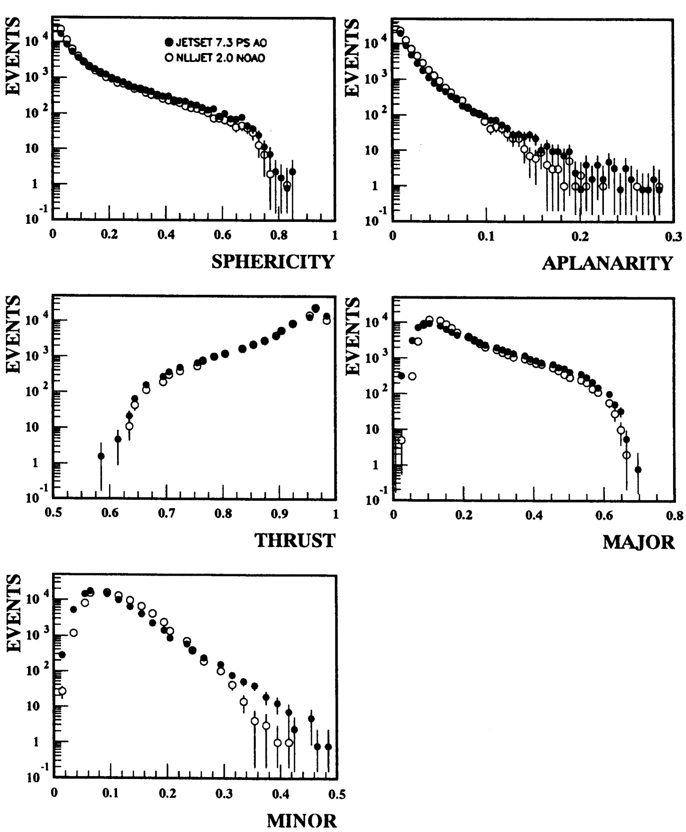

Figure 6.4: *Comparison of event shape variables for JETSET 7.3 PS with angular ordering AO and NLLJET 2.0 without angular ordering (NOAO).*

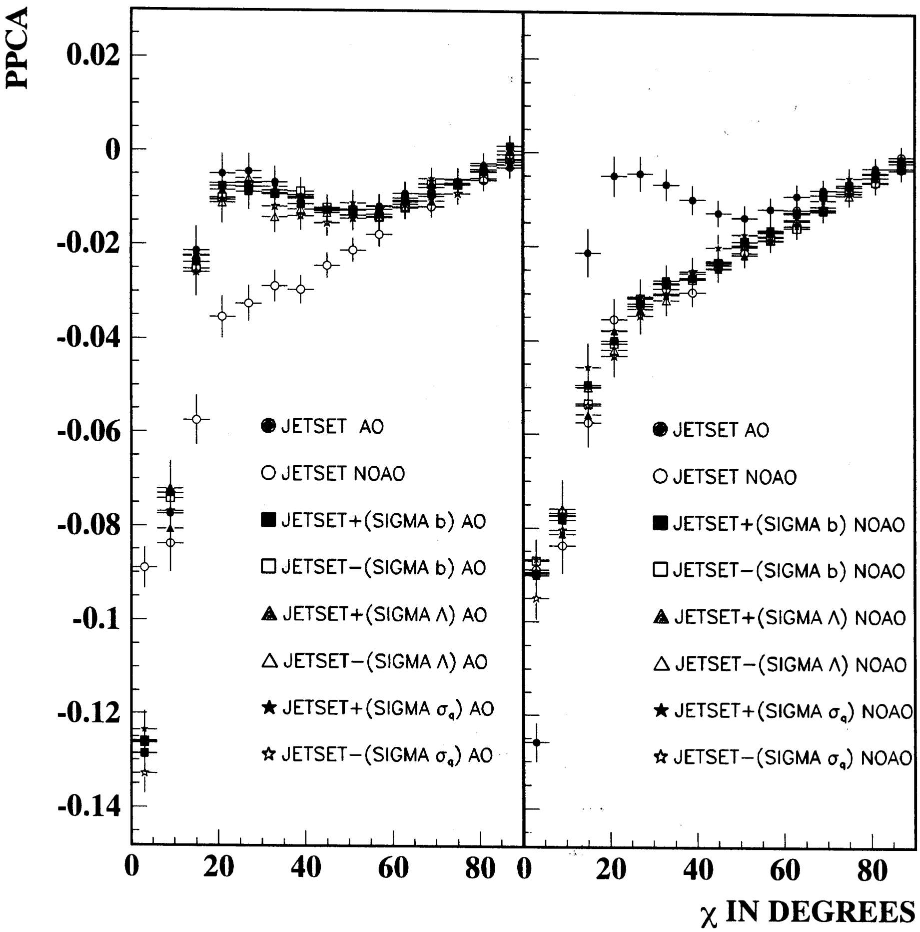

Figure 6.5: *Effect of varying the JETSET 7.3 PS parameters around their fitted value by one standard deviation. Each parameter is varied while keeping the others at the fitted value*

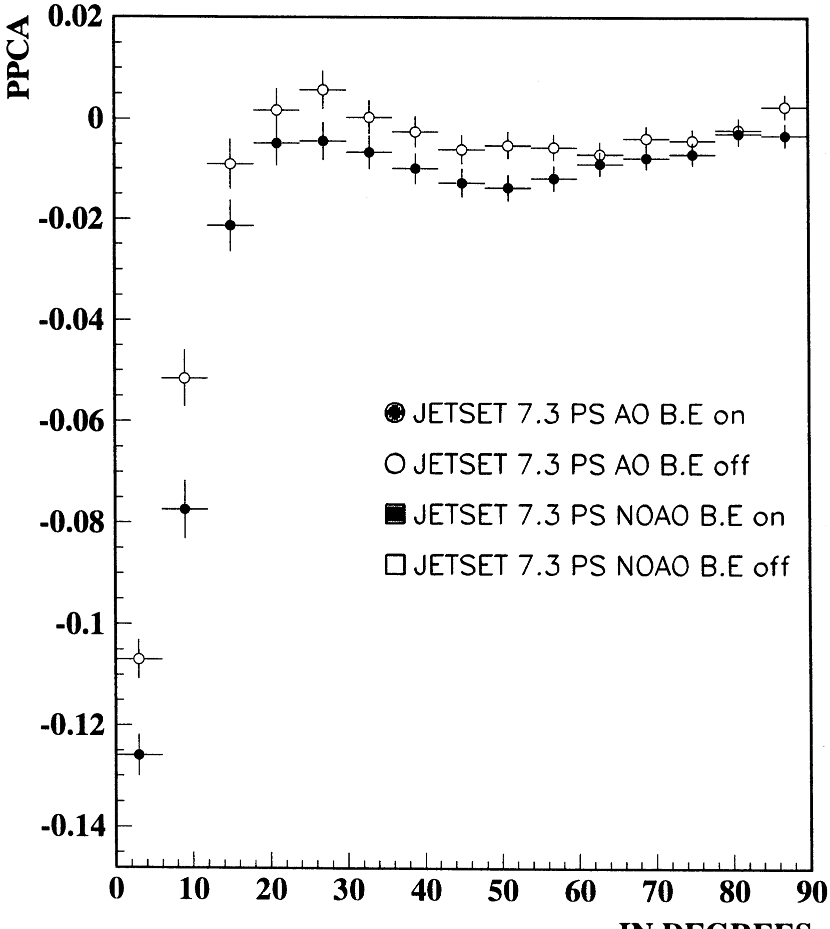

Figure 6.6: *Effect of Bose Einstein correlations on PPCA*

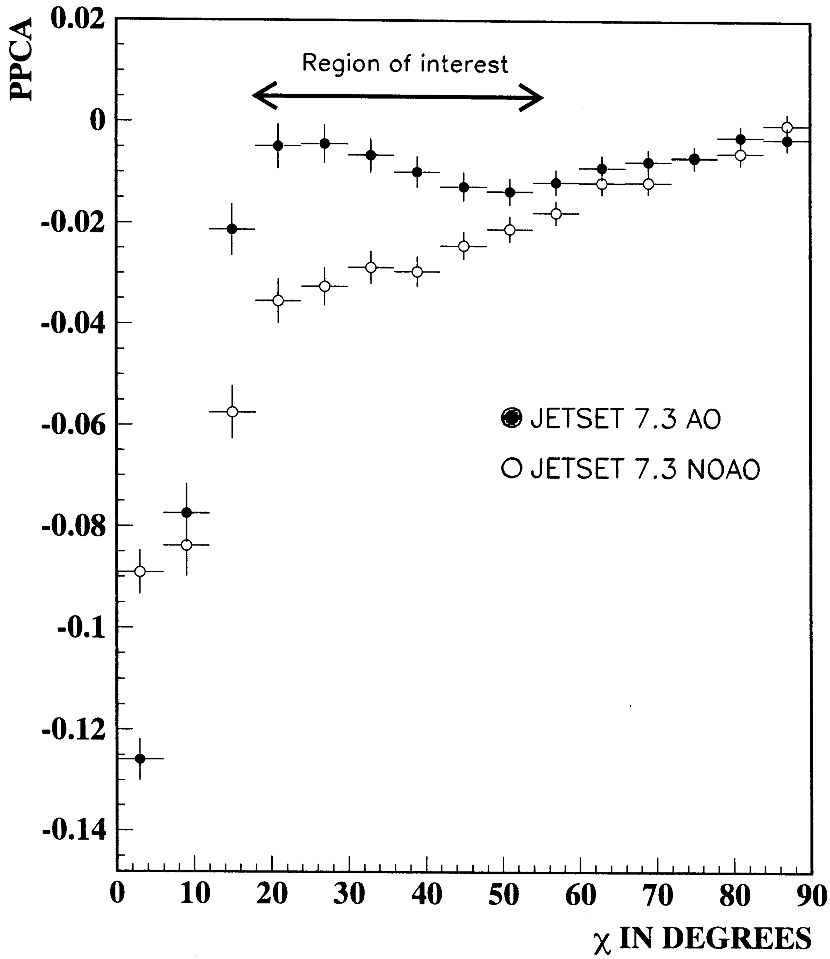

Figure 6.7: *Particle Particle Correlation Asymmetry as predicted by the JETSET 7.3 PS program for angular-ordered (AO) and non-angular-ordered (NOAO) parton showers.*

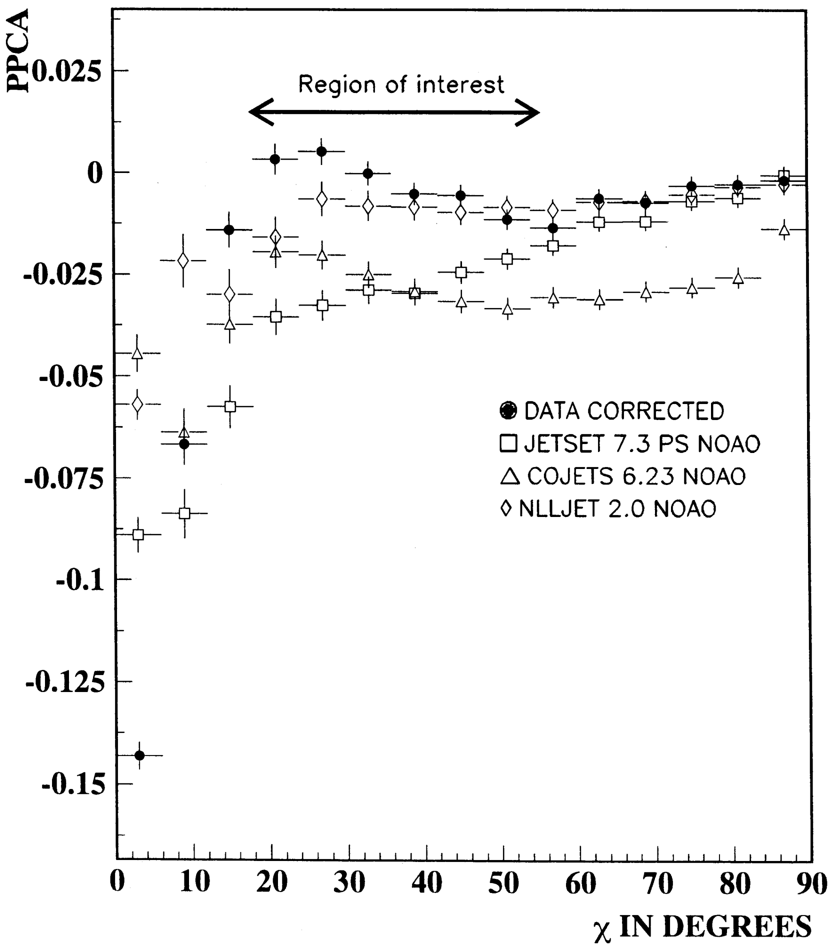

Figure 6.8: *Comparison of PPCA between data and predictions of incoherent Monte Carlo models, NOAO stands for no angular ordering.*

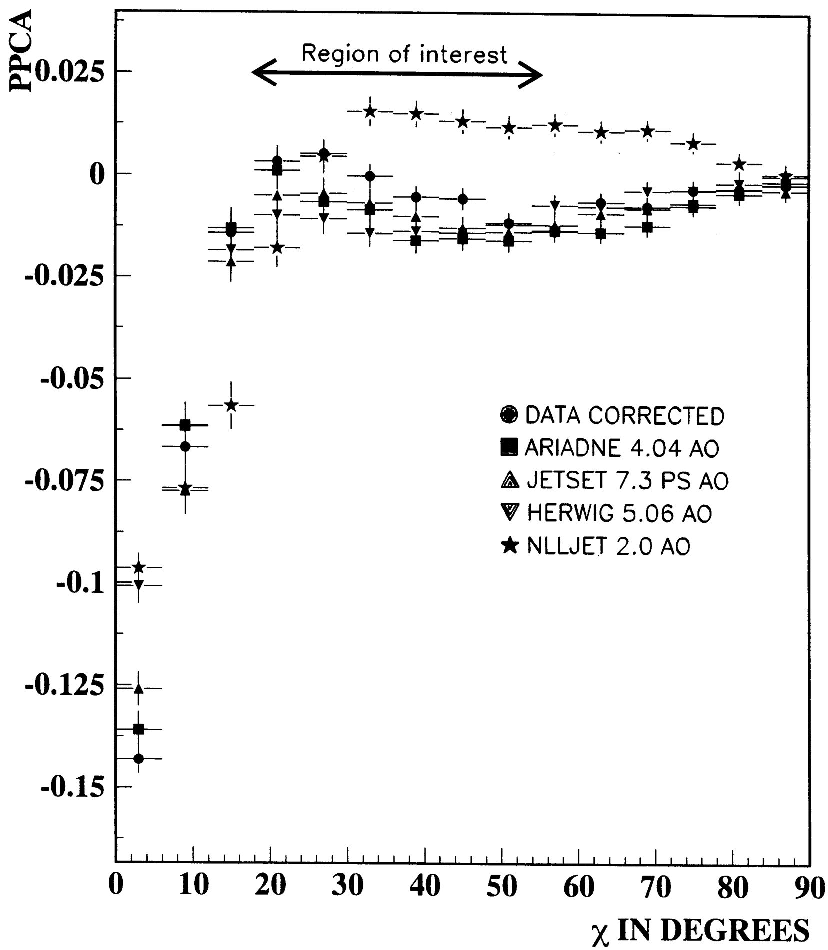

Figure 6.9: *Comparison of PPCA between data and predictions of coherent Monte Carlo models, AO stands for angular ordering.*

Appendix A

Structure of the L3 run control database

A.1 Structure of the L3 run control database

We describe here the structure of the L3 run control database in brief giving the purpose of the various directories, their contents, and the keys used to identify their objects.

//DBL3

This directory serves as the stem for the database tree. The name of this directory can be chosen at the time of database initialisation. It is not necessarily DBL3 as shown in the figure 3.4 but can be different character strings thus making it possible to work with more than 1 database file in the same program.

/DICTIONARY

This directory is automaticaly created by the DBL3 package at the time of the creation of the database . It contains information about each directory, such as the last date of modification. The user can store simple alias names for pathnames as well as mnemonics for data objects.

/HELP

Help information about the directories in the database can be stored in this directory in ASCII format.

/CORPAM/xxL3

This directory contains corrections needed by the official L3 programs in a trackable manner in the form of correction cradles (a set of instructions to PATCHY to make changes in the code) which should be applied to the offical PAM (PATCHY Master) file while making an executable program. These corrections are officially released by the collaboration.

For each PAM file of the L3 code, for example SIL3, REL3, UTL3, etc., there exists a corresponding Corpam subdirectory xxL3 where xx is SI for SIL3, RE for REL3 etc. These subdirectories xxL3 contain correction cradles for the corresponding PAM file.

The keys used for identification of corrections are as follows:

- Key 5 = PAM Version number
- Keys 8-9 = Name of the author of corrections (Hollerith)

/TEST/GO

Originally this directory was foreseen to contain examples for making and running programs (PATCHY, compilation and loading procedures , data cards). The key structure for this directory is the same as explained below for the /Program directory. Although although it still exists in the database, it is only used for test programs. Instead, the example programs are placed on a separate disk from where all users can easily access them.

/PROGRAM

The contents of this directory are the templates for running production jobs. The templates, identified using PMCC, contain some wildcard fields which are substituted automatically at the execution time along with a standard procedure that is performed by each job. The keys used in this directory are:

- Key 5 = PMCC
- Key 8 = Steering PAM file name for the program (Hollerith)
- Key 9 = Official version number of the program
- Key 10-11 = Program name (Hollerith)

/PROGRAM/FIXUP

This directory was foreseen to contain any emergency fixups made to the programs 'a la PATCHY'. However, in practice this directory is never used since the corrections are always taken from the Corpam directory and since a need for emergency fixups did not arise. The keys used are:

- Key 5 = Fixup ID
- Key 8 = PMCC ID

/PROGRAM/MODULE

The contents of this directory are pointers in the computer filling system to the physical location of the executable module. Extra information about module creation can be added in ASCII format. The keys used are:

- Key 5 = Module ID (The JODIB of the program that produced the module)
- Key 8 = PMCC (PPP, M_{DC} and CC fields only)

/PROGRAM/DATACARD

A template of datacards is stored in this directory. This template has wildcards for a number of parameters that the user can change and for the input and output filenames. At the time of execution of the job, the wildcard parameters are substituted automatically. The key structure for this directory is:

- Key 5 = Datacard ID
- Key 8 = PMCC

/FIELDMAP

The field map of the L3 magnetic field is stored in this directory. The keys have the usual DBL3 meaning and no special keys are defined for this directory. Key 5 in this directory is the magnetic field configuration ID.

/JOBLOG/RUNID

The purpose of this directory is to create a link between the online L3 run number and the JOBID of the program processing the data. All the information is kept in the keys. The key layout of the directory is as follows:

- Key 5 = JOBID of the job
- Key 8 = PMCC
- Key 9 = L3 run number

/JOBLOG/SIMU/RUNID

The structure and purpose of this directory is the same as /Joblog/Runid except that it is used for Monte Carlo production jobs.

- Key 5 = JOBID of the reconstruction program
- Key 8 = PMCC
- Key 9 = Run number = Simulation JOBID

and that Key 9 is the JOBID of the job which generated the events being reconstructed.

/JOBLOG/SIMU/SUBMIT

This directory contains information about the production job submission such as the JOBID of the job, the program ID and name, the name of the user, name of the computer that the user used to submit the job, the name of the computer where the job will is run, and the whole command line given for job submission. Only the Monte Carlo jobs make entries in this directory, the data jobs make entries in /Joblog/Submit directory. The key layout of this directory is as follows:

- Key 5 = Jobid of the job
- Key 8 = PMCC
- Key 9 = Module ID
- Key 10 = Datacard ID
- Key 11 = Template ID

/JOBLOG/SIMU/CHECK

When a job has finished, it is checked and the information about the job status, such as good or bad, is logged into this directory in the form of keys. Only the Monte Carlo jobs are checked in this directory, the data jobs are in the directory /Joblog/Check. The keys are as follows:

- Key 5 = JOBID of the job
- Key 8 = Check status

/JOBLOG/SUBMIT

The structure and purpose of this directory is the same as that of /Joblog/Simu/Submit, but it is used for data production jobs.

/JOBLOG/CHECK

The same as /Joblog/Simu/Check, but for data jobs.

/JOBLOG/SPLIT

After reconstruction, the events are split into different steams for analysis depending on the selection criteria they pass. The job that splits the events streamwise makes entries into this directory. This directory does not contain any data but just keys described below.

- Key 5 = JOBID of the split job

- Key 8 = Reconstruction JOBID
- Key 9 = Run Number
- Key 10 = Switches for DRE
- Key 11 = Switches for DSU
- Key 12 = Number of input events
- Key 13 = Number of output events
- Key 14 = Number of write operations

each of the Keys 15 to 26 contain the number of events written out in a particular data stream.

/JOBLOG/CCAT

Once there are enough events of a particular type in the split stream files, a job is run to concatenate events of a given stream into a single file normaly on a tape. This job makes an entry into this directory. The keys in this directory are:

- Key 5 = JOBID
- Key 8 = JOBID of the reconstruction
- Key 9 = JOBID of the Split job
- Key 10 = Tape identifier in base 36
- Key 11 = Concatenation type in Hollerith permanent/temporary
- Key 12 = Dummy
- Key 13 = Dummy

keys 12 and 13 are left for future use.

/RUNLOG/DACQ

The data part of this directory contains the information about the essential run parameters such as the beam energy, beam intensity, luminosity and status of L3 magnet. An entry is made in this directory by the data acquisition program at the start and end of each run. The keys of the directory are:

- Key 8 = Run number
- Key 9 = Tape number

- Key 10 = Start or End of run Run
- Key 11 = Fill number
- Key 12 = Energy measured
- Key 13 = Energy nominal
- Key 14 = Fast bus readout status
- Key 15 = High voltages on/off
- Key 16 = Level 1 Trigger mask
- Key 17 = Run Type
- Key 18 = number of events written in case of end of run
- Key 19 = Luminosity Monitor status open/close
- Key 20 = Current in the magnet
- Key 21 = E_FLIP
- Key 22 = Number of Bhabha events uncorrected
- Key 23 = Number of Bhabha events corrected
- Key 24 = Lifetime of the beam
- Key 25 = DUMMY
- Key 26 = DUMMY
- Key 27 = DUMMY

/RUNLOG/SIMU/GENE

Every job generating Monte Carlo events makes entries into this directory. The data part of this directory contains a bank with some generator parameters and results. The keys in the directory are:

- Key 5 = JOBID of the generator job
- Key 8 = PMCC
- Key 9 = Center of mass energy
- Key 10 = Number of events generated
- Key 11 = Special condition number for final state

- Key 12 = Special condition number for datacards
- Key 13 = Cross section calculated by the generator

/RUNLOG/SIMU/SIL3

Every simulation job writes into this directory a set of keys which are later used by the user to make connections between generated and reconstructed events. The contents, which are only keys, are described below:

- Key 5 = JOBID of the simulation job
- Key 8 = PMCC
- Key 9 = JOBID of the generator job
- Key 10 = Number of events
- Key 11 = Special condition number for simulation
- Key 12 = Special condition number for datacards
- Key 13 = First event on the file simulated

/FLUM

Luminosity information calculated by the reconstruction program is stored in this directory which is later updated by other standalone programs that compute more accurate luminosity using better calibrations when they become available.

The description of keys is:

- Key 5 = JOBID of the program
- Key 8 = Pass-1 JOBID
- Key 9 = Run number
- Key 10 = Luminosity analysis version
- Key 11 = Beam energy in keV
- Key 12 = Begining time of the time period used for analysis
- Key 13 = End time of the time period used for analysis
- Key 14 = First event used
- Key 15 = Last event used
- Key 16 = Number of good Bhabha events

- Key 17 = Number of background events
- Key 18 = Luminosity
- Key 19 = Error on luminosity
- Key 20 = Second luminosity estimate (if any)
- Key 21 = Error on second luminosity estimate (if any)

/NOMINAL_VERTEX

This directory contains the nominal coordinates of the e^+e^- interaction vertex computed by the reconstruction program. The keys used are:

- Key 5 = JOBID of the job producing the coordinates
- Key 8 = LEP fill number
- Key 9 = Run number
- Key 10 = PMCC of the job.

/LUMLIST

This directory contains lists of luminosity information called 'lumlists', for different runs. These lists contain information about the luminosity as monitored by the L3 luminosity monitoring system. The lumlists also contain information about the pass1 job and the tape number on which the reconstructed events were written out. The keys in this directory are:

- Key 5 = Lumlist program version number
- Key 8 = Run number
- Key 9 = Fill number
- Key 10 = Year
- Key 11 = period of data taking
- Key 12 = dummy
- Key 13 = dummy

Bibliography

[1] T. Sjöstrand et al., "Z Physics at LEP 1", CERN Report CERN-89-08, Vol. III (1989) p. 143.

[2] T. Hebbeker, "Tests of Quantum Chromodynamics in Hadronic Decays of Z^0 Boson Produced in e^+e^- Annihilation", Phys. Rep. 217 (1992) 69.

[3] M. Consoli and W. Hollik, "Z Physics at LEP 1", CERN Report CERN-89-08, Vol. I (1989) p. 7.

[4] F. A. Berends et al., "Z Physics at LEP 1", CERN Report CERN-89-08, Vol. I (1989) p. 89.

[5] G. Altarelli, G. Parisi, Nucl. Phys. B126 (1977) 298.

[6] R. D. Field, R. P. Feynman, Nucl. Phys. B 136 (1978) 1.

[7] B. Andersson et al., Phys. Rep. 97 (1983) 31; X. Artru, Phys. Rep. 97 (1983) 147.

[8] G. C. Fox, S. Wolfram, Nucl. Phys. B 213 (1983) 65.

[9] Y. Dokshitzer, V. A. Khoze, S. I. Troyan, A. H. Mueller, Rev. Mod. Phys. 60 (1988) 373.

[10] B. I. Ermolaev, V. S. Fadin, JETP Lett. 33 (1981) 269.

[11] A. H. Mueller, Phys. Lett. B104 (1981) 161.

[12] A. Bassetto, M. Ciafaloni, G. Marchesini, A. H. Mueller, Nucl. Phys. B207 (1982) 189.

[13] R. P. Feynman, Proc. 3rd Workshop on Current Problems in High Energy Particle Theory, Florence 1979, Eds. R. Casalbuoni et al., Johns Hopkins University Press, Baltimore 1979.

[14] G. Veneziano, Proc. 3rd Workshop on Current Problems in High Energy Particle Theory, Florence 1979, Eds. R. Casalbuoni et al., Johns Hopkins University Press, Baltimore 1979.

[15] A. Giovannini, Proc. Xth Int. Symp. on Multiparticle Dynamics, Goa 1979, Eds. S. N. Ganguli, P. K. Malhotra and A. Subramaniam (Tata Inst.) p. 364.

[16] G. Gustafson and A. Nilsson, Z. Phys. C52 (1991) 533.

[17] W. Ochs and J. Wosiek, Phys. Lett. B304 (1993) 144.

[18] Ph. Brax, J. L. Meunier, R. Peschanski, "Angular intermittency in QCD Jets", Nice preprint INLN 93.01 (1993) and Saclay preprint SPht/93-011.

[19] JACEE Collab., T. H. Burnett et al., Phys. Rev. Lett. 50 (1983) 2062.

[20] A. Bialas and R. Peschanski, Nucl. Phys. B273 (1986) 703.

[21] A. Bialas and R. Peschanski, Nucl. Phys. B308 (1988) 857.

[22] P. Lipa and B. Buschbeck, Phys. Lett. B223 (1989) 465.

[23] E. A. De Wolf, I. Dremin, W. Kittel, "Scaling Laws for Density Correlations and Fluctuations in Multiparticle Dynamics", University of Nijmegen preprint HEN-362.

[24] S. Myers, The LEP Collider from Design to Approval and Commissioning. Lecture delivered at CERN Acclerator School, CERN(91-80) 10 October 1991.

[25] L3 Collab., B. Adeva et al., "The construction of the L3 experiment", Nucl. Instr. & Meth. A289 (1990) 121.

[26] A. H. Walenta, IEEE Trans. Nucl. Sci. NS. 26, 1 (1979) 73.

[27] L3 Collab., O. Adriani et. al., Phys. Rep. 236 Nos. 1 & 2 (1993) 1.

[28] C. Timmermans "Measurement of muon pair production around the Z-resonance using L3 detector at LEP", Ph.D. Thesis, University of Nijmegen (1992).

[29] R. Brun, J. Zoll, "ZEBRA User Guide, CERN Program Library" (1987) unpublished.

[30] R. Brun et al., "Geant 3 User's Guide", CERN/DD/EE/84.1 (1984).

[31] R. P. Mount, "Database Systems For HEP Experiments", Comput. Phys. Commun. 45 (1987) 299.

[32] B. Adeva et. al. "The L3 Database System", Nuc. Instr.& Meth. A309 (1991) 318.

[33] R. Brun and P. Zanarini, "KUIP-Kit for a User Interface Package", CERN Computer Center Program Library, Long Write-up 1202 (1988) unpublished.

[34] H. J. Klein and J. Zoll, "PATCHY Reference Manual", CERN Program Library L400, 1988.

[35] R. Brun et al., "FFREAD User Guide and Reference Manual", CERN Computer Center Program Library, Long Write-up I103 (1986) unpublished.

[36] C. Boissat , E. Jagel , G. Lee , H. Renshall , "CSF User Guide", (1993) unpublished.

[37] L3 Collab., B. Adeva et. al., Z. Phys. C 55 (1992) 39.

[38] G. Altarelli, R. Kleiss and C. Verzegnassi, "Z Physics at LEP", CERN 89-08 Vol. I (1989) 434.

[39] L3 Collab., B. Adeva et al., Phys. Lett. B 265 (1991) 451.

[40] R. Rosmalen, Ph.D. Thesis , Univ. of Nijmegen, in preparation.

[41] Hans C. Eggers, "Intermittency, moments and correlations in distributions of particles created in high energy collisions", Ph.D Thesis, University of Arizona (1991).

[42] F. P. M. Botterweck, "Density Fluctuations in π^+/K^+P Interactions at 250 GeV/c", Ph.D Thesis, University of Nijmegen (1992).

[43] W. Ochs, Phys. Lett. B247 (1990) 101.

[44] A. Bialas and J. Seixas, Phys. Lett. B250 (1990) 161.

[45] P. Carruthers, Ap. J. 380 (1991) 24; P. Lipa, Proc. Ringberg Workshop on Multiparticle Production, R. C, Hwa et al. (eds), p. 96. Singapore: World Scientific 1992; P. Lipa et al., Phys. Lett. B285 (1992) 300.

[46] NA22 Collab., M. Adamus et al., Phys. Lett. B185 (1987) 200.

[47] P. Lipa, "Intermittency in Antiproton-proton Collisions", Ph.D. Thesis, University of Vienna Austria, HEPHY-PUB 542/90 (1990).

[48] F. James, "MINUIT: Function Minimization and Error Analysis", CERN Program Library D506, 1992.

[49] NA22 Collab. N. Agababyan et al., Z. Phys. C 59, (1993) 405.

[50] UA1 Collab, N. Neumeister et al., Z. Phys. C 60 (1993) 633.

[51] JADE Collab., W. Bartel et al., Z. Phys. C 33 (9186) 23; JADE Collab., S. Bethke et al., Phys. Lett. B213 (1988) 235.

[52] Opal Collab., P. D. Acton et. al., Z. Phys. C 58 (1993) 207.

[53] E.R. Boudinov, P. V. Chliapnikov and V. A. Uvarov, Phys. Lett B309 (1993) 210-221.

[54] Azimov, Ya. I., Yu. L. Dokshitzer, V. A. Khoze, S. I. Troyan, Z. Phys. C27 (1985) 65. and Azimov, Ya. I., Yu. L. Dokshitzer, V. A. Khoze, S. I. Troyan, "QCD portrait of hadronic jets", Leningrad Nuclear Physics Institute Preprint No. 1230.

[55] H. Yamamoto, 1985, in *International Symposium on Lepton and Photon Interactions at High Energies (12th)*, Kyoto, edited by Michiji Konuma and Kasuke Takahashi (Kyoto University Kyoto), p. 50.

[56] K. Sugano, 1986, "Gluon jets" Argonne National Laboratory Report ANL-86-133 unpublished.

[57] M. A. Chmeissani, private communication, 1993.

[58] T. Spickermann, private communication, 1993.

[59] C. L. Basham, L. S. Brown, S. D. Ellis, and S. T. Love, Phys. Rev. D17 (1977) 2298.

[60] JETSET 7.3 Monte Carlo program:
T. Sjöstrand, Comput. Phys. Commun. 39 (1986) 347;
T. Sjöstrand, M. Bengtsson, Comput. Phys. Commun. 43 (1987) 367.

[61] ARIADNE 4.04 Monte Carlo Program:
L. Lönnblad Comput. Phys. Commun. 71 (1992) 15.

[62] NLLJET 2.0 Monte Carlo Program:
K. Kato, T. Munehisa, Comput. Phys. Commun. 64 (1991) 67.

[63] HERWIG 5.6 Monte Carlo Program:
G. Marchesini, B. R. Webber, G. Abbiendi, I. G. Knowles, M. H. Seymour, and L. Stanco, Comput. Phys. Commun., 67 (1992) 465.

[64] COJETS 6.23 Monte Carlo Program:
R. Odorico, Comput. Phys. Commun., 72 (1992) 235.

[65] G. Gustafson, G. Ingelman, and T. Sjöstrand, Phys. Rep. 97 (1983) 31.

Summary

The subject of this thesis is particle correlations in hadronic decays of the Z boson produced in the e^+e^- collisions at LEP. A study of these correlations may lead to a better understanding of the so-called parton shower phase of hadron production.

The process of hadron production in e^+e^- collisions is believed to proceed through 4 successive phases. The initial $q\bar{q}$ system is produced in the first phase. This system then radiates gluons which in turn can radiate additional gluons or convert into a $q\bar{q}$ pair. This phase is called the parton shower. This is followed by the hadronisation phase, in which the quarks and gluons combine to form hadrons. Finally, the unstable hadrons decay. QCD is considered to be the theory of strong interactions and makes interesting predictions for the parton shower phase. One prediction is that, in the evolution of parton showers with running α_s, the angles between successive partons decrease because of interference between gluons. This effect has come to be known as *Angular Ordering.* A second prediction is that the process of parton showering is approximately self similar in nature, leading to fractals and fractal dimensions in hadron production. This latter prediction has come to light recently in the wake of studies of the so-called *Intermittency* effect.

L3 is one of the four detectors set up in the LEP ring to detect particles from e^+e^- collisions. A multiwire central tracking chamber working on the time expansion principle measures the direction and momentum of charged particles. The energy is measured with a calorimeter system by the total absorption technique. The calorimeter system comprises an electromagnetic calorimeter made of BGO crystals with a high stopping power for electrons and photons and a hadron calorimeter made of uranium plates sandwiched with brass proportional wire chambers. A scintillator system gives precise timing information for the events. The muons are detected by a drift chamber system positioned outside the calorimeters. All detecting elements are surrounded by a magnet providing a field of 0.5 Tesla. Event recording is triggered by a system constructed in three logical layers, making decisions with increasing sophistication. A computer controlled electronic system is used for data acquisition.

Owing to the complexity of present day electronic detectors and to the large amount of data collected by them, it has become necessary to have an automated system for book keeping of the data processing performed off line. A system has been developed which

is capable of uniquely identifying every computer job, the output files the job produces, and the parameter settings used for processing the data and Monte Carlo events. This system makes use of the DBL3 database package for storing the information on jobs into a database designed for this purpose. This system has been successfully used by the L3 collaboration since 1991.

The analysis presented in this thesis uses correlations between particles to study parton showers. The L3 detector measures the particle directions of both charged and neutral particles, but the resolution for charged particles is much better than for neutral ones. Since, for particle correlation studies, it is important to have a good two-particle resolution, only events with well reconstructed tracks are used. To select such events, a procedure is used which is based on tracks of charged particles in the TEC. Each track in an event is required to fulfill criteria defining a good track. The efficiency for two tracks to be detected as separated tracks is found to be 94 %. The detector resolution in variables used for the correlation studies is determined from Monte Carlo simulations of the detector effects.

The formalism used to study the phenomenon of intermittency is that of normalised factorial moments. The phase-space variable range of an event sample is divided into a large number of small intervals. The particle multiplicity is then studied in smaller and smaller intervals. A power-law behaviour of normalised factorial moments with decreasing bin size indicates the presence of intermittency. A new development in factorial moment analysis, called density strip integrals, has been proposed recently. It avoids splitting the events into bins, by using a strip volume of integration instead of the box volume of conventional factorial moment analysis.

Factorial moments in azimuthal angle ϕ around the beam direction are presented and compared to different Monte Carlo models. Good agreement is observed with the models used. Good agreement is also observed between data and the JETSET 7.3 Monte Carlo model, if the events are divided into high and low multiplicity samples.

The squared 4-momentum difference Q^2 between two tracks is a theoretically preferred variable in jet evolution studies. Density strip integrals in Q^2 are compared to JETSET 7.3 Monte Carlo model for the total event sample. We observe a signal for intermittency in e^+e^- collisions at LEP on the Z resonance. The signal is particularly well seen when using the four-momentum difference Q^2 as the phase-space variable. The effect is stronger than observed in hadronic collisions, but smaller than expected from QCD for the perturbative region (e.g. at $Q^2 \approx M_z$). Resonances and Bose-Einstein interference contribute at lower Q^2. For the first time, a multiplicity dependence is seen also in e^+e^- collisions. It is present for $-\ln Q^2 < 1$ (large values of Q^2), but not for larger values (small Q^2). The effect is stronger in two-jet than in three-jet events and stronger in transverse momenta above average. The Monte Carlo program JETSET 7.3 PS provides a good qualitative description of the data, but tends to overestimate the effect at small Q^2 and small p_t.

The effect of angular ordering in parton showers can be studied under the assumption of Local Parton Hadron Duality (LPHD). We study this effect by comparing angular particle correlations for particles from the same jet and those for particles coming from different jets. The correlation function used is similar to the energy-energy-correlation

(EEC) and is called the particle-particle-correlation (PPC). The asymmetry of this correlation function is called particle-particle-correlation-asymmetry (PPCA). We argue that, in the case of no angular ordering, one expects to observe a larger PPCA than in the case of angular ordering. Different Monte Carlo models are presented and their quality is assessed by means of event shape variable distributions. We find that the correlation asymmetry PPCA is insensitive to the change of the tuned JETSET 7.3 Monte Carlo parameters by 1 standard deviation. We also check the effect of Bose-Einstein correlation on PPCA using JETSET 7.3 and find it insignificant for this study. We observe that the data are well reproduced by the models containing angular ordering, but that the models without angular ordering fail to reproduce the data. We, therefore, conclude that parton showers indicate the presence of angular ordering in subsequent branchings.

Samenvatting

Deeltjescorrelaties in Hadronische Vervallen van het Z Boson

Het onderwerp van dit proefschrift wordt gevormd door deeltjescorrelaties in hadronische vervallen van het Z-boson, geproduceerd in e^+e^--botsingen bij LEP. De studie van deze correlaties leidt hopelijk tot een beter begrip van de zogenaamde parton-shower fase in de productie van hadronen.

Men veronderstelt dat deze productie van hadronen in e^+e^--botsingen geschiedt in vier opeenvolgende fasen. In de eerste fase wordt een $q\bar{q}$-systeem geproduceerd. Dit systeem straalt gluonen uit, die op hun beurt weer gluonen kunnen uitstralen of vervallen in een $q\bar{q}$-paar. Deze fase heet de parton-shower fase. Hij wordt gevolgd door een fase van hadronisatie, waarin de quarks en gluonen omgezet worden in hadronen. Tenslotte vervallen de onstabiele hadronen. QCD wordt gezien als *de* theorie van de sterke wisselwerking, en doet interessante voorspellingen over de parton-shower fase. Een van die voorspellingen is, dat in de evolutie van parton-showers met veranderende α_s, de hoeken tussen opeenvolgende partonen kleiner worden tengevolge van de interferentie tussen gluonen. Dit effect is bekend geworden onder de naam *hoek-ordening.* Een tweede voorspelling is dat het parton-shower proces bij benadering self-similar is, wat leidt tot fractals en fractale dimensies in de productie van hadronen. Deze laatste voorspelling is onlangs aan het licht gekomen, naar aanleiding van studies naar het zogenaamde *intermittency*-effect.

L3 is een van de vier detectoren die gebouwd zijn aan de LEP-ring om de deeltjes, die geproduceerd worden in e^+e^--botsingen, te bestuderen. Een centrale sporenkamer, de TEC, werkend volgens het principe van 'tijdsexpansie', meet de richting en impuls van geladen sporen. Energieën worden gemeten in een calorimetersysteem. Dit systeem bevat een electromagnetische calorimeter, bestaand uit BGO-kristallen met een hoog stoppend vermogen voor electronen en fotonen, en een hadronische calorimeter, bestaand uit lagen uranium-platen afgewisseld door koperen proportionele telbuizen. Een systeem van scintillatoren geeft preciese tijdinformatie over de interacties. Muonen worden gedetecteerd door een systeem van driftkamers buiten de calorimeters. Alle subdetectoren worden omringd door een magneet die een veld van 0.5 Tesla opwekt. De registratie van interacties wordt in werking gezet door een systeem opgezet in drie lagen, die beslissingen van oplopende sophisticatie nemen. Een computergestuurd electronisch systeem wordt gebruikt voor het verzamelen van de gegevens.

Gezien de complexiteit van hedendaagse detectoren en de grote hoeveelheid hiermee verzamelde data is de noodzaak gerezen van een geautomatiseerd systeem voor de boekhouding van de offline dataverwerking. Een systeem is ontwikkeld dat in staat is eenduidig iedere computertaak, de bestanden die deze taak oplevert, en de parameters gebruikt bij het verwerken van de data en Monte Carlo interacties te identificeren. Dit systeem maakt gebruik van het DBL3 database-pakket om informatie op te slaan in speciaal hiervoor ontworpen databases. Dit systeem is sinds 1991 in gebruik in het L3-experiment.

De analyse die in dit proefschrift beschreven wordt, gebruikt de correlaties tussen deeltjes om parton-showers te bestuderen. De L3-detector bepaalt de richtingen van zowel geladen als neutrale deeltjes, maar de resolutie voor geladen deeltjes is veel beter dan die voor neutrale deeltjes. Omdat in de studie van deeltjes-correlaties een goede twee-deeltjes resolutie belangrijk is, worden alleen interacties met goed gereconstrueerde sporen gebruikt. Om deze interacties te selecteren wordt een procedure gehanteerd die gebaseerd is op de sporen van geladen deeltjes in de TEC. Ieder spoor in een interactie moet voldoen aan criteria die goede sporen definiëren. De efficiëntie waarmee verschillende sporen als gescheiden worden gezien is 94%. De detectorresoluties in de variabelen die gebruikt worden voor de studie van correlaties, worden bepaald met behulp van Monte Carlo simulaties van de detectoreffecten.

Het formalisme gebruikt voor de studie van het intermittency-fenomeen is dat van genormaliseerde factoriële momenten. Het bereik van een data-sample in faseruimtevariabelen wordt onderverdeeld in een groot aantal kleine intervallen. De deeltjesmultipliciteit wordt dan bestudeerd voor steeds kleinere intervallen. Als de genormaliseerde factoriële momenten als een machtsfunctie afhangen van de grootte van de intervallen is dit een aanwijzing voor het optreden van intermittency. Onlangs is een nieuwe ontwikkeling voorgesteld in de analyse van factoriële momenten: de zogenaamde density-strip integralen. Deze vermijden het splitsen van de interacties in intervallen, door als integratievolume een strook te gebruiken inplaats van de rechthoek die gebruikt wordt in de conventionele analyse van factoriële momenten.

De factoriële momenten in de azimuth-hoek ϕ om de as van de bundel worden gepresenteerd en vergeleken met de verschillende Monte Carlo modellen. De overeenstemming met de gebruikte modellen is goed. Ook wordt een goede overeenstemming geconstateerd wanneer de interacties verdeeld worden in lage en hoge multipliciteiten.

Theoretisch gezien verdient het aanbeveling om in de studie van parton-showers het kwadratische vierimpulsverschil tussen twee sporen, Q^2, als variabele te gebruiken. De density-strip integralen in Q^2 worden vergeleken met het JETSET 7.3 Monte Carlo model voor alle data. We nemen een signaal waar voor intermittency in e^+e^--botsingen bij LEP op de Z-resonantie. Dit signaal is bijzonder duidelijk wanneer het vierimpulsverschil Q^2 als faseruimtevariabele gebruikt wordt. Het effect is groter dan het effect waargenomen in hadronbotsingen, maar kleiner dan verwacht op grond van QCD voor het storingstheoretische gebied ($Q^2 \approx M_Z^2$). Bij lagere Q^2 dragen resonanties en Bose-Einstein interferentie bij. Voor het eerst wordt ook in e^+e^--botsingen een afhankelijkheid van de multipliciteit waargenomen. Deze afhankelijkheid is aanwezig voor $Q^2 > 1\text{GeV}^2$, maar niet voor lagere waarden. Het effect is sterker in 2-jet interacties dan in 3-jet interacties, en sterker voor meer dan gemiddelde transversale impulsen. Het JETSET 7.3 Monte Carlo programma geeft een goede kwalitatieve beschrijving van de data, maar neigt ertoe het effect bij kleinere p_t te overschatten.

Het effect van hoekordening in parton-showers kan bestudeerd worden onder de aanname van Locale Parton-Hadron Dualiteit (LPHD). We bestuderen dit effect door hoekcorrelaties voor deeltjes in dezelfde jet te vergelijken met die van deeltjes die van verschillende jets afkomstig zijn. De gebruikte correlatiefunctie lijkt op de energie-energiecorrelatie (EEC) en wordt deeltjes-deeltjes-correlatie (PPC) genoemd. De asymmetrie van deze correlatiefunctie heet deeltjes-deeltjes-correlatie-asymmetrie (PPCA). We stellen dat, bij afwezigheid van hoekordening, men een grotere PPCA verwacht te zien dan in het geval van hoekordening. Verscheidene Monte-Carlo modellen worden gepresenteerd en hun kwaliteit wordt beoordeeld op grond van globale karakteristieken van de data. We vinden dat de correlatieasymmetrie PPCA ongevoelig is voor veranderingen met een standaarddeviatie in de ingestelde JETSET 7.3 Monte Carlo parameters. We bekijken ook het effect van Bose-Einstein correlaties op de PPCA met behulp van het JETSET 7.3 programma en concluderen dat deze van geen belang zijn in deze studie. We stellen vast dat de data goed beschreven worden door de modellen die hoekordening bevatten, maar dat de modellen zonder hoekordening niet in staat zijn de data te beschrijven. Daarom concluderen we dat parton-showers inderdaad aan hoekordening onderhevig zijn in opeenvolgende stappen.

Curriculum vitae

The author of this thesis was born on 29th June 1961 in Lahore Pakistan. he passed his matriculation from the Crescent Model School Lahore. He attended the F. C. College Lahore for his F.Sc. certicifate. For his B.Sc. degree, he attended the Govt. College Lahore. He studied physics at the Punjab University Lahore and performed research on the topic of 'Phase Transitions in Metallic Glasses' under the supervision of Prof. M. S. Zafar and Dr. A. Shamim. He graduated from the Punjab University Lahore with an M.Sc. degree in Physics in 1986. He joined a post-graduate training programme at CTC Islamabad for a one year computer hardware and software course in 1987. He went to CERN in Geneva to join the L3 experiment in 1988 as an FBLJA fellow of the World Lab. and worked on database software and QCD analysis. He joined a Ph.D programme with the Katholieke Universiteit Nijmegen in June 1990 under the supervision of Prof. E. W. Kittel. He gave invited talks at 4th International Symposium on Heavy Flavour Physics, ORSAY-France in 1991 and at Societa Italiana di Fisica LXXVII Congresso Nazionale in 1991. From may 1992 to may 1994 the author was an Assistent in Opleiding at the K. U. Nijmegen.